FLOW DISTRIBUTION CONTROL AND THERMAL HOMOGENIZATION WITH EHD CONDUCTION PUMPING AND EXPERIMENTAL STUDIES IN POOL BOILING AND INTERNAL CONDENSATION

by

Lei Yang

A Dissertation

Submitted to the Faculty

of the

WORCESTER POLYTECHNIC INSTITUTE

in partial fulfillment of the requirements for the

Degree of Doctor of Philosophy

in

Mechanical Engineering

August 2017

APPROVED:

_____

Dr. Jamal Yagoobi, Major Advisor

_____

Dr. Brian Savilonis, Committee Member

_____

Dr. John Blandino, Committee Member

_____

Dr. Yan Wang, Committee Member

_____

Dr. Pratap M. Rao, Graduate Committee Representative

ACKNOWLEDGMENT

This dissertation would not become a reality without the generous support and help of many individuals. I would like to extend my sincere thanks to all of them.

Foremost, I would like to express my special gratitude to my advisor, Dr. Jamal Yagoobi, who gave me this wonderful opportunity for advanced learning and research. I will always appreciate the invaluable advice he gave me on my career and life.

I am grateful to NASA Headquarters – Microgravity Fluid Physics Program, National Science Foundation and United Technology Research Center for their financial support of this research project.

I would also like to thank the members of my dissertation committee, Dr. John Blandino, Dr. Brian Savilonis, Dr. Yan Wang and Dr. Pratap Rao for their feedback and advice on my research.

I am thankful to Dr. Viral Patel, from whom I learned many useful experimental skills, it was a pleasure working with him. My thanks also go to my colleagues: Michal Talmor, who helped me on the numerical analysis in chapter 3; Jon J. Barruetabeña, Connor D. McGuirk, and Lily M. Ouellette who built the experimental setup for the study of chapter 3; and Payam Razavi, who helped me take high-speed videos and photos for pool boiling study.

I am forever grateful to my parents and friends for their encouragement which helped me in completion of this dissertation. I would not be at this stage in my life without their constant support.

Table of Contents

LIST OF TABLE

LIST OF FIGURE

LIST OF SYMBOLS

A	Heat transfer surface area of evaporator, based on tube inner diameter, m^2
A^+	Positive ion
A_c	Cross-sectional area of evaporator, m^2
AB	Neutral species
b	Ion mobility, $m^2/V{\cdot}s$
B^-	Negative ion
c	Concentration of neutral species, mol/m^3
c_p	Specific heat, $J/kg{\cdot}K$
D	Diffusion coefficient
e	Electron charge, C
E	Electric field intensity, V/m
$\boldsymbol{E}$	Electric field vector, V/m
$\boldsymbol{f}_{EHD}$	Electric body force density vector, N/m^3
$\boldsymbol{f}_g$	Gravitational force density vector, N/m^3
$F(\omega_e)$	Onsager function
g	Gravitational acceleration, m/s^2
$\boldsymbol{g}$	Gravitational acceleration vector, m/s^2
G	Mass flux through evaporator = $\frac{\dot{m}}{A_c}$, $kg/m^2{\cdot}s$
h	Heat transfer coefficient, $W/m^2{\cdot}K$
h_i	Local heat transfer coefficient at thermocouple station i, $W/m^2{\cdot}K$
h_{lv}	Latent heat of vaporization, kJ/kg
h_{lo}	Single-phase, laminar, all-liquid flow heat transfer coefficient, $W/m^2{\cdot}K$

I_1	Modified Bessel function of the first kind
J	Current density, A/m^2
k	Thermal conductivity, W/m·K
k_B	Boltzmann constant, J/K
k_d	Field enhanced dissociation rate
k_D	Dissociation rate constant
k_R	Recombination rate constant
L	Overall length of evaporator, m
$\dot{m}$	Mass flow, kg/s
M	Molecular weight
M_0	Mobility ratio
Nu	Nusselt number = $Nu_i = \frac{h_i D}{k_l}$
n	Negative charge density, C/m^3
p	Positive charge density, C/m^3
P	Pressure, Pa
P_C	Critical pressure, Pa
Pr	Prandtl number
q	Heat transfer rate, W
q''	Heat flux, W/m^2
q''_{max}	Critical heat flux, W/m^2
Q	Heater power, W
q''_{MB}	Heat flux for Moissis-Berenson transition, W/m^2
R	Resistance, Ω

Ra	Rayleigh number
Re	Reynolds number
Rp	Surface roughness
S	Surface area of the heater, m^2
t	Time, s
t_e	Charge relaxation time, s
T	Temperature, K
T_{sat}	Saturation temperature, K
T_w	Wall temperature, K
ΔT	Wall superheat, K
$\boldsymbol{u}$	Fluid velocity vector, m/s
U	Applied voltage, V
	Total heat transfer coefficient, $W/m^2 \cdot K$
$\boldsymbol{v}$	Velocity vector, m/s
x	Vapor quality
x_i	Vapor quality at thermocouple station i
X_{tt}	Martinelli parameter

Greek Symbols

δ_{ij}	Kronecker delta
ε	Electric permittivity, F/m
ζ	Zeta potential
θ	Surface inclination angle, °

	Liquid contact angel, °
λ	Simplified heterocharge layer thickness, m
λ_D	Taylor wave node spacing
μ	Dynamic viscosity, N·s/m^2
ρ	Density, kg/m^3
ρ_e	Net charge density, C/m^3
τ_{ij}	Maxwell stress tensor
τ_{res}	Response time, s
σ	Surface tension, N/m
σ_e	Electric conductivity, S/m
ϕ	Electric potential, V
Φ	Molecular flux of neutral species
Ψ	Potential distribution
ω_e	Parameter defined by equation 7

Subscripts

i, j, k	Variables
l	Liquid
T	Constant temperature
v	Vapor
+	Positive charges
-	Negative charges

ABSTRACT

Electrohydrodynamic (EHD) pumping relies on the interaction between electrical and flow fields in a dielectric fluid medium. Advantages such as simple and robust design as well as negligible vibration and noise during operation make EHD conduction pumping suitable for various applications. This work investigates meso-scale EHD conduction pumping used as an active flow distribution control mechanism for thermal management systems. Two different scenarios are considered for this purpose: alteration of uniform flow distribution and flow maldistribution correction. Its capability of actively controlling the flow distribution is examined in terms of the value of applied potential for initiation of flow divergence or flow equalization and the flow rate difference between each branch. Experimental results confirm that the reverse pumping direction configuration of EHD pumping is more effective than the same pumping direction configuration. A fundamental explanation of the heterocharge layer development is provided for the effect of flow direction on EHD conduction pumping performance. This study also involves a macro-scale EHD conduction pump used as an alternative mechanism of mixing liquid within a storage tank, for example under low-g condition. A numerical analysis of a simplified model of the experimental setup is provided to illustrate the liquid mixing and thermal homogenization process. The experimental and numerical study provide fundamental understanding of liquid mixing and thermal homogenization via EHD conduction pumping.

Liquid-vapor phase change phenomena are used as effective mechanisms for heat transfer enhancement and have many applications such as HVAC&R systems. With this in mind, two detailed studies in pool boiling and in-tube flow condensation are carried out. Specifically, nucleate pool boiling on nano-textured surfaces, made of alumina ceramic substrate covered by electrospun nanofiber, is experimentally investigated. Also, the role of surface roughness and

orientation in pool boiling is experimentally characterized. The in-tube convective condensation of pure water in mini-channels under sub-atmospheric pressure is also experimentally explored. This study provides valuable information for the design of condensers in a vapor compression cycle of HVAC&R systems using water as the refrigerant, this process has zero global warming potential.

CHAPTER 1 INTRODUCTION

1.1 Electrohydrodynamic pumping

Electrohydrodynamics (EHD) is a field of research studying the interactions between externally applied electrical fields and fluid flow fields. Although the notion that electrical charge can affect fluids has been known for centuries [1], research into utilizing EHD phenomenon to generate fluid flow did not begin in earnest until the 1960's [2-5]. EHD devices have no moving parts and are able to pump traditionally difficult flows such as single and two-phase thin film flows [6,7], These devices can therefore be more easily miniaturized than mechanical pumping devices, and recent research has shown that some EHD pumping can operate in microgravity conditions [8].These unique properties of EHD devices make them advantageous for usage in a wide range of applications, including small-scale electronics cooling, flow distribution control for single or two-phase flows, propellant utilization enhancement, and aerospace thermal control [9].

The model for EHD driven flows couples the Navier-Stokes equations for fluid flow with Maxwell's equations for electrostatics via an additional force density term in the momentum conservation equation. This term describes the sum of EHD body force densities that are applied on a linear dielectric working fluid [10], and is generally written as:

$$\boldsymbol{f}_{EHD} = \rho_e \boldsymbol{E} - \frac{1}{2} E^2 \nabla \varepsilon + \frac{1}{2} \nabla \left[E^2 \rho \left(\frac{\partial \varepsilon}{\partial \rho} \right)_T \right] \tag{1}$$

The first term in the above equation is the Coulomb force density, also known as the electrophoretic force density, which describes the interaction between the applied electrical field, $\bar{E}$, and the free space charge density, ρ_e. The second term is the dielectrophoretic force density, which arises from polarization effects in a working fluid with gradients or discontinuities in its electrical permittivity, ε. The final term is the electrostriction force density, which is due to

changes in the electrical permittivity of the working fluid as a result of changes in fluid density, and is primarily relevant for compressible flows. In the case of a bulk fluid where the force being applied is most significant at a boundary location, it is possible to use the Maxwell stress tensor to describe the EHD body force density applied on the surface of a volume enclosing the system of interest [11]. This can be done in lieu of determining the charge distribution in the bulk if the electric field arising from these charges is known,

$$\tau_{ij} = \varepsilon E_i E_j - \frac{\varepsilon}{2}\delta_{ij}E_k E_k \left[1 - \frac{\rho}{\varepsilon}\left(\frac{\partial \varepsilon}{\partial \rho}\right)_T\right] \tag{2}$$

Since even in multi-phase flows each phase is often considered incompressible for the purpose of modeling, the electrostriction force term can be neglected in the formulation of most EHD driven flows. The dielectrophoretic force is relevant in non-isothermal applications, or when there exists an interface between regions of the fluid domain with significantly different electrical permittivity values, such as a vapor-liquid interface. This force acts along the electric permittivity gradient, unlike the electrophoretic force that acts in the direction of the electric field. This means that the dielectrophoretic force can create undesired flow motion that opposes or reduces the desired effect of the electrophoretic force, as well as introduces flow instabilities [9]. If a single phase working fluid is assumed to be incompressible and isothermal, the force density will be dominated by the electrophoretic force. Most existing applications of EHD driven internal flows, such as EHD pumps, follow this description due to its simplicity. There exist three recognized types of EHD pumping techniques, which differ by how each introduces free charges into the working fluid: ion drag pumping, induction pumping, and conduction pumping [12].

1.1.1 Ion Drag Pumping

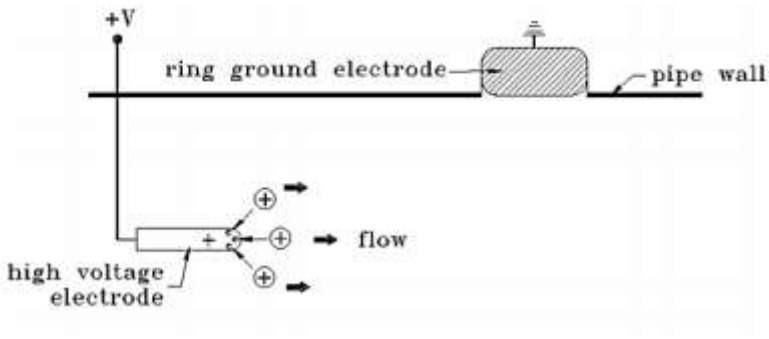

Figure 1: EHD ion Drag Pumping Schematic [13]

Ion drag pumping, also known as injection pumping, is the most maturely developed one of the EHD pumping mechanisms. An ion drag EHD pump, shown in Figure 1, introduces free charges into a working fluid via applying a sufficiently strong direct current (DC) electric field between a sharp emitter electrode and a collector electrode, such that a corona discharge of material from the sharp emitter tip occurs, in the forms of ions of the same polarity as the emitter. The emitted charges travel to the oppositely charged collector electrode, imparting their momentum to the surrounding fluid and generating a strong net flow [14].

The phenomenon of injected ions discharged from sharp points are able to exert mechanical forces on fluids has been known for more than a century [15]. However, the first model describing the phenomenon in all fluid media was not developed until much later [2] and verified experimentally [3,4] using transformer oil. This model showed that significant pressure head could be generated using injected charges into a dielectric liquid, making ion drag pumping a viable theoretical replacement to select mechanical pumps. Figure 1 shows a common configuration in a circular flow channel, with the emitter electrode receiving high voltage while the ring shaped collector electrode mounted into the wall being grounded. It is, however, possible to configure this type of pump with the emitter being grounded and the collector the receiving high voltage [9].

The primary advantages of the ion drag EHD pumping technique are the simplicity of the design, high pressure and flow rate generation compared to other techniques, and ability to pump single phase gas flows. The main disadvantage of ion drag pumping is the erosion of the emitter electrode over time, and degradation of the fluid's dielectric properties due to the injection of charges [16]. The erosion effect is of major concern for small scale applications, since it significantly limits the operational lifetime of the ion drag pump. Ion drag also requires higher power consumption than other techniques, due to the strong electric field that must overcome the fluid's breakdown voltage to generate the corona discharge and the strong ionic currents [9].

1.1.2 Induction Pumping

In this EHD pumping technique, charges are induced in the working fluid as a result of the applied electric field. A positive potential induces negative charges on the liquid side near the electrodes, and vice versa. These charges drift through the liquid medium through normal conduction processes, but are delayed at a discontinuity or gradient in electric conductivity, leading to a local accumulation of charge. Most commonly, such discontinuities can be found at interfaces between the liquid and vapor phase of a fluid [17], or between two immiscible fluids [10]. Unlike ion drag pumping, fluid motion cannot occur under the effect of a direct current electric field. To generate fluid motion, an alternating current (AC) travelling wave electric field must be used. To understand the mechanism of induction pumping, it is important to consider the charge relaxation time, t_e, of the fluid,

$$t_e = \frac{\varepsilon}{\sigma_e} \tag{3}$$

The charge relaxation time describes how long the induced charges will take to relax through the fluid to the locations of conductivity discontinuity [18]. Charges accumulating at these locations will then be attracted or repelled by the travelling potential wave. Because this relaxation

is not instantaneous, the induced charges will accumulate at the discontinuity interface at a certain time lag from when they were initially induced by the applied potential, leading to a phase shift between the original potential travelling wave and the surface charge carried by the traveling wave [9].

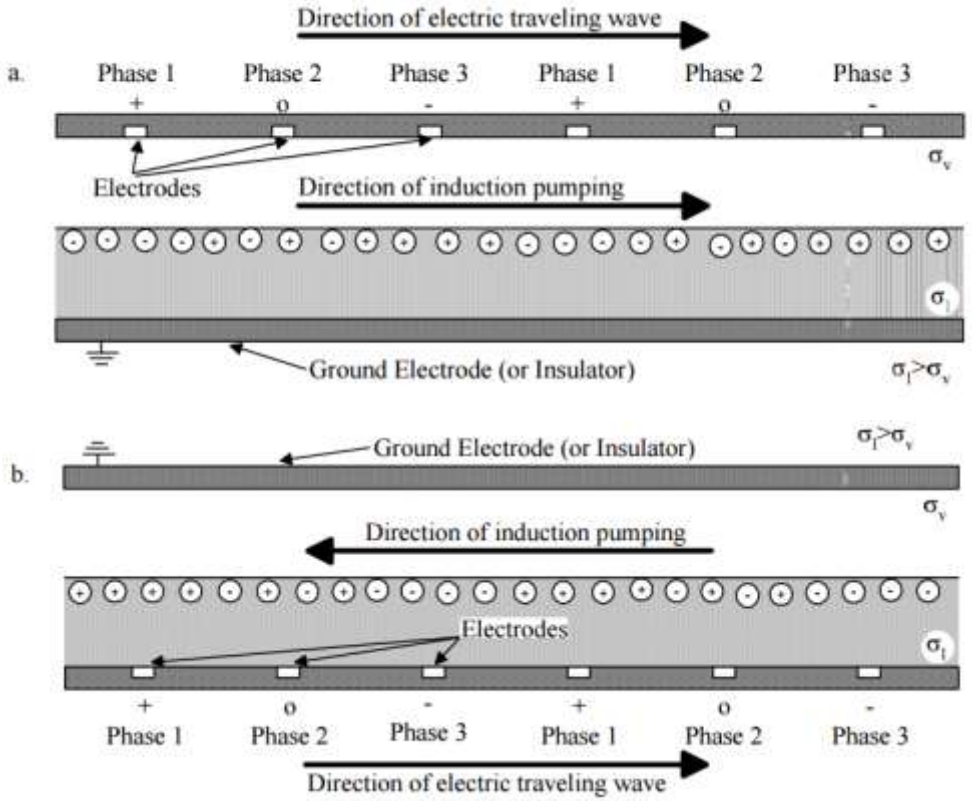

Figure 2: EHD induction pumping schematic, with travelling wave applied on

(a) the low conductivity side, (b) the high conductivity side [13]

The direction in which the fluid will move due to this attraction or repulsion is dependent on the direction of the conductivity gradient, as shown in Figure 2. In this figure, a 3-phase travelling wave field is shown applied through a series of identical electrodes embedded in the top or bottom wall of a rectangular channel filled with a layer of the vapor phase over a layer of the liquid phase of some fluid. Since these charges are induced in fluids with different conductivities,

and therefore different charge relaxation times, they will relax toward the interface at different rates, affecting the final charge composition on the interface.

Figure 2 (a) illustrates the case where the positive potential travelling wave is applied adjacent to the low conductivity fluid, where the charge relaxation time is longer. The induced positive charges on the fluid side will therefore take longer to reach the interface than the induced negative charges on the high conductivity fluid side. The charge composition at the interface across from the positive potential will therefore be negative. As the potential wave progresses, the negative interface charges will be pulled along in the same direction, and the induction pump would be operating in the attraction mode [9].

Conversely, Figure 2 (b) illustrates the case where the positive potential travelling wave is applied adjacent to the high conductivity fluid, where the charge relaxation time is shorter. In this case the composition of charges at the interface across from the positive potential will be more positive, as the positive induced charges will reach the interface more quickly than their negative counterparts. In this case, the interface charges will be repulsed by the travelling potential wave. This can result either in pumping in the opposite direction from the travelling wave, or increased pumping velocity in the direction of the travelling wave, depending on the time lag between the wave and the charge accumulation at the interface. In either case the induction pump would be operating in the repulsion mode [9].

The main advantages of induction pumping are its ability to pump different types of fluids, so long as the frequency of the AC traveling wave can be adjusted to match the inverse of the charge relaxation time of the fluid. The ability to pump two-phase flows and layers of immiscible fluids, and the ability to change the pumping direction by adjusting the frequency of the travelling wave, are also unique advantages to this pumping technique. The main disadvantage for this

technique is the complex power configurations needed to maintain the electric field wave, using a low frequency AC power source, as well as the temperature gradients. The overall complexity of the system, both in terms of instrumentation of the actual pumping devices and the mathematical modeling, is relatively high as well and prone to many modes of instability that must be designed around [9].

1.1.3 Conduction Pumping

The "conduction" term in the conduction pumping mechanism indicates that the free charges within a dielectric working fluid are generated by the dissociation of naturally occurring electrolytic impurities within a dielectric working fluid in lieu of injection or induction. In the absence of a strong electric field, under equilibrium conditions, these impurities dissociate into ions and recombine into neutral species at equal reaction rates, as described by,

$$AB \underset{Recombination}{\overset{Dissociation}{\rightleftharpoons}} A^+ + B^- \tag{4}$$

In general, the dissociation rate increases exponentially with electric field intensity, but the recombination rate is independent of the electric field intensity. When the electric field exceeds a certain threshold value (on the order of 10^5 V/m, depending on the working fluid), an abundance of free ionic charges are generated in the near-electrode region. This effect is known as the Onsager field enhanced dissociation [19]. The dissociated positive and negative ions are attracted toward oppositely charged electrodes. Due to a balance between how long the ions can maintain their charge, as described by the charge relaxation time, and the time the ions take to move through the characteristic length of the electrode gap in a viscous medium, as described by the ionic transit time, a new equilibrium forms [20]. Within a thin layer above each electrode. These layers are known as the heterocharge layers [21]. They have opposite polarity to the corresponding electrode and can be further divided into two sub-regions: compact layer and diffusion layer. The thickness

of the heterocharge layer is proportional to the corresponding relaxation time of the working fluid and the strength of the local electric field.

Numerical simulations of EHD conduction allow for better understanding of the profiles of the heterocharge layers [22].An example of numerical simulations of the heterocharge layer structure for flush electrodes is presented in Figure 3. The heterocharge layer profiles are shown for variations in a non-dimensional quantity, $M_0 = \sqrt{\frac{\varepsilon}{\rho b^2}}$, representing the working fluid properties.

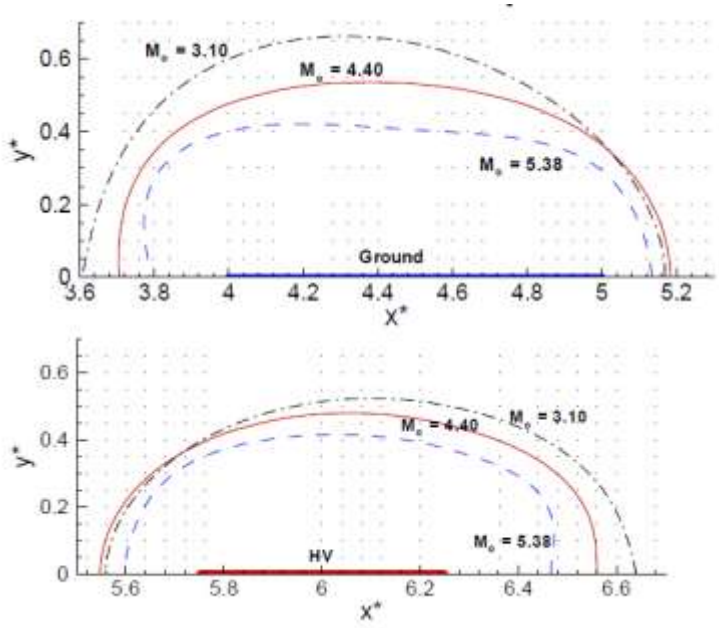

Figure 3: Flush electrodes heterocharge layer structure for different fluid properties [22]

For an electric field below a certain value (on the order of 10^7 V/m depending on the liquid characteristics and the electrode material), the ion injection at the electrode/liquid interface is considered to be negligible and conduction pumping mechanism is expected to be dominant. At a high electric field regime beyond this threshold value, the current suddenly increases steeply with an increase in the voltage due to the injection of ions from the electrodes into the liquid and the ion-drag pumping mechanism is expected to be dominant.

Although this pumping technique also requires strong electric fields in order to activate the field enhanced dissociation, corona discharge and fluid breakdown work against conduction pumping and must be avoided [23]. Therefore, all electrode surfaces are made smooth to ensure that there are no electric field concentrations at sharp features that can undergo corona discharge.

Under the assumption of equal ionic mobilities for both the negative and positive ions, if the high voltage and ground electrodes have the same wetted areas, such that the positive and negative heterocharge layers have the same dimensions and will generate equal forces, only flow circulation will occur between the electrodes. To generate a net flow, EHD conduction pumps use asymmetrical electrode configurations, where the electrode with the larger wetted surface area, and therefore larger heterocharge layer, determines the flow direction [22, 24]. In most cases, this corresponds to designing the high voltage electrode as having the larger wetted surface area than the ground electrode, to select for the negatively charged heterocharge layer to be more dominant, but the reverse configuration can be used as well. A schematic of a conduction pump with such asymmetrical electrodes is shown in Figure 4. In this figure, the larger high voltage electrode has a larger negative heterocharge layer than the positive heterocharge layer on the ground electrode, leading to a larger force component and a net flow to the right, as shown.

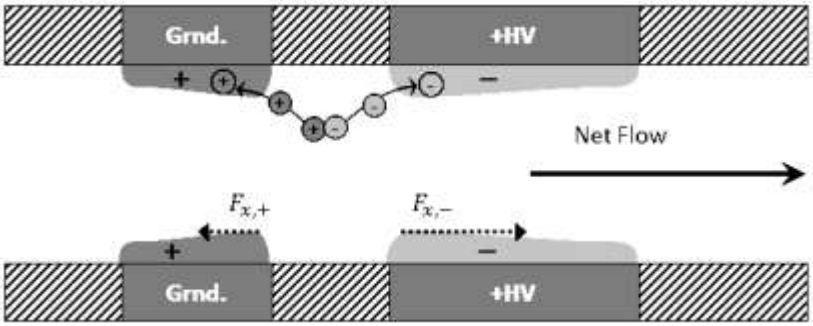

Figure 4: EHD conduction pumping schematic [25]

Unlike ion drag pumping and induction pumping, various electrode designs can be used with conduction pumping. Figure 5 shows some of the existing designs - hollow tube high voltage

and flush ring ground electrode, perforated or porous-permeable high voltage electrode, and multi-tube high voltage electrode. These different electrode designs will have different heterocharge layer profiles and therefore different force distributions in the liquid, which in turn will lead to different pressure generation versus flow rate performance for each electrode design [26].

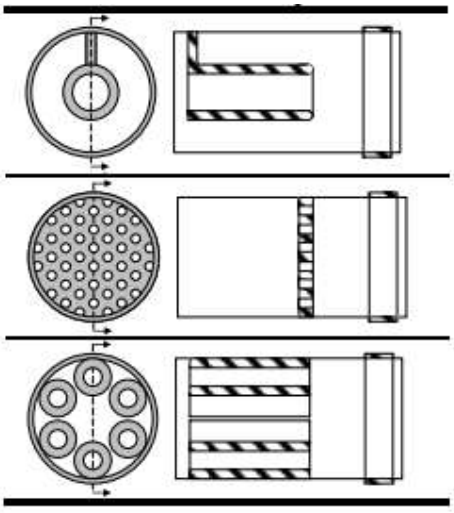

Figure 5: EHD conduction pump electrode design examples [26]

Unlike ion drag and induction pumping, the motion is not solely dominated by a single polarity of charge carriers. The model for conduction pumping must therefore account for both negative and positive ionic species,

$$\rho_e = p - n \tag{5}$$

Here, n_e and p_e are the negative and positive charge densities, respectively. These charge densities relate to the initial concentration of neutral species, c, through the constitutive relation for the balance between dissociation and recombination:

$$k_D c = k_R \left(\frac{pn}{e^2}\right) = k_R \frac{n_{eq}^2}{e^2} \tag{6}$$

where k_D and k_R are the dissociation and recombination rate constants, respectively, and e is the unit charge. Note that these rate constants have different units, s^{-1} for the dissociation and $m^3 s^{-1}$ for the recombination in SI units. In the above, n_{eq} is the equilibrium charge density of either

positive or negative species, since n_e and p_e are assumed to be the same in that situation. To account for the field enhancement effect, the Onsager function, $F(\omega_e)$, is used:

$$k_d = k_D F(\omega_e) = k_D \frac{I_1(4\omega_e)}{2\omega_e} \quad , \quad \omega_e = \left[\frac{e^3 E}{16\pi\varepsilon(k_B T)^2}\right] \tag{7}$$

The Onsager function utilizes the modified Bessel function of the first kind and order one, and the enhanced dissociation rate coefficient, ω_e. In the above equation, k_B is the Boltzmann constant, and k_{D0} is the original dissociation constant, which is identical to the recombination constant. As is shown, the Onsager function serves as a multiplication factor for the original dissociation constant. In the absence of an electric field the value of $F(\omega)$ is 1, and under the effect of the electric field it is greater than 1.

As the name of the technique implies, the primary charge transport mechanism is conduction. However, unlike the ordinary Ohmic conduction described for ion drag and induction pumping, the conductivity is now variable, depending on the charge density:

$$\sigma_e = (b_- n + b_+ p) \tag{8}$$

In the conductivity equation, b_- and b_+ represent the ionic mobilities of the negative and positive ions, respectively. The equation for current density must now be split to account for all the charged species of interest – positive and negative ions. In addition, a flux density equation for the neutral species must be provided:

$$J_\pm = b_\pm \rho_\pm \boldsymbol{E} + \rho_\pm \boldsymbol{v} - D_\pm \nabla \rho_\pm \tag{9}$$

$$\Phi = c\boldsymbol{v} - D\nabla c \tag{10}$$

In these equations, $\rho_\pm$, $b_\pm$ and D stand for the charge density, ionic mobility and diffusion coefficient belonging to each charged species, and D is the diffusion coefficient for the neutral species, respectively. Note that diffusion effects are not entirely negligible for EHD conduction,

since the heterocharge layers' shapes can be affected by diffusion of charges into the bulk of the working fluid, as well as diffusion of neutral species from the bulk into the near electrode region.

Since the charge density is now affected by chemical reaction rates, the charge conservation equations must also be split, and made to account for these reactions. In addition, a similar equation for the conservation of concentration of neutral species must also be supplied:

$$\nabla \cdot J_{\pm} = k_D ce - k_R \frac{pn}{e} \tag{11}$$

$$\nabla \cdot \Phi = k_R \left(\frac{pn}{e^2}\right) - k_D c \tag{12}$$

Otherwise the model is similar to ion drag pumping, with the Poisson equation and conservation of momentum equations largely unchanged:

$$\nabla^2 \Phi + \frac{p - n}{\varepsilon} = 0 \tag{13}$$

$$(\boldsymbol{v} \cdot \nabla)\boldsymbol{v} = \boldsymbol{f}_g - \nabla P + \frac{\mu}{\rho}\nabla^2 \boldsymbol{v} + \frac{1}{\rho}[(p - n)\boldsymbol{E}] \tag{14}$$

The boundary condition for flow is no-slip condition. For high voltage electrode and ground electrode, the potential boundary conditions are the applied voltage value and zero, respectively. The charge and concentration density boundary conditions only need to account for incoming and outgoing fluxes at the electrode surfaces and the inlet and outlet of the domain. As a general rule, it is assumed that no diffusion occurs between the electrode surfaces and the fluid, and that the charge density of each ionic species is zero on the electrode with the same polarity as the species. In the same fashion as ion drag pumping, solving these coupled equations numerically will account for the full flow inertia effects, including pressure losses and flow velocity effects on the shape of the heterocharge layers. However, a quick estimation of conduction pumping pressure generation is also available here.

The simplest model for EHD conduction is the 1D case of parallel plate electrodes [21]. Neglecting any flow, the charge conservation equations can be solved analytically. This yields a

simplified heterocharge layer thickness that depends on the ionic mobility, the charge relaxation time and the nominal magnitude of the electric field [21]:

$$\lambda_{\pm} = b_{\pm}\boldsymbol{E}t_e \tag{15}$$

Under the assumption of equal ionic mobilities, the thickness is expected to be the same over each of the electrodes, such that the magnitude of the net force will depend only on the dimensions of the electrodes. An integration of the electrophoretic force for this 1D model can therefore be performed over this thickness in order to estimate the resulting pressure [21]:

$$\Delta P = \int_0^{\lambda} (p - n)\boldsymbol{E}dx \tag{16}$$

Estimating this integral using Poisson's equation yields the following approximation [21]:

$$\Delta P = \int_0^{\lambda} \varepsilon E \frac{\partial \bar{E}}{\partial x} dx \approx \lambda\varepsilon(E)^2 \approx b\sigma_e E^3 \tag{17}$$

This relation tends to overestimate the actual magnitude of pressure generation for EHD conduction. Attempts to convert this general relation to account for the lower observed experimental values have been made using altered fluid properties [27] or accounting for the exact wetted surface areas participating in the formation of the heterocharge layer [28] with some measure of success.

In addition, the current consumed in conduction pumping is very small due to the short time the ions maintain their charge before recombination occurs outside the near-electrode region, leading to overall low power consumption for these types of EHD pumps. The main advantages of EHD conduction pumping are its reliability in long term operations, its low power consumption, and its simple, flexible electrode designs. The main disadvantages of this technique are lower pressure generation capabilities, difficulty pumping two phase flows, and manufacturing concerns due to the need for smooth electrodes in order to avoid charge injection from sharp features.

1.1.4 Size Scaling – Micro and Nano Scale EHD Theory

It should be noted that all EHD forces are volumetric forces, which act independently of gravity. In terms of size scaling, as an EHD device is scaled down any adverse effects from gravity would be minimized, and the EHD forces would dominate. However, other effects related to miniaturization will need to be taken into consideration as well, such as higher pressure losses, flow instabilities, and any effects on the charge distribution [29].

In dielectric fluids at very small scales, on the order of tens of microns or smaller, effects that are negligible in larger scales become prominent. The most important of these effects is the electric double layer (EDL). This is a unique formation of charge structure in the vicinity of any dielectric surface in contact with a fluid, due to natural physical or chemical processes such as absorption and adsorption. Once a surface gains a net charge, oppositely charged ionic species from the fluid adhere to the surface under strong electrostatic forces and form what is known as the Stern layer – an immobile layer of ions. Immediately beyond this immobile layer, a diffuse layer of mobile mixed ionic charges is present. The diffuse layer has the same charge sign as the Stern layer, but the electric potential drops off exponentially further into the fluid bulk, such that the bulk is still electroneutral. The characteristic drop off length is the Debye length of the EDL, which is usually on the order of nanometers. Within the diffuse layer there exists a slipping plane, which defines where the diffuse layer is able to shear off from the Stern layer. The potential at this slipping plane, ζ, is known as the zeta potential [30]. Figure 6 shows a schematic of the EDL and the potential distribution, Ψ, along its length, y'. In this figure, Ψ_0 represents the applied potential on the electrode surface at $y' = 0$.

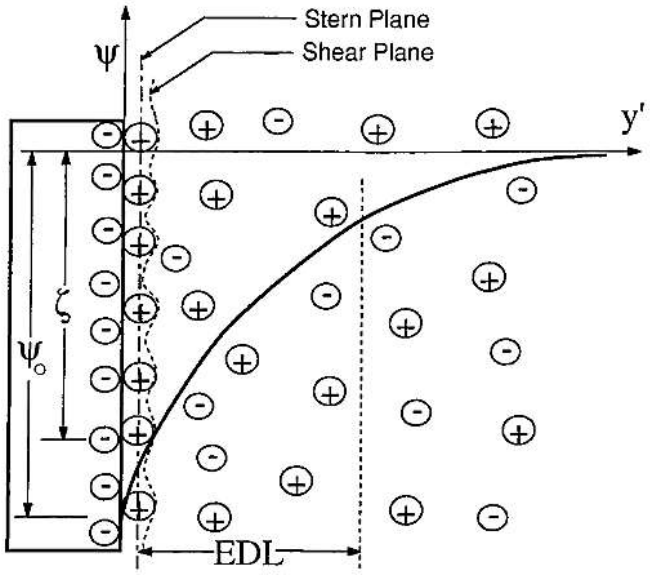

Figure 6: Electric double layer and zeta potential [31]

In the presence of an electric field orthogonal to the EDL surface, with an applied potential that is significantly larger than the zeta potential, the diffuse layer is stripped away. This is the case with most electrode surfaces in EHD pumping. However, the remaining wall surfaces will still retain their EDL. Studies have shown that the presence of the EDL serves as an electroviscous resistance that opposes any pressure driven flow [32]. All EHD pumping techniques in small scales would, therefore, need to generate greater forces on the fluid in order to overcome the EDL flow resistance.

In low conductivity dielectric fluids, the EDL length can be on the order of microns [33], which means that sufficiently small micro-scale EHD pumps using such fluids, as is the case for ion drag and conduction pumping, will be affected by the presence of the additional space charge, as well as a potentially non-negligible zeta potential compared with the applied pumping voltage.

Additional potentially adverse effects at small-scales include significant Joule heating relative to the volume of the fluid, which can give rise to potentially unwanted gradients in the fluid's electrical properties [34], and induced buoyancy forces or unexpected electro-thermal

induction flow [35]. In general, Joule Heating is the main cause of low power efficiency in EHD pumping devices in all size scales, but in small scales the effect can become more severe. Lastly, localized electrochemical reactions, between the electrode material and the fluid, can be enhanced by the application of an electric field at such small scales, which can cause a more rapid erosion of the electrodes or generate unwanted reaction products in the fluid [36].

1.1.5 Early studies on conduction pumping

This section focus on the historical references of EHD conduction pumping rather than the state of the art. Since EHD conduction is the youngest of the EHD pumping techniques, all studies of EHD conduction driven single phase internal flows are more recent compared to the other pumping techniques. EHD conduction was first proposed as a separate EHD pumping technique after a few experimental studies of induction pumping yielded unexpected results [9]. As an example, in a study of high frequency, high voltage induction pumping initial theories about the existence of heterocharge layers began to emerge [37], but it was merely assumed to be a side effect of induction pumping.

With the introduction of the EHD conduction model and first proper experiments [38], further macro-scale studies focused on investigating different electrode designs of EHD conduction pump [39, 40] in order to determine the its pressure generation performance. Some of these performance curves are given in Figure 7. Note that this figure shows performance information for conduction pumps with only one pair of electrodes of any given design. In general, pressure generation of EHD conduction pump increases in a nearly linear fashion with the inclusion of additional electrode pairs [39], as long as there is sufficient spacing between the pairs such that their individual electric fields do not interfere with each other [22]. These early studies

confirmed that there is a quasi-linear relation between the number of electrode pairs used and the final pressure generation values of the EHD conduction pump [9].

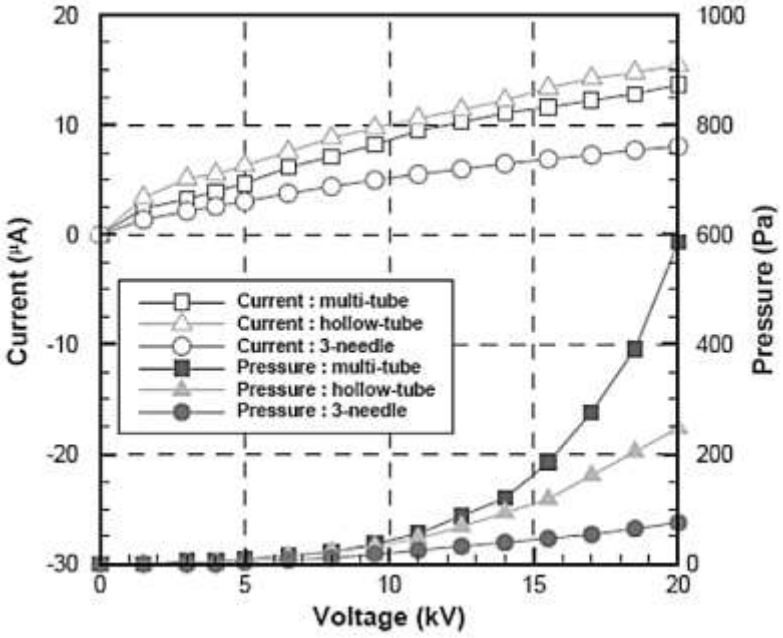

Figure 7: EHD conduction pumping performance of selected high voltage electrode designs [39]

In addition to different electrode designs, different working fluids were also tested by Ashjaee and Mahmoudi [41] for static pressure generation in a similar macro-scale channel using the same electrode design for all fluids. Their study showed the range of electrical conductivities that are most favorable for EHD conduction. The schematic of their pressure measurement apparatus is presented in Figure 8. The pressure measurement was carried out by a manometer with 10 degree inclination with respect to horizontal.

Four fluids, N-Hexane, Shell-Diala AX transformer oil, Kerosene and Nynas Transformer oil-Nytro 10-GBN were tested. The EHD generated pressure heads as a function of applied voltage with 10-GBN and shell Diala AX as working fluid are shown in Figure 9. The EHD pumping pressure generation was quadratic function of applied voltage and the maximum was l09 Pa with the Shell Diala- AX at 23kV applied voltage, with 0.92W power consumption. The generated

pressure head with Kerosene as working fluid was lower and there was no noticeable pressure head generation for N-Hexane. Their experimental results shows that pumping performance depends on electrical conductivity, electrical permittivity, and primarily viscosity of working fluid. Specifically, it increases with the charge relaxation time and the order of magnitude of electric conductivity.

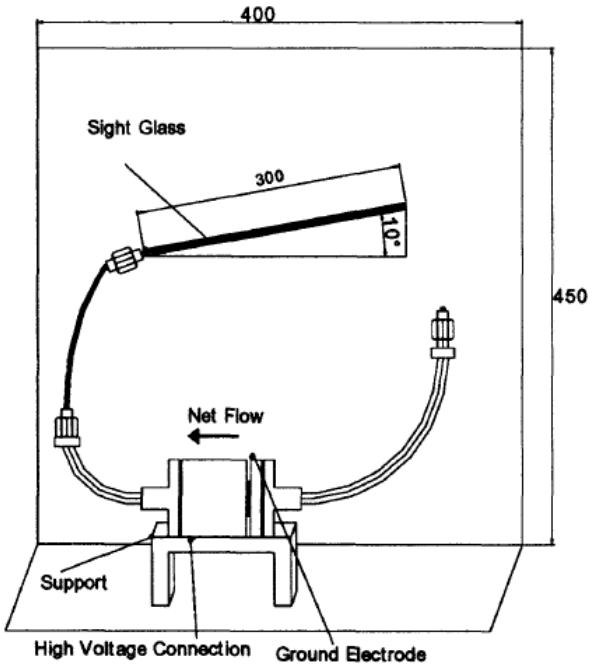

Figure 8: Pressure measurement apparatus for EHD static pump (All dimension in mm) [41]

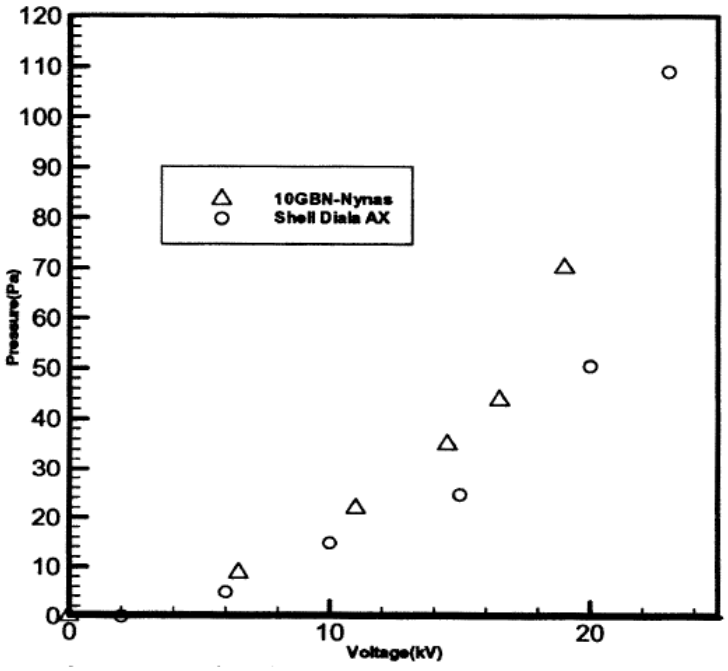

Figure 9: Pressure head generation as a function of applied voltage for Nynas Transformer oil-Nytro 10-GBN and Shell Diala AX transformer oil [41]

1.2 Heat transfer enhancement with phase change phenomenon

1.2.1 Pool boiling heat transfer

Boiling at the surface of a body immersed in an extensive pool of liquid is generally referred to as pool boiling. This type of boiling process is encountered in a number of applications including metallurgical quenching processes, flooded tube and shell evaporators (with boiling on the shell side), immersion cooling of electronic components, and boiling of water in a pot on the burner of a stove [42]. The regimes of pool boiling are most easily understood in terms of the so-called boiling curve: a plot of heat flux q" versus wall superheat T_w-T_{sat}. The first classical pool boiling curve was determined in an early investigation of pool boiling conducted by Nukiyama [43]. Figure 10 shows a typical pool boiling curve and the associated pool boiling regime if the boiling surface temperature is controlled and slowly increased.

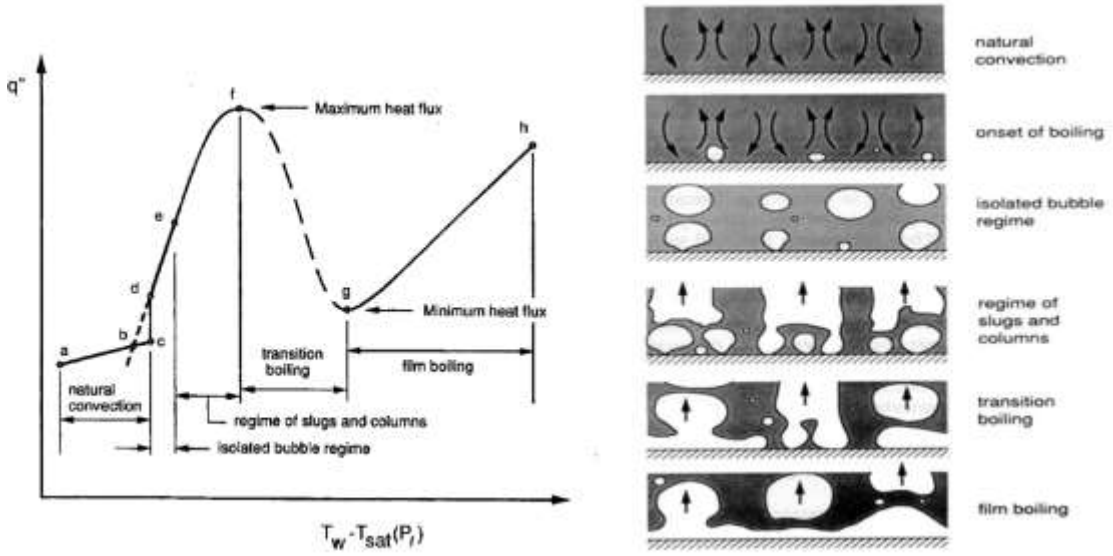

Figure 10: Pool boiling curve and regimes for a controlled boiling surface temperature [42]

At very low wall superheat levels, no nucleation sites may be active and heat may be transferred from the surface to the ambient liquid by natural convection alone. The heat transfer coefficient associated with natural convection is relatively low, and q" increases slowly with $T_w - T_{sat}$. Once nucleate boiling is initiated, any further increase in wall temperature cause the system operation point to move upward along the d-f of the curve in Figure 10. This portion of the curve corresponds to the nucleate boiling regime. Increasing the wall temperature ultimately results in a peaking and roll-over of the heat flux. The peak value of heat flux is called the critical heat flux (CHF), designated as point f in Figure 10.

If the wall temperature is increased beyond the critical heat flux condition, a regime is encountered in which the mean overall heat flux decreases as the wall superheat increases. This regime, corresponds to segment f-g on the boiling curve shown in Figure 10. The transition boiling regime is typically characterized by rapid and severe fluctuations in the local surface heat flux and/or temperature values (depending on the imposed boundary condition) [42]. These fluctuations

occur because the dry regions are generally unstable, existing momentarily at a given location before collapsing and allowing the surface to be rewetted.

The vapor film generated during transition boiling can be sustained for longer intervals at higher wall temperatures. As this trend continues, eventually a point is reached at which the surface is hot enough to sustain a stable vapor film on the surface for an indefinite period of time. The entire surface then becomes blanketed with a vapor film, thus making the transition to the film boiling regime. This transition occurs at point g in Figure 10. Within the film boiling regime, the heat flux monotonically increases as the superheat increases. This trend is a consequence of the increased conduction and/or convection transport due to the increased driving temperature difference across the vapor film [T_w–T_{sat}]. Radiative transport across the vapor layer may also become important at higher wall temperature [42].

The mechanism responsible for the critical heat flux has been the subject of considerable investigation and debate over the past six decades. Kutateladze [44] was among the first investigators to note the similarity between flooding phenomenon in distillation columns and the CHF condition in pool boiling. In a column of this type, vapor rich in the more volatile components flows upward while liquid rich in the less volatile components flows downward. If the relative velocity of the two streams becomes too large, the flow become Helmholtz unstable, causing the vapor drag on the downward moving liquid to increase to the point that the flow of liquid is impeded. Liquid that is then unable to move downward and accumulates at the top of the column, which is then said to be “flooded” [42]. Based on the similarity between the CHF condition and column flooding, Kutateladze [44] used dimensional analysis arguments to derive the following relation for the maximum heat flux.

$$q''_{\max} = C_K \rho_v^{1/2} h_{lv} \left[g(\rho_l - \rho_v)\sigma \right]^{1/4} \tag{18}$$

Zuber [45] included Taylor wave motion and Helmholtz instability as key elements in his model of the CHF mechanism. Zuber's model analysis, as refined by Lienhard and Dhir, is based on the following idealizations [42]:

1) The critical heat flux is attained when the interface of the large vapor columns leaving the surface becomes Helmholtz unstable.
2) The columns leave the surface in a rectangular array as shown in Figure 11. The centerline spacing of the columns coincides with nodes of the most dangerous wavelength associated with the two-dimensional wave pattern for Taylor instability of the horizontal interface between a semi-infinite liquid region above a layer of vapor.
3) The column radius is equal to $\lambda_D/4$, where λ_D is the spacing of the columns as predicted by Taylor instability analysis.
4) The Helmholtz unstable wavelength imposed on the columns is equal to the Taylor wave node spacing λ_D.

Zuber's original model resulted in a relation for CHF identical to the following equations:

$$q''_{\max} = 0.131 \rho_v h_{lv} \left[\frac{\sigma(\rho_l - \rho_v) g}{\rho_v^2} \right]^{1/4} \tag{19}$$

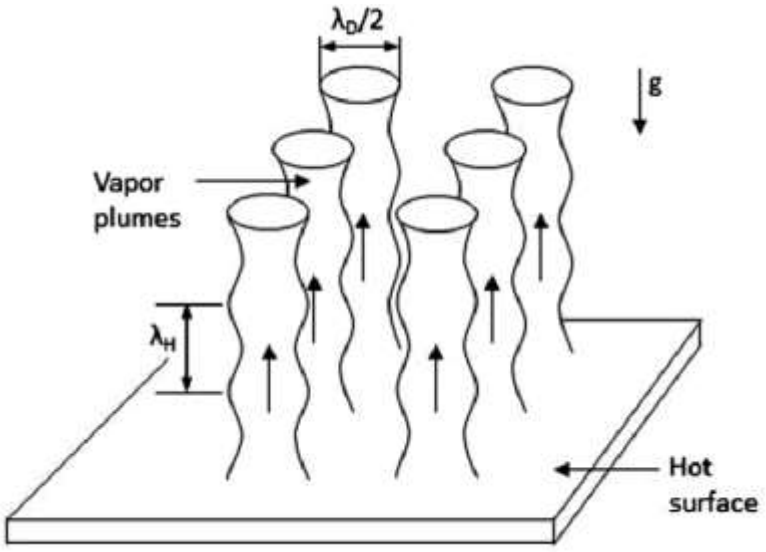

Figure 11: Vapor Column spacing in the Zuber critical heat flux model [42]

Nucleate pool boiling heat transfer data have been obtained for a number of pure fluids at different system pressure levels. Correlations of such data have typically been used to predict nucleate boiling heat transfer in engineering systems and heat exchangers. Among many correlations of nucleate pool boiling, Rohsenow's correlation [46], shown in equation 20, probably is the most commonly used one, which is based on analogies with force convection processes

$$\frac{q''}{\mu_l h_{lv}}\left[\frac{\sigma}{(\rho_l-\rho_v)g}\right]^{1/2}=\left(\frac{1}{C_{sf}}\right)^{1/r}\mathrm{Pr}_l^{-s/r}\left[\frac{c_p[T_w-T_w(P_l)]}{h_{lv}}\right]^{1/r} \tag{20}$$

Originally, values of r=0.33 and s=1.7 were recommended for this correlations. Subsequently, Rohsenow recommended that for water only, s be changed to 1.0. It is generally recommended that, whenever possible, an experiment be conducted to determine the appropriate value of C_{sf} for the particular solid-liquid combination of interest. If this is not possible, a value of C_{sf} = 0.013 is recommended as a first approximation.

Despite the high heat transfer coefficients often associated with normal pool boiling, considerable effort has been expended to enhance pool boiling heat transfer. One method of great interest is the modification of the pool boiling surface since it has been confirmed that surface characteristics substantially affect the nucleate pool boiling heat transfer phenomenon. From the discussion of the basic mechanisms of pool boiling, it is clear that nucleate boiling is most effective when there exists an abundance of cavities on the surface to act as nucleation sites. It is also clear that the cavities are most likely to become active nucleation sites if they effectively trap vapor and/or gas in them when the system is filled and during periods when the system is inactive. Thus, the two of the most widely-studied ways of enhancing nucleate boiling are: (1) creation of special surfaces having artificially-formed cavities designed to efficiently trap vapor and (2) increasing the surface roughness [42].

For the first way, many of the more recent efforts to enhance nucleate boiling have employed surface structures designed to produce re-entrant or doubly re-entrant cavities. The main objective in designing the cavities in this manner is to produce a convex liquid-vapor interface, as seen from the liquid side, when liquid penetrates into the cavity. This assures that the vapor trapped in the cavity will withstand at least some subcooling of surrounding solid surface without condensing. Surfaces with such artificially produced cavities are generally fabricated in one of two ways. One approach is to fuse metal particles or small drops of molten metal to a flat metal surface to create a thin layer which provides an irregular matrix of re-entrant cavities. The second method first produces a tube or surface having fin-like protrusions which ae subsequently flattened upset or bent over to form re-entrant cavity structures [42].

Yilmaz et al [47] systematically compared the performance of three enhanced surfaces of these types. The surface constructions and experimentally determined pool boiling curves for the three surfaces considered by these investigators are shown in Figure 12. It can be seen that the boiling curves for all three of the enhanced surfaces are shifted well to the left of that for the plain tube, implying a substantial enhancement.

For the second way, In order to increase surface roughness, various techniques have been proposed such as porous coatings and mechanical surface machining. In principle, all of these surface treatment techniques create macroscopic or microscopic geometries on surfaces, which serve to increase heat transfer area, surface roughness as well as active nucleation site density during pool boiling.

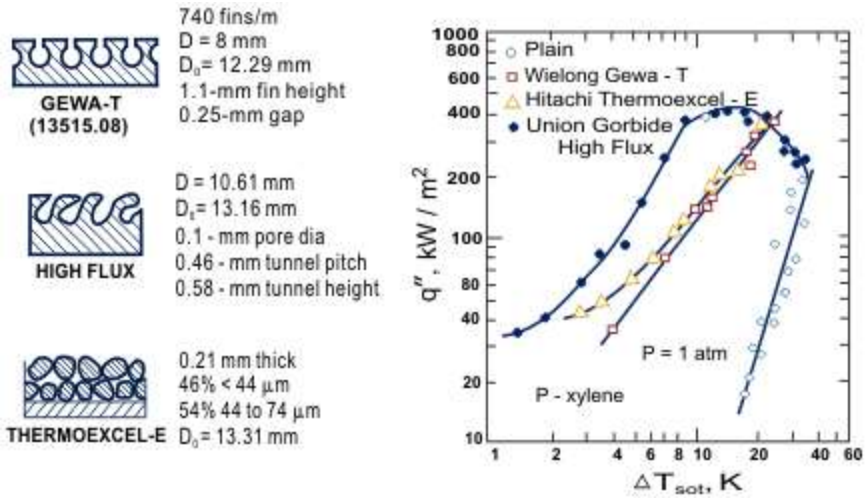

Figure 12: Schematic representation of the cross sections of three enhanced surfaces for nucleate boiling and comparison of their pool boiling curves with that for a plain tube [47]

Theoretical and experimental work [48-53] has been done recently for fundamental understanding of the effect of surface roughness on pool boiling. In chapter 4, the effect of the surface roughness on pool boiling heat transfer coefficient was investigated by comparing the experimental results for surfaces with 1 micron and 10 micron surface roughness with the Rohsenow correlation [46].

The research on the effect of surface inclination angle on pool boiling heat transfer and CHF has been receiving increased attention recently. Nishikawa et al. [54] was the first to carry out a detailed study on surface orientation effect on pool boiling and tried to give a theoretical interpretation of their experimental data. Their experimental results indicated that above a certain threshold heat flux level, the pool boiling curves for all orientations are virtually identical. Below this threshold value the curves differ significantly for the different surface orientations. The upward facing surface resulted in the highest superheat for a given heat flux, whereas in the downward facing positon, the surface superheat was the lowest. This threshold value corresponds

approximately to the transition from the isolated bubble regime to the regime of slugs and columns. This transition is sometimes referred to as the Moissis-Berenson transition [55].

$$q''_{MB} = 0.11\rho_v h_{lv}\theta^{1/2}\left(\frac{\sigma g}{\rho_l - \rho_v}\right)^{1/4} \tag{21}$$

Where θ is the liquid contact angle. This relation agreed well with visual observations of the transition between the isolated bubble regime and the regime of slugs and columns.

Chang and You [56] studied the nucleate boiling of FC-72 on a smooth 1cm×1cm copper surface with various surface orientations. They found that the pool boiling heat transfer coefficient increased as surface orientation increased from 0° to 90º and attributed this phenomenon to an increase in the number of active nucleation sites with the increase in the surface angle. On analyzing the effect of inclination angle on saturation pool boiling of HFE-7100 on a smooth 10 ×10 mm copper surface, simulating a microelectronic chip, El-Genk and Bostanci [57] found that for $\theta \leqslant 90°$ and surface superheat, $\Delta T_{sat} > 20$ K, nucleate boiling heat flux decreases with increased θ, but increases with θ for $\Delta T_{sat} < 20$ K. Similarly, at higher inclinations and $\Delta T_{sat} > 13$ K, nucleate boiling heat flux decreases with increased inclination, but at lower surface superheats the trend is inconclusive. They [58] then studied the combined effects of surface orientation and sub-cooling. Priarone [59] obtained pool boiling data at atmospheric pressure with both saturated FC-72 and HFE-7100. For both fluids, the orientation angle of the copper surface from the horizontal plane was varied from 0° to 175°. This result obtained confirmed some of the effects of heater orientation on heat transfer coefficient reported in the literature: in the low-heat-flux nucleate boiling region, the heat transfer coefficient increases markedly with orientation angle; for higher heat flux values, the effect is evident only for angles greater than 90° and the heat transfer coefficient diminishes as the angle increases. Howard and Mudawar [60] studied near-saturated pool boiling at various

surface orientations in order to determine the critical heat flux trigger mechanism associated with each orientation, based on the vapor behavior observation just prior to CHF. They suggested that surface orientations can be divided into three regions: upward-facing (0-60°), near-vertical (60-165°) and downward-facing (>165°) and each region is associated with a unique CHF trigger mechanism. They also proposed a near-vertical CHF model incorporating classical two-dimensional interfacial instability theory, a separated flow model, an energy balance, and a criterion for separation of the wavy interface from the surface at CHF. A few investigators have attempted to correlate the orientation effect on CHF. Vishnev [61] was the first to correlate this effect and his correlation is still widely utilized. Later, Chang and You [56], El-Genk and Bostanci [57] also developed surface orientation correlation for CHF. Their correlations were used in this study for comparison with experimental data.

1.2.2 Pool boiling heat transfer enhancement with enhanced surface

Most previous techniques used for surface structure modification are related to micro-sized dimensions. However, recent advances in nano-technology have allowed the development of nano-textured surfaces with conspicuous structures [62] and extensive research has been carried out to investigate the pool-boiling enhancement due to these surfaces. Many have found favorable boiling heat transfer augmentation results and demonstrated that nano-textured surfaces lead to the increase of some important boiling parameters such as nucleation site density, bubble departure frequency and therefore result in a significant increase in the pool boiling heat transfer coefficient.

A brief review of work done in this area is given in the paragraphs that follow. Forrest et al. [63] demonstrated significant enhancement in the pool boiling critical heat flux and nucleate heat transfer coefficient by applying nanoparticle thin-film coatings to heater surface using a layer-by-layer assembly method. Lee et al. [62] reported their experimental study on water nucleate

boiling heat transfer coefficient and long term performance with nano-porous surface fabricated by anodizing technique. They also found that the nucleate boiling heat transfer of nano-porous coating surfaces appeared enhanced compared to that of non-coating surfaces, especially at low heat flux conditions. Vemuri and Kim [64] conducted an experimental study on the nucleate pool boiling heat transfer of nano-porous surface made of aluminum-oxide (thickness is 70 nm) in saturated FC-72 dielectric fluid. Based on the experimental data obtained, they found that the incipient wall superheat for a nano-porous surface was reduced by 30%, compared with a bare surface. Hendricks et al. [65] obtained enhanced pool-boiling heat fluxes at reduced wall superheat on nanostructured surfaces created with micro-reactor assisted nanomaterial deposition. In their study, they attributed the augmented nucleate boiling heat transfer performance to increased vapor entrapment volume and active nucleation site density as well as the capillary pumping effect resulting from nano-porous structure.

Ahn et al. [66] investigated pool boiling on multi-walled carbon nanotube (MWCNT) forests using 3M^{TM} Performance Fluid PF-5060 as the working fluid and their results show that the Type A MWCNT forests enhanced critical heat flux by as much as 62% compared to control experiments performed on bare silicon. Ujereh et al. [67] performed pool boiling experiments to assess the impact of silicon coating and copper substrates with carbon nanotubes (CNT) on pool boiling performance. With dielectric liquid FC-72 as the working fluid, they found that the large incipient temperature and ensuing temperature drop due to the low contact angle of FC-72 on silicon and copper was completely eliminated and the nucleate boiling heat transfer coefficient and critical heat flux were greatly enhanced when the surfaces were fully coated with CNTs. Chen et al. [68] reported that nanowires made of silicon and copper were utilized for pool boiling in saturated water. They observed that both critical heat flux and heat transfer coefficient increased

by more than 100%. They attributed such enhancement to some unique properties of nanowires, such as high nucleate site density, superhydrophilicity, and enhanced capillary pumping effect. Wu et al. [69] performed an experimental study to investigate the nucleate pool boiling and critical heat flux of water and FC-72 dielectric liquid on a hydrophilic, titanium oxide nanoparticle-modified surface. The results showed that the TiO2 coated surface increased critical heat flux by 50.4% and 38.2% for water and FC-72, respectively. Launay et al. [70] experimentally studied the boiling heat transfer on various hybrid micro-nano structured thermal interfaces using PF-5060 and deionized water as working fluids. Using 3D microstructure and deionized water, they obtained a maximum heat flux of 130W/cm^2. Im et al. [71] also observed enhanced critical heat flux and reduced incipience superheat of pool boiling using copper nanowire surfaces compared to baseline experiments, which were performed using a bare surface without nanowires.

1.2.3 Convective flow condensation heat transfer

Convective condensation heat transfer is an important area of research and has many practical applications, such as in heat exchangers in commercial refrigeration systems, building and automotive air-conditioners, nuclear reactors and power plants, chemical process and food production industries, and the thermal management system of electronic devices. The characterization of associated two-phase flow, such as its flow regimes (shown in Figure 13), pressure gradient and heat transfer coefficient, is critical to the design of efficient and cost-effective cooling systems.

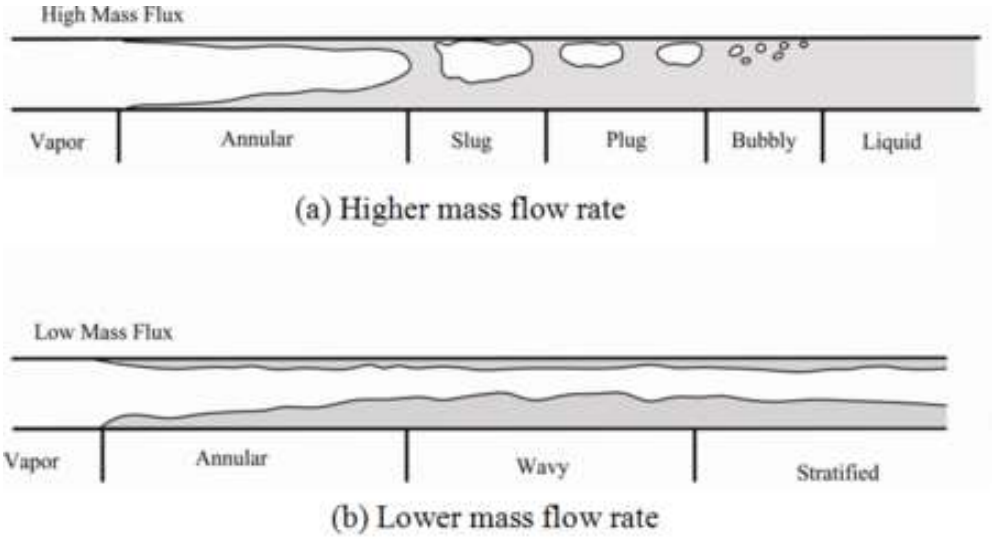

Figure 13: Convective flow condensation regimes [42]

Two-phase flow is generally more complicated physically than single-phase flow as it is also affected by interfacial tension forces and the exchange of momentum between the liquid and vapor flows. Various flow regimes and conditions that exist in two-phase flow make its generalized analytical treatment and numerical simulation a challenging task. As a result, research efforts focus on exploring the development of simplified models of two-phase flow mechanisms which are typically based on a mixture of semi-theoretical arguments and empirical evidence [42].

The so-called homogeneous flow model can be considered to be the simplest model of gas-liquid two-phase flow, in which the vapor and liquid velocities are assumed to be equal. It is a special case of the separated flow model and sometimes is also called the friction factor model or fog flow model. It is usually only used for the approximation of bubbly flow and mist flow, in which cases the gas and liquid velocities are similar.

For more general separated flow cases in which the gas and liquid velocities are different, the pioneering work of Martinelli and his co-workers in the 1940s provided the first widely successful methods [72, 73] for predicting two-phase multipliers, and established an analytical foundation on which much of the subsequent work on two-phase flow has been built [42]. The

dependence of two-phase multipliers on Martinelli parameter X can be made more concrete by considering the separate cylinders model of gas-liquid flow described by Wallis [74].

Convective condensation in a horizontal circular tube is probably the most common configuration that is encountered in the condensers of air-conditioning and refrigeration systems as well as Rankine power cycles. The convective condensation in this study is also based on a configuration of this type. In fact, for many applications in which condensation occurs at low to moderate pressure, the void fraction is relatively high even at low qualities near the end of the condensation process. As a result, flow regimes other than annular flow may occur, but they typically exist during only a small portion of the heat transfer process. Thus, prediction of the condensation heat transfer coefficient for annular flow is obviously of primary importance. Most efforts to develop methods for predicting internal convective condensation heat transfer have focused on annular flow.

A number of investigators have proposed correlations of predicting the condensation heat transfer coefficient for annular flow conditions. For horizontal tubes at low vapor velocities, liquid that condenses on the upper portion of the inside tube wall tends to run down the wall towards the bottom, this stratified-annular flow condition is observed most commonly at low condensation rates. Chato [75] developed a detailed analytical model of the heat transfer, as shown in equation 22 for these circumstance and his results implied that this type of flow configuration exists for inlet vapor Reynolds numbers less than 35000.

$$h = 0.728 K_C \left[\frac{g\rho_l(\rho_l - \rho_v)k_l^3 h_{lv}^{'}}{\mu_l(T_{sat} - T_w)D} \right]^{\frac{1}{4}} \tag{22}$$

$$h_{lv}' = h_{lv}\left[1 + 0.68 \frac{c_p(T_{sat} - T_w)}{h_{lv}} \right] \tag{23}$$

At moderate to high inlet vapor velocities, annular flow is established almost immediately at the inlet, and persists over most of the condensation process. Travis et al. [76] proposed the following relation for the local heat transfer coefficient for annular flow convective condensation.

$$\frac{hD}{k_l} = \frac{0.15\,\mathrm{Pr}_l\,\mathrm{Re}_l^{0.9}}{F_T}\left[\frac{1}{X_{tt}} + \frac{2.85}{X_{tt}^{0.476}}\right],\ \mathrm{Re}_l = \frac{G(1-x)D}{\mu_l} \tag{24}$$

$$F_T = 5\,\mathrm{Pr}_l + 5\ln\{1+5\,\mathrm{Pr}_l\} + 2.5\ln\{0.0031\,\mathrm{Re}_l^{0.812}\},\ \mathrm{Re}_l > 1125 \tag{25}$$

$$= 5\,\mathrm{Pr}_l + 5\ln\{1+\mathrm{Pr}_l(0.0964\,\mathrm{Re}_l^{0.585} - 1)\},\ 50 < \mathrm{Re}_l \le 1125 \tag{26}$$

$$= 0.707\,\mathrm{Pr}_l\,\mathrm{Re}_l^{0.5},\ \mathrm{Re}_l \le 50 \tag{27}$$

Based on a purely empirical approach, Shah [77] has proposed the following correlation as a best fit to available convective condensation heat transfer data for round tubes.

$$\frac{h}{h_{lo}} = (1-x)^{0.8} + \frac{3.8x^{0.76}(1-x)^{0.04}}{(P/P_C)^{0.38}} \tag{28}$$

$$h_{lo} = 0.023\left(\frac{k_l}{D}\right)\left(\frac{GD}{\mu_l}\right)^{0.8}\mathrm{Pr}_l^{0.4} \tag{29}$$

In addition, Chen et al. proposed a comprehensive film condensation heat transfer correlation based on analytical and theoretical results from the literature.

The discussion of convective condensation above has focused on circular flow passages with diameters larger than 5mm, a typical geometry and size range of condensers used in many conventional technologies. However, over the past two decades, there has been rising interest in applications that involve two-phase flow and convective condensation in mini-channels and micro-channels, as the condensation heat transfer could be significantly enhanced with decrease in the size of flow passage. For a given fluid at a specified quality and saturation pressure, the film

thickness decreases and the heat transfer coefficient increases as the tube diameter is reduced. These general trends are, in fact, observed in the performance of high-performance compact condensers used in automotive air-conditioning applications. Recent advances in manufacturing technologies such MEMS lithographic fabrication methodologies and micromachining have made it possible to fabricate condensers with passage dimensions as small as a few hundred nanometers [42].

As passage size is reduced, the flow exhibits specific features that are different from those for macroscale condensing flows. The Reynolds number associated with the flow becomes progressively smaller and the two-phase flow would be expected to be in the laminar-laminar regime. In general, it is expected that the two-phase flow in micro-channels will be dominated by the interplay among flow inertia, viscous forces (shear), and surface tension forces. Gravity induced buoyancy is expected to play a much weaker role. Similar to the convective condensation in conventional applications. The data from several experimental investigations indicate that annular flow spans an increasing portion of the condensation process as the hydraulic diameter of the passage decreases and thus exists during much of the internal flow condensation processes in micro-condensers. As a consequence, annular flow has also been a main focus of efforts to empirically and theoretically predict convective condensation heat transfer in micro-channels.

1.3 Heat transfer enhancement with EHD conduction pumping and phase change phenomenon

1.3.1 Channel flow generation and convective flow boiling enhancement with EHD conduction pumping

Bryan and Seyed-Yagoobi [78] conducted the first study on EHD conduction driven two-phase flows, they investigated the heat transfer performance enhancement of a mono-groove heat

pipe using EHD conduction pumping. Their study showcased the ability of macro-scale EHD conduction pumps to enable recovery from dryout conditions, as shown in Figure 14. In this figure times 1 and 2 define the span between the activation of the EHD pump at its maximum voltage and achieving a steady state, recovered temperature.

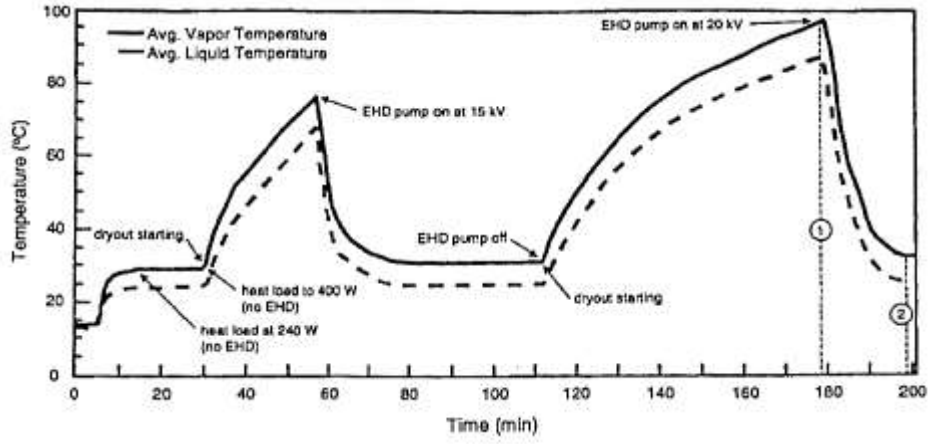

Figure 14: Time line of average evaporator vapor and liquid temperatures [78]

Jeong and Didion [79] investigated the performance characteristics of an electrohydrodynamic conduction pump in two-phase thermal control loops and presented the results of an extensive experimental matrix examining the operational performance. Specifically, two EHD conduction pump sets (EHD pump-1, EHD pump-2), consisting of six electrode pairs, were built and installed alternatively in two two-phase loops (EHD loop-1, EHD loop-2) with condenser and high heat flux evaporator. Deaerated HFC-134a and unprocessed HFC-134a were used as the working fluid to investigate the influence of noncondensable gas in fluid.

Their experimental results, shown in Figure 15 and 16, indicated that both working fluid temperature and projected electrode area can significantly impact the generated pressure head. Lower EHD pump operating temperature and bigger projected electrode area provide a higher generated pressure head by increasing heterocharge layer thickness and area, respectively. Deaeration of the working fluid also significantly enhanced the pressure generated by the EHD

conduction pump. In addition, the diabatic test results showed that the tube diameter between the evaporator and condenser has great influence on the pressure loss and mass flow rate in a two-phase loop with dryout flow regime in the evaporator. The larger diameter improved loop heat transport capability making the diameter an important loop optimization parameter.

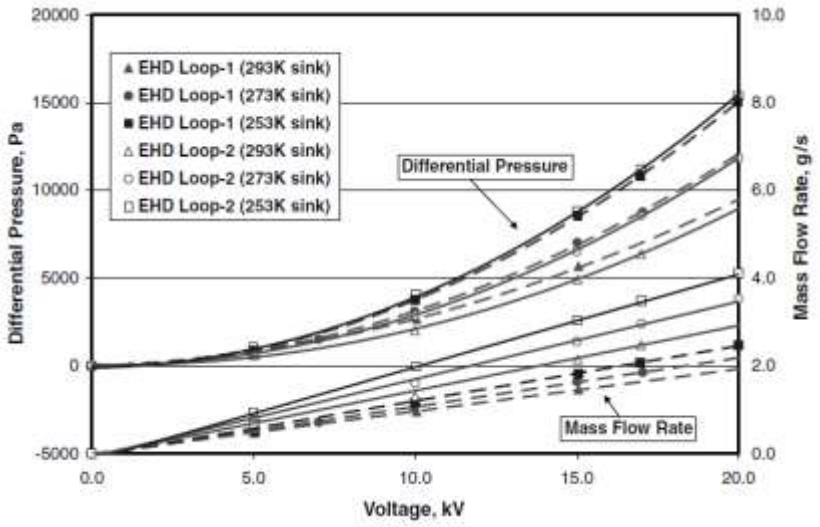

Figure 15: Pressure generation and mass flow rate of EHD pump-2 as a function of applied voltage with various sink temperatures (unprocessed HFC-134a used) [79]

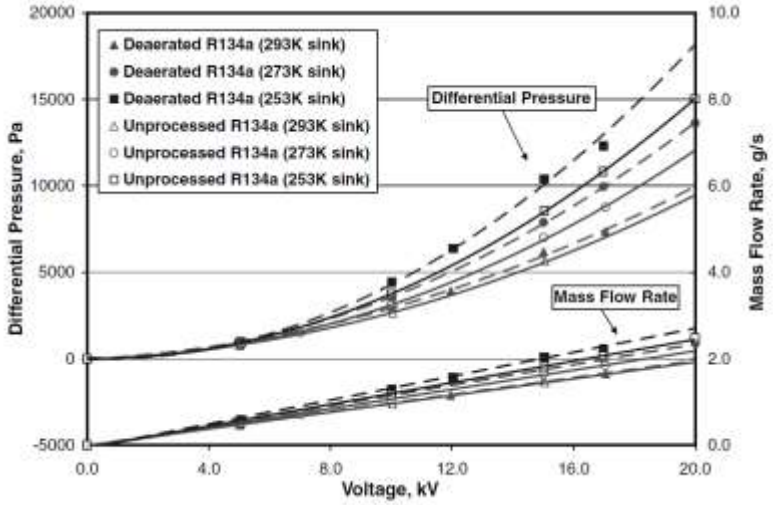

Figure 16: Pressure generation and mass flow rate of EHD pump-2 as a function of applied voltage with various sink temperatures for unprocessed and deaerated HFC-134a in EHD loop-1 [75]

Jeong and Didion [80] further showed the effect of voltage and working fluid temperature on the critical heat flux for such a setup, as shown in Figure 17.

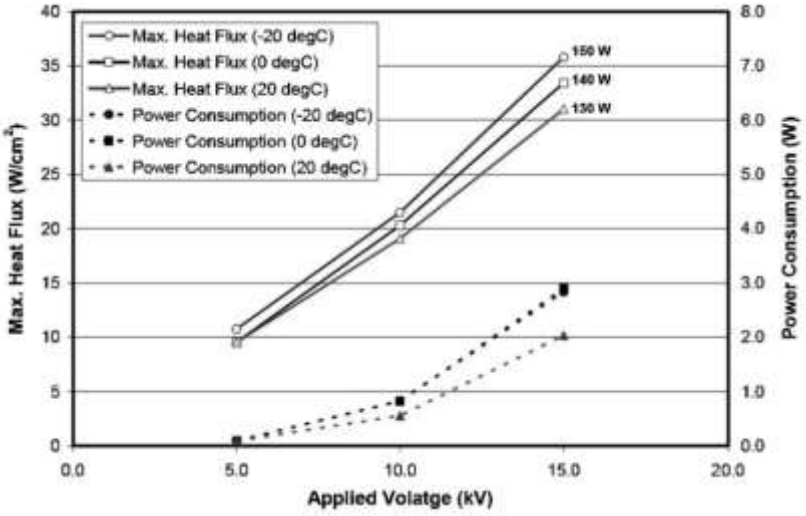

Figure 17: CHF and power consumption vs. applied voltage at different temperatures [80]

Conduction pumping generation depends primarily on the intensity of the imposed electric field, so the magnitude of the applied voltage can be significantly reduced in micro-scale pumps. The simplicity of conduction pumps makes them well-suited for pressure generation in micro-scale fluid and heat transfer devices. Research on heat transport in microscale has been generating much interest in recent years due to the development of state-of-the-art high-powered electronics used in aerospace and terrestrial applications and the large amount of heat produced during their operation. Experimental work in the area of EHD conduction driven micro-scale internal flows has been fairly limited due to the relative age of this pumping technique [9]. Nevertheless, initial studies of micro-scale single phase flows were conducted, which is briefly reviewed in the following.

Pearson and Seyed-Yagoobi [81] for the first time experimentally studied the flow and pressure generation of two EHD conduction pumps embedded within rectangular meso- and

micro-channels. Both pumps had micro-scale electrode dimensions much less than 1mm. The pump design is shown in Figure 18 and details of dimensions are in Table I.

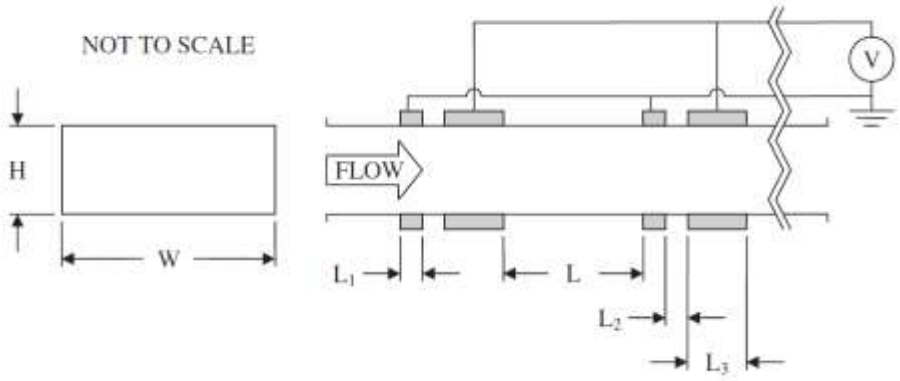

Figure 18: Schematic of flow channel embedded with EHD conduction pump [81]

Table I: EHD pump dimensions corresponding to Figure 18

Dimension	Meso-scale Pump	Micro-scale Pump
W (mm)	12.7 ± 0.3	12.7 ± 0.3
H (mm)	1.016 ± 0.051	0.254 ± 0.026
L1 (mm)	0.254 ± 0.013	0.051 ± 0.003
L2 (mm)	0.254 ± 0.026	0.051 ± 0.013
L3 (mm)	0.914 ± 0.102	0.178 ± 0.013
L4 (mm)	3.175 ± 0.254	0.794 ± 0.077
Number of electrode pairs	10	10

For the meso-scale pump, the entire span of possible pressure loads were studied, ranging from an infinite load to the minimum pressure load and the corresponding pump performance curves at nominal applied voltages of 1-4 kV are shown in Figure 19. The infinite load corresponds to the static pressure generation of the pump and lies on the x axis; the minimum load is shown by the bold, curved line. The author mentioned that, even with the valve closed for the so-called "static

case", there was still expected to be significant circulation of fluid within the pumping section due to the highly non-uniform electric field and electric body force within the micro-channel, even though the net flow rate of fluid through the pump is zero. The pump performance shows an inverse and approximately linear relationship between the flow generation and the pressure load.

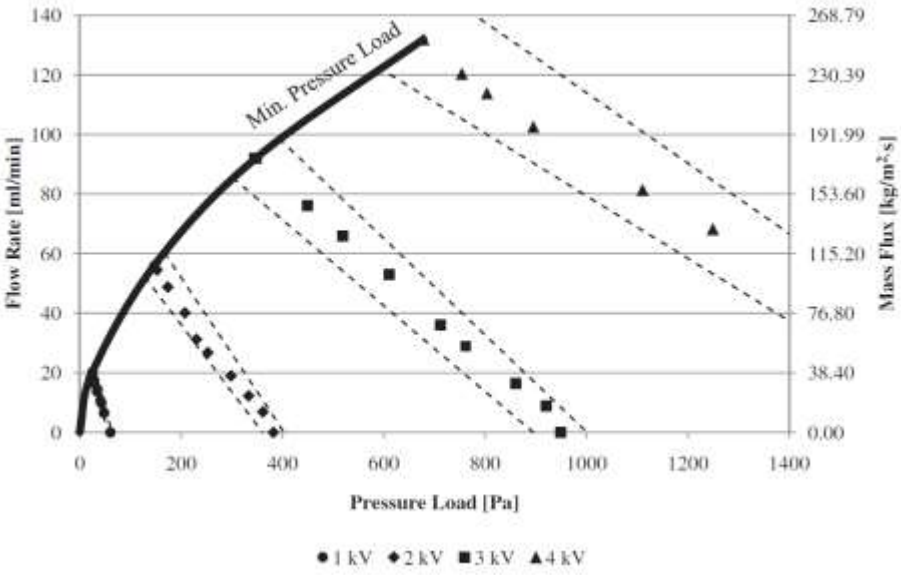

Figure 19: Pump performance curve for the meso-scale pump [81]

Further studies were conducted by Kano and Nishina [82] on planar 120μm wide ground or positive voltage electrodes versus a negative voltage 21mm by 16mm rectangle cover electrode in a 100μm microchannel using HFE-7100. These showed that EHD conduction pumping can be initiated using negative applied potentials on the electrode with the higher wetted surface area, as long as the required overall field strength is reached via grounding or applying a positive potential to the smaller electrodes.

The same concept was adapted into a radial configuration by Mahmoudi and Adamiak [83]. They proposed a single-stage axisymmetric conduction micropump in a vertical configuration. The micropump consisted of four components: high voltage ring electrode, grounded disk-shaped electrode, insulator spacer, and inlet/outlet ports. The high-voltage electrode and grounded

electrode of the device, which are shown in Figure 20, were patterned on two separate commercial LCP substrates with 30 μm copper cladding using standard lithographic techniques.

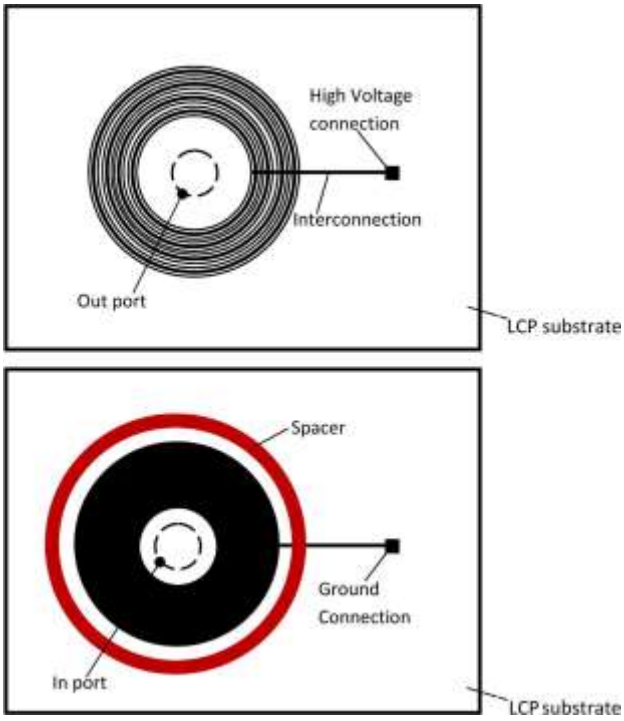

Figure 20: Top view of (a) high-voltage annulus electrodes and (b) grounded electrode patterned on two separate substrates [83]

The static pressure generation of the micropump was measured at various applied voltages using three different dielectric liquids: 10-GBN Nynas, Shell Diala AX transformer oils, and N-hexane. To further verify the experimental results, a 2-D axisymmetric model of the micropump was also developed based on a double species conduction model. The pressure head generation predicted numerically was compared with experimental result and is presented in Figure 21. The conduction pumping effect started at the average field strength of 1 V/μm, and a maximum 101 Pa pressure generation was achieved at the average field strength of 5.24 V/μm. Their numerical static pressure generations prediction were generally in a good agreement with the experimental data with an average 8% deviation except for an overestimation at 10 V/μm local field strength (1500

VDC). They believed that this overestimation was related to the reversed pressure generation due to the initiation of the direct ion injection.

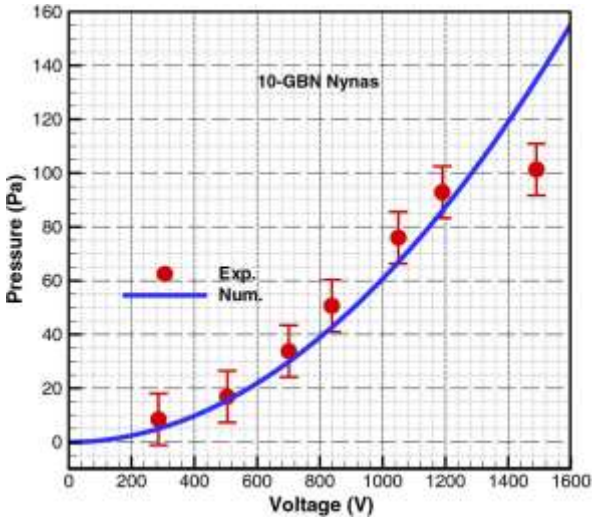

Figure 21: Comparison of calculated and experimental static pressures for conduction micropump using 10-GBN Nynas oil transformer [83]

Pumping of micro-scale internal two-phase flows is of immense interest for the electronics cooling industry, due to the high heat flux removal capabilities. Several passive two-phase flow pumping solutions involving capillary action have been investigated at this size scale, but the study of active pumping solutions, such as EHD, has been limited. The first such studies were conducted by Pearson and Seyed-Yagoobi [84] in order to discover the behavior of EHD driven flow in microchannels under boiling and the reciprocal effect of the boiling on the EHD pump performance. An EHD micropump (adiabatic pump) was used to pump liquid within a two-phase loop that contains a microchannel evaporator, in which additional EHD electrodes (diabatic pump) were embedded and could be energized separately from the adiabatic pump. The single-phase performance of each pump as determined first before applying any heat transfer to the diabatic pump. For two-phase experiments, two cases were considered: in the first case, the electrodes in the evaporator were switched off so that the adiabatic pump was the only source of EHD pumping;

in the second case, the electrodes in the evaporator were activated to assist the adiabatic pump, these two cases are referred to as the "baseline" and "EHD enhanced" case, respectively. The two-phase experimental results are shown in Figure 22 and 23.

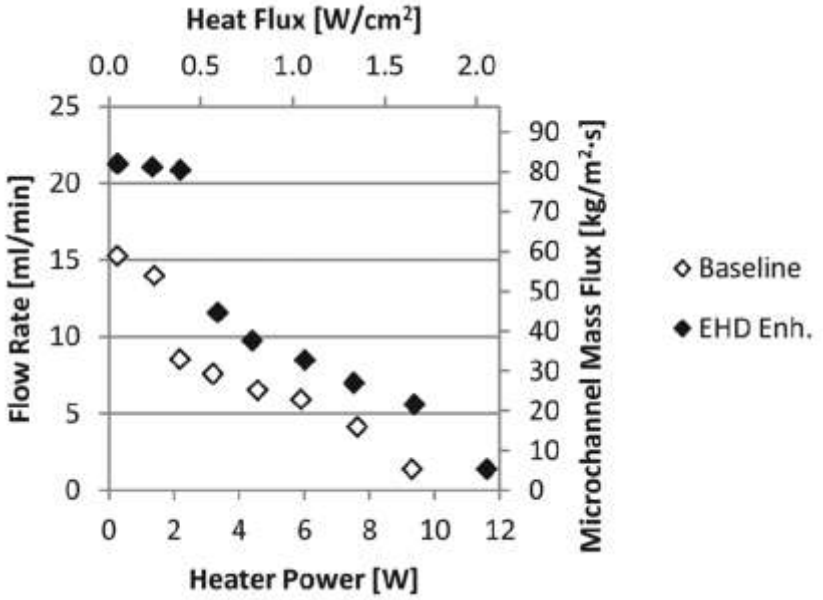

Figure 22: Effect of applied heat flux on the flow rate of the two-phase loop (750 V) [84]

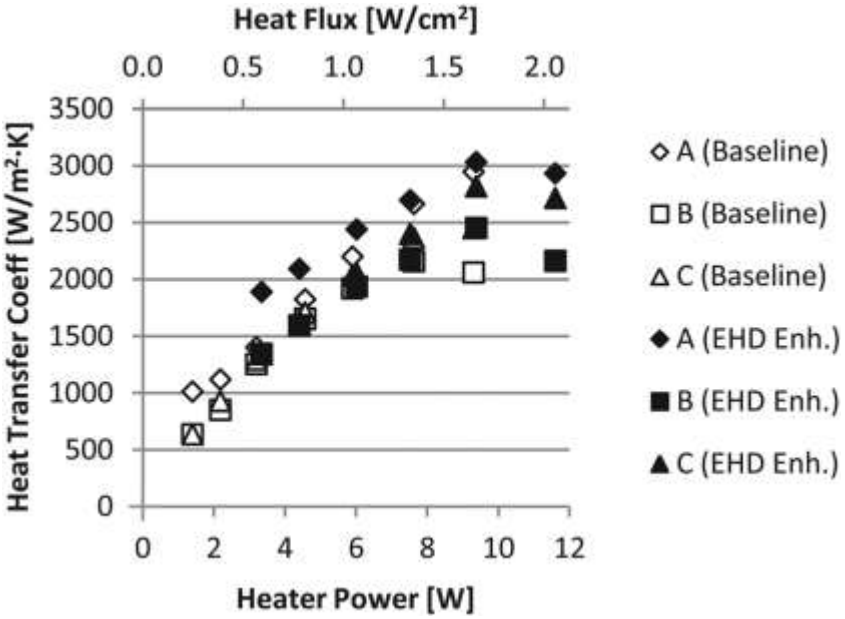

Figure 23: Measured local heat transfer coefficients at three thermistor locations in the evaporator (750 V): A: upstream edge, B: middle point and C: downstream edge [84]

As shown in Figure 22, the activation of electrodes in the evaporator section caused an increase in flow rate and there was a 40-45% drop in the flow rate at the onset of significant boiling whether or not the diabatic pump was active. The authors attributed this phenomenon to the pressure load due to evaporation, which imposed significant impedance on the flow at the onset of boiling. The activation of electrodes in the evaporator section was also shown, in Figure 19, to provide up to 30% enhancement to the heat transfer at low heat flux levels (below 1W/cm^2). At higher heat fluxes, the enhancement effect of EHD in the evaporator section was effectively eliminated. The author thus concluded that the sole use of electrodes in the evaporator without a separate pump was not successful except at very low heat flux levels below 0.2 W/cm^2 where evaporation of fluid was absent or negligible.

Patel and Seyed-Yagoobi [85], for the first time, presented the results of an experimental study of a unique microscale heat-transport device that is driven by electrohydrodynamic (EHD) conduction pumping in the presence and absence of gravity. The results from ground-based single-phase experiments were compared with those from experiments conducted on board a variable-gravity parabolic flight and are shown in Figure 24 and 25. For a single-phase liquid flow in a loop, it was expected that there should be no effect of the absence of gravity on the performance of the pump. However, from Figure 24 and 25, it was shown that, although the results were similar, there were some differences.

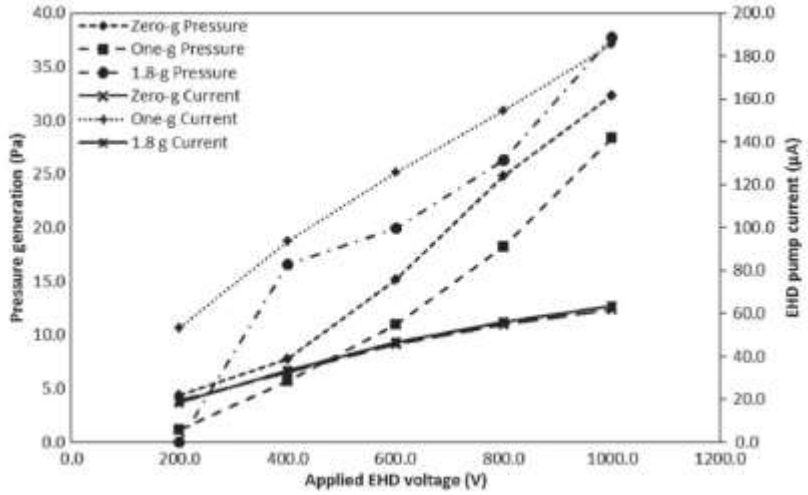

Figure 24: EHD pump pressure generation and current versus applied EHD voltage [85]

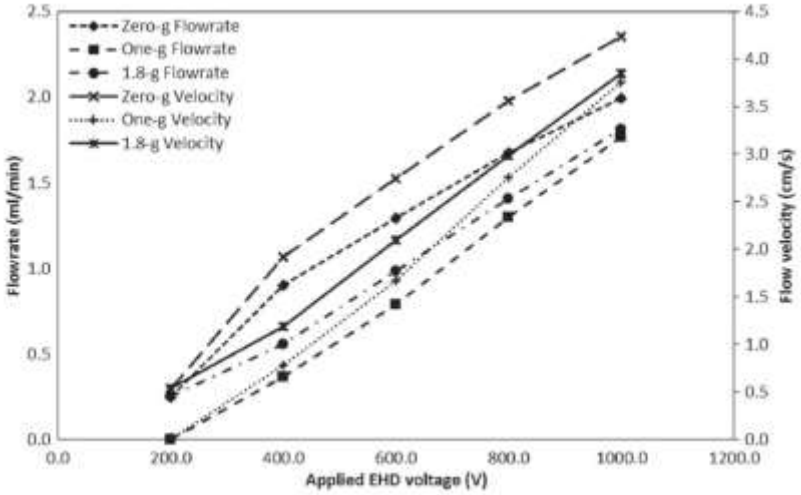

Figure 25: EHD pump flow rate and flow velocity versus applied EHD voltage [85]

The authors concluded that while there were differences in flow and pressure generation, preliminary single-phase data showed that the absence of gravity did not affect the performance of EHD pumps based on conduction mechanism. The use of EHD conduction pumping in both ground based and zero-gravity environments was confirmed.

Patel and Seyed-Yagoobi [86] then determined the flow and heat transfer characteristics of the aforementioned mesoscale two-phase flow heat transport device and local in-tube flow boiling heat transfer coefficient as a function of vapor quality in a mesoscale circular tube evaporator. In

addition, system recovery from evaporator dryout was achieved successfully for the first time in s mesoscale EHD-driven two-phase flow heat transport system. This study is also an extension of the work already done in macroscale by Bryan and Seyed-Yagoobi [78]. They demonstrated the scalability of the technique by scaling down in size to mesoscale.

The heat transfer coefficients in the mesoscale evaporator plotted as a function of vapor quality at three levels of mass flux are shown in Figure 26. The results show that for this low mass flux range, the internal flow convective boiling heat transfer coefficient decreases with quality and increases with mass flux. At higher vapor quality, the data for varying mass flux appear to converge. The experimental data also fall in between the predictions of two known micro and mesoscale flow boiling correlations. The authors concluded that the convective heat transfer coefficient achieved with EHD conduction pumping had a similar trend to other experiments at higher mass fluxes in the literature for mesoscale in-tube flow boiling.

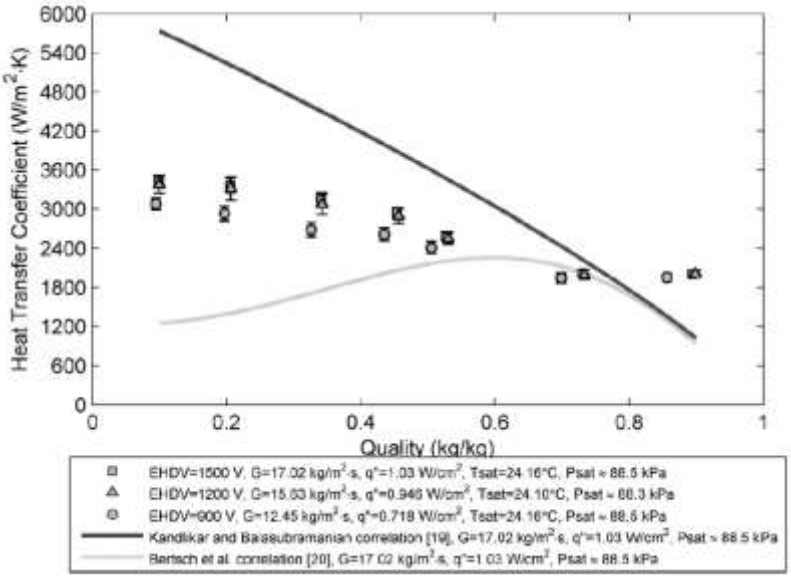

Figure 26: Flow boiling heat transfer coefficient of HCFC-123 versus quality for circular copper tube (D=1.5 mm), with comparison to two correlations [86]

In light of very few studies dedicated to operating microscale heat transport devices driven by electrohydrodynamic (EHD) conduction pumping for extended periods of time, Patel and Seyed-Yagoobi [87] extended the above work to long-term testing for eventual use in applications and to determine whether it is feasible to use a stand-alone EHD-driven heat transport system. Their experimental results demonstrated operation of a microscale EHD pump intermittently for 105 h over 15 days. Averages of each daily 7-h experiment are shown in Figure 27. The results indicated that the EHD conduction pump can successfully operate for a considerable amount of time without significant deterioration in pump performance. As with the flow rate measurements, the heat transport performance was very reliable over 15 days of operation despite the challenges presented by the highly dynamic nature of two-phase flow heat transport, and there was no degradation in performance at all, which means that the continuous application of the electrical field on the refrigerant HCFC-123 for over 105 h did not alter its heat transfer characteristics.

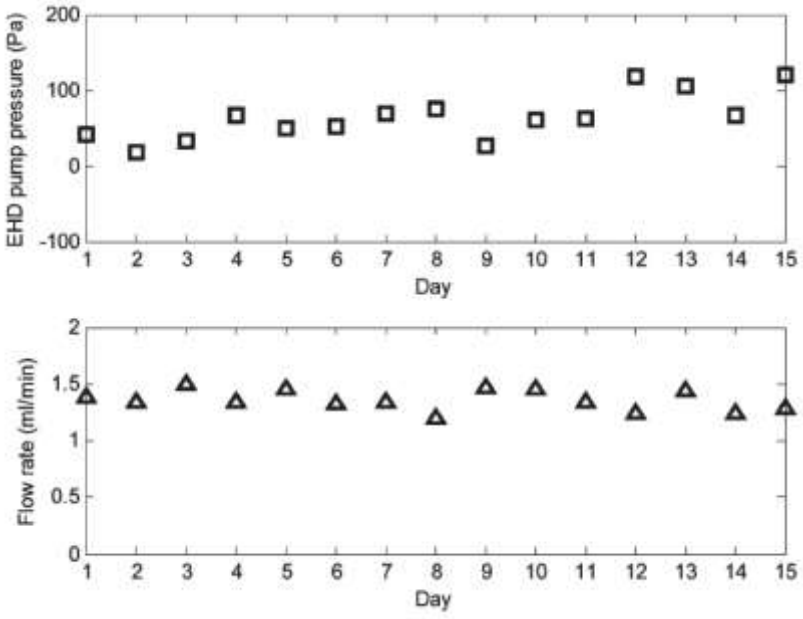

Figure 27: EHD pump pressure and flow rate averaged over 7 h/day for 15 days [87]

1.3.2 Liquid film flow generation and liquid film boiling enhancement with EHD conduction pumping

Siddiqui and Seyed-Yagoobi [88], for the first time, experimentally studied pumping of stratified liquid film in a channel with conduction phenomenon. They considered two innovative electrode pairs, capable of generating liquid film flow: Perforated electrodes and flushed electrodes. The experimental setup was a rectangular channel loop milled on a PVC piece. The loop consisted of two straight sections connected by two semicircles. The design and arrangement of the flush electrode pairs on PVC strip is shown in Figure 28.

Base on the liquid flow rate measurement for liquid film thicknesses of 2, 5 and 8 mm, they found that the liquid film average velocity increased with the applied voltage. However, with the liquid film thickness of 2 mm, the liquid film velocity slightly dropped with further increase in applied potential, which could be due to the ion-drag pumping effect taking place and forcing the liquid in opposite direction. For the flush electrodes design, the liquid film velocity was higher at film thickness of 5 mm compared to 2 mm and 8 mm film due to either the higher viscous shear stresses associated with thinner liquid films or the decrease in electric field intensity (thus, reduction in dissociated charge level) with thicker liquid film. They concluded that the flush electrodes were more suitable for thin liquid films, while perforated electrodes were better for thicker liquid films.

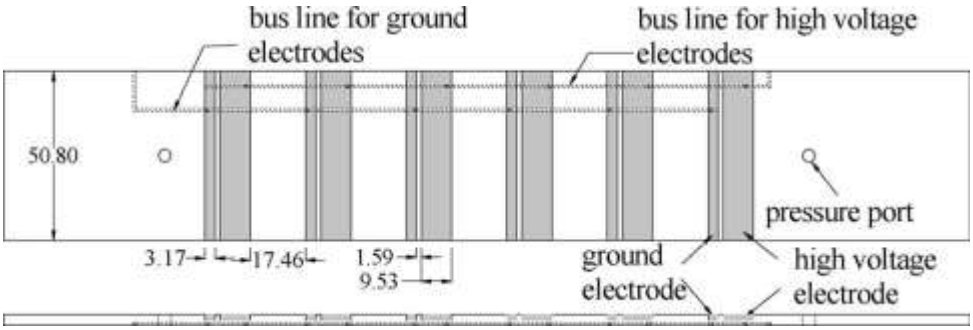

Figure 28: Top and side view of PVC strip with flush electrodes. Dimensions in millimeters [88]

Further studies by Nourdanesh and Esmaeilzadeh [89] compared the achievable heat transfer coefficients of a similar conduction pump using different film heights and different temperatures using kerosene. They presented the best operation condition by considering the effect of volume flow rate, heat transfer, power consumption ratio and conduction pumping efficiency of free surface liquid film in different film thicknesses and temperatures. They also compared the heat transfer coefficient on free surface liquid film passing on flush electrodes with similar liquid film in absence of flush electrodes in different temperatures. The schematic of their experimental setup is shown in Figure 29. The Loop consisted of two direct channels, Case1 and Case2, one involved flush electrodes and the other was for the measurement of fluid volume flowrate inside the loop and the comparison of heat transfer coefficient with electrode side.

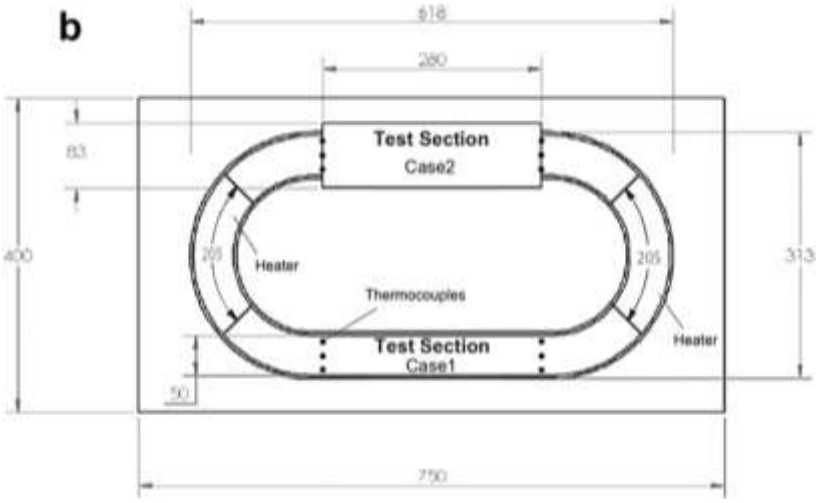

Figure 29: Schematic diagram of experimental setup (dimensions in mm) [89]

The variation of fluid volume flow rate versus applied voltage for different temperatures and film thicknesses is shown in Figure 30, showing that in all three of the thicknesses volume flow rate is increased with increasing the film temperature. The effect of increasing temperature on the enhancement of efficiency is considerable in low voltages. In addition, applied voltage related to the highest percentage of heat transfer coefficient enhancement demonstrated the reverse

relation with temperature. Results confirmed that there is a direct relationship between film thickness and the applied voltage related to the maximum heat transfer per pumps power consumption. Also the results show that, the optimum film thickness for heat transfer coefficient enhancement is 6 mm.

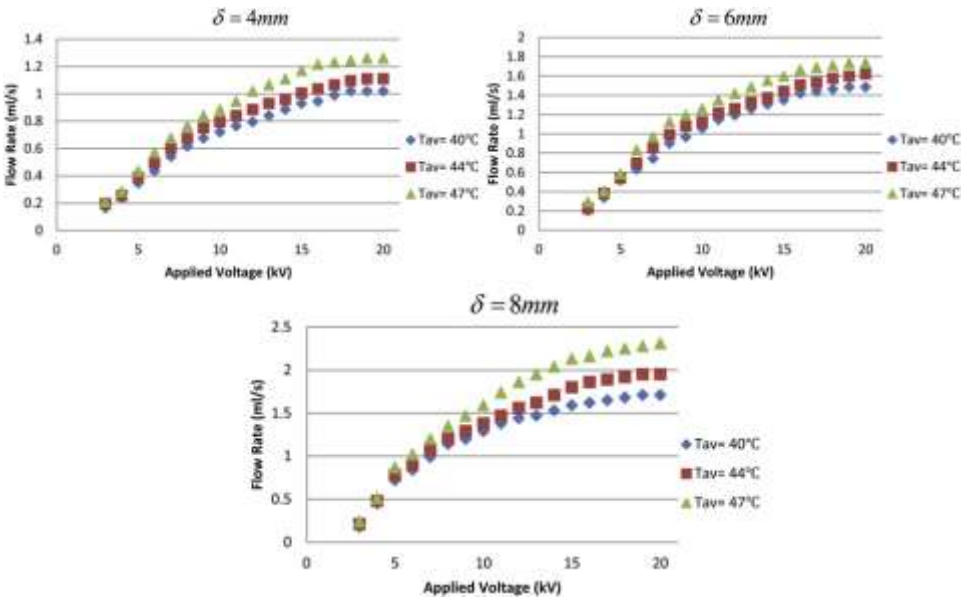

Figure 30: Fluid volume flow rate pumped in the channel versus applied voltage for different temperatures and film thicknesses [89]

Yazdani and Seyed-Yagoobi [90] then presented the theoretical formulation for EHD conduction pumping of liquid film and the corresponding numerical solutions in order to determine how liquid film flow is generated based on the electric conduction phenomenon and provide in-depth understanding of the interaction between electric fields and generated flow fields through dissociation/recombination phenomenon for a liquid film. Specifically, the role of controlling dimensionless parameters on the heterocharge layers and flow structures along with the impact of liquid film velocity on charge distribution are illustrated and fundamentally analyzed. The solution domain for numerical solution is illustrated in Figure 31.

The numerical results indicated that there was a net flow generated with its direction from the HV electrode toward the ground electrode. Their numerical results, shown in Figure 32, were also compared with experimental data of Siddiqui and Seyed-Yagoobi [88] to validate the numerical predications. Base on this comparison, they concluded that their numerical simulations successfully predicted the trends and the values of volumetric flow rate for various liquid film thicknesses and confirmed the nonmonotonic enhancement of flow characteristics with increasing the applied voltage.

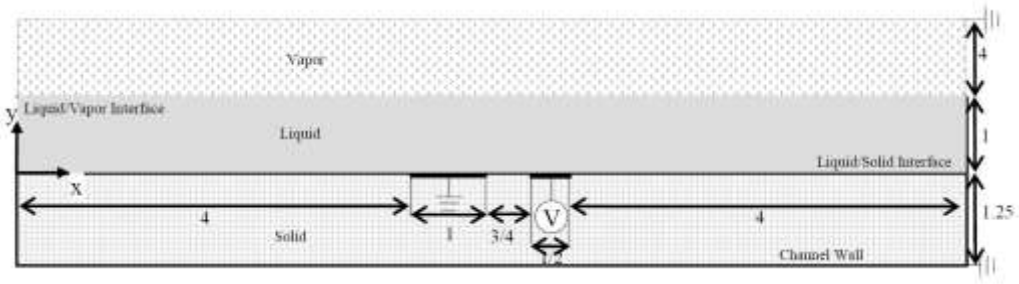

Figure 31: Schematic diagram of solution domain in dimensionless form. The length scale is liquid film thickness, d=4mm [90]

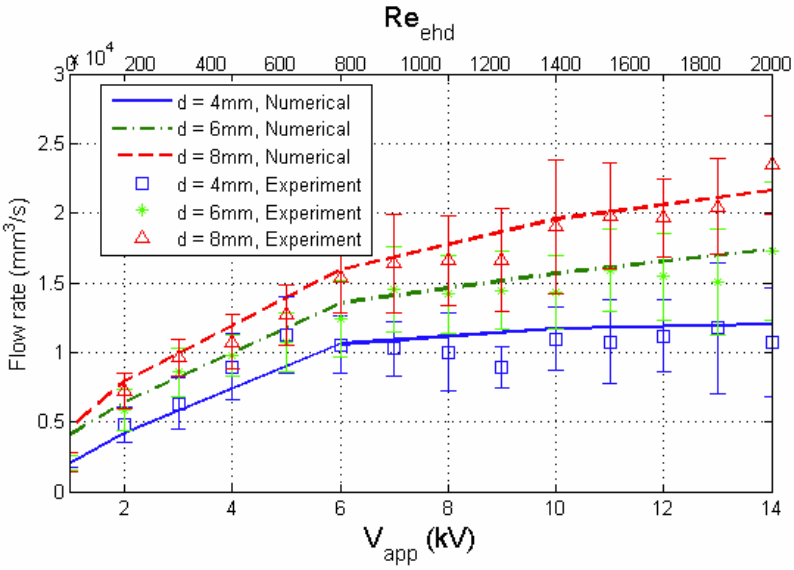

Figure 32: Numerical predictions and experimental data for average volumetric flow rate at the outlet [90]

Yazdani and Seyed-Yagoobi [91] extended the above work by fundamentally illustrating the electrically driven liquid film flow based on the conduction phenomenon in the presence of liquid film evaporation and the resultant heat transfer due to conduction pumping. The presence of liquid evaporation complicated the problem due to the changes in the liquid film thickness along the heated plate. The solution domain they used is shown in Figure 33. The flow system comprised a liquid film flowing over a two-dimensional flat plate. The channel was separated into four different sections: the entrance, electrode, evaporation, and downstream sections. The entrance, electrode, and downstream regions were adiabatic while a constant heat flux applied in the evaporation section.

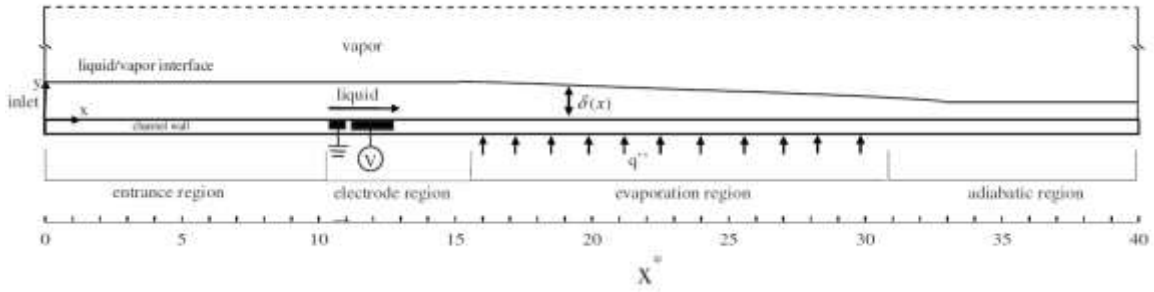

Figure 33: Schematic of 2D solution domain (not to scale) [91]

Their sectional heat transfer analysis for the EHD-conduction driven liquid film flow and comparison with that of the conventional pressure-driven flow are shown in Figure 34. The integration to obtain average Nusselt numbers was performed only in the evaporation section. They argued that while in early stages of evaporation, the pressure-driven flow showed better heat transfer performance compared with the EHD-conduction driven counterpart, the eventual increase of the Nusselt number in the downstream region was considerably higher for the EHD-driven flow resulting in better overall heat transfer performance for the latter case, as observed in Figure 34 (b).

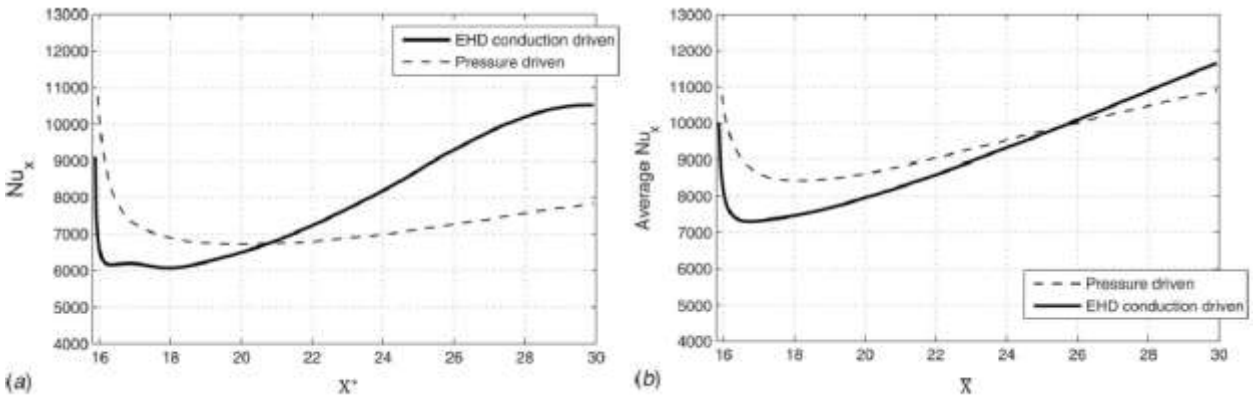

Figure 34: Comparison of local and average Nusselt numbers along the dimensionless channel length in the evaporation section [91]

Pearson and Seyed-Yagoobi [92] designed and fabricated two two-phase devices driven by the EHD conduction pumping phenomenon. The first one was a linear device that transports heat axially from a boiler at one end to a condenser at the other. The second device was circular, with a central boiler section and an annular condenser section surrounding it—heat is transported radially outward from the central heat source. The schematics of the linear and circular two-phase heat transport device are shown in Figure 35 and Figure 36 respectively. Both devices had a high heat flux source that evaporates a thin layer of liquid. Heat was dissipated through condensation to a heat sink and the EHD Electrodes were lithographically fabricated on the surface. The radial device incorporated a number of improvements compared to the linear device. Most notably, electrodes were included in the condenser section to reduce the pressure load of that section and the heat source was wetted with fresh liquid from all directions, thereby reducing the amount of distance that must be travelled by the working fluid.

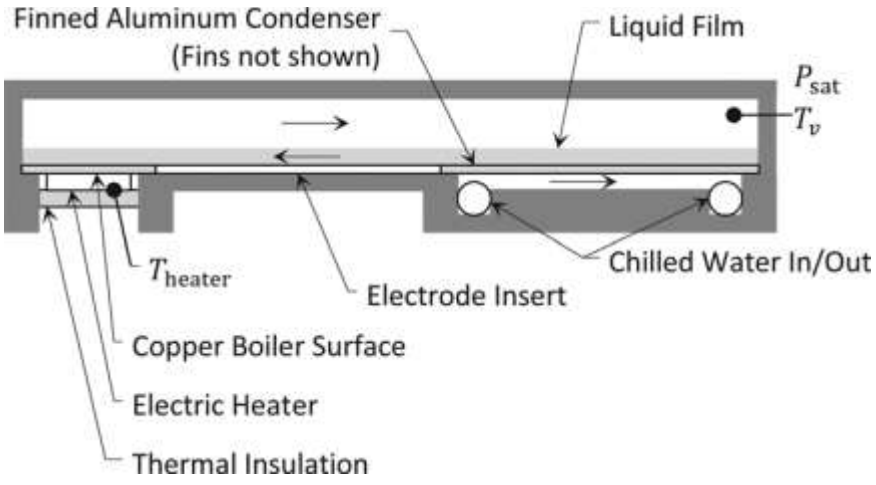

Figure 35: Schematic of linear heat transport device [92]

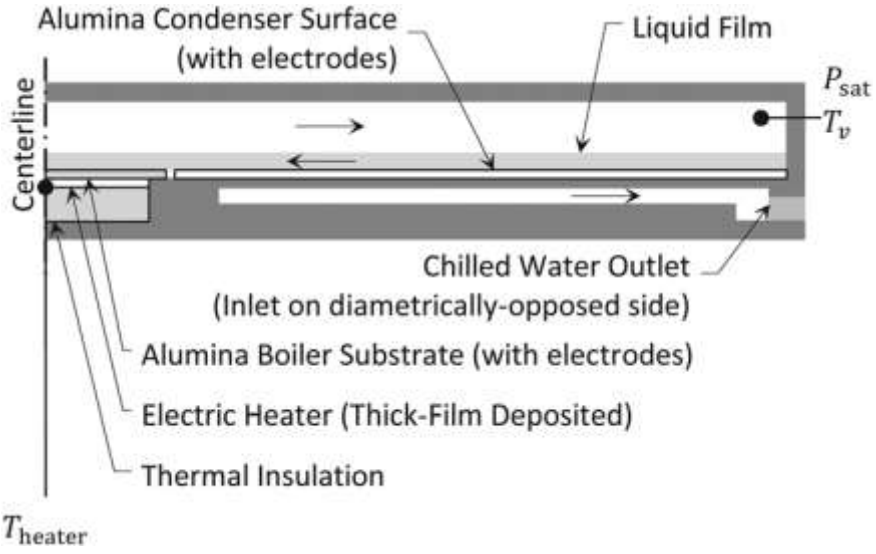

Figure 36: Schematic of radial heat transport device [92]

The heat transport performance of each device was experimentally characterized, the behavior with EHD-driven flow was compared to the case of an almost-stagnant liquid film where gravity was the only pumping force and are shown in Figure 37 and 38 for linear and radial heat transport devices, respectively. Without any EHD pumping, the liquid film flowed due to gravity, with the phase-change processes in the boiler and condenser causing a slight gradient in film thickness and a resulting gravity-driven flow to the boiler. Application of EHD supplied significant additional liquid to the boiler and caused notable reductions in the temperature of the boiler for a

given heat flux when compared to the no-EHD case. Their experimental results also showed that the use of EHD can provide significant increases in the maximum heat flux of the device when compared to the use of gravity alone. The power required to operate the EHD conduction pumps was a trivial amount relative to the heat that is transported.

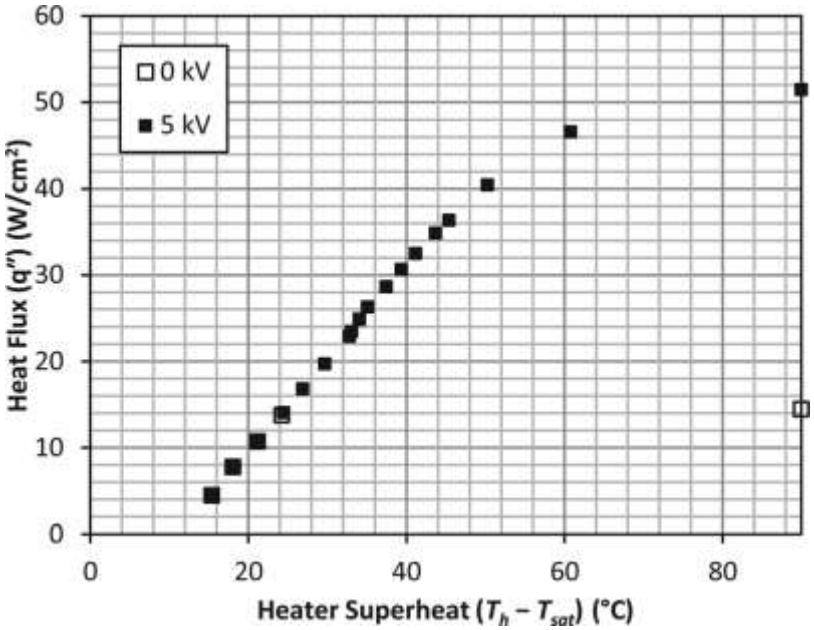

Figure 37: Boiling curve for the 2mm film in linear heat transport device [92]

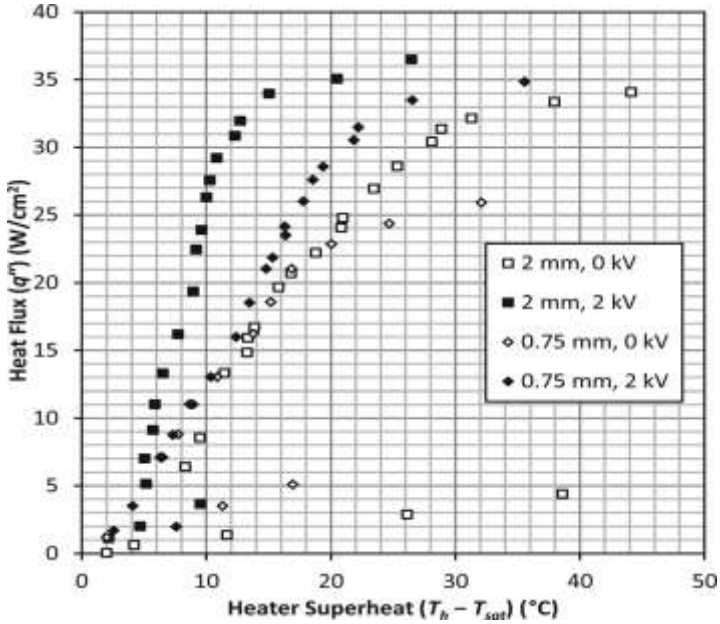

Figure 38: Boiling curves achieved with radial heat transport device [92]

Patel and Seyed-Yagoobi [93] continued the work carried out by Pearson and Seyed-Yagoobi [92] and investigated the electrowetting of the copper-plated nanofiber-enhanced surface via EHD conduction pumping mechanism for the entire liquid film flow boiling regime leading up to critical heat flux (CHF), and compared it to the bare surface without EHD-driven flow. The design and fabrication of the EHD conduction pump in this study was originally done by Pearson and Seyed-Yagoobi [92]. The major differences between them were electrode spacing and total number of electrodes. The liquid film flow boiling concept considered in this study is illustrated in Figure 39. It consists of a heater installed in the bottom center of a circular chamber. The heater is immersed in a film of liquid with a thickness of 2.0 mm.

Their experimental results are shown in figure 40. At low heat flux, activation of the EHD pump delayed the ONB. Thus, there was an initial adverse effect of EHD on heater surface temperature in the combined EHD/enhanced surface experiment. However, beyond the isolated bubble regime, the two techniques worked exceedingly well together and resulted in a maximum of 555% enhancement in boiling heat transfer coefficient compared to the bare surface experiment without EHD conduction pumping. They argued that the increase in overall surface area and nucleation site density due to the presence of the nanostructures allowed for a shift in the ONB, which changed the overall trajectory of the boiling curve compared to the bare surface. This improved performance was also a result of increased pressure generation within the liquid film due to EHD.

In addition to the research presented in this paper, they also studied the liquid film flow boiling driven by the EHD conduction in microgravity, on board a variable gravity parabolic flight [94]. However, the parabolic flight experiments were limited due to time constraints of the flight

and microgravity results reported were transient as opposed to steady-state results in terrestrial experiments.

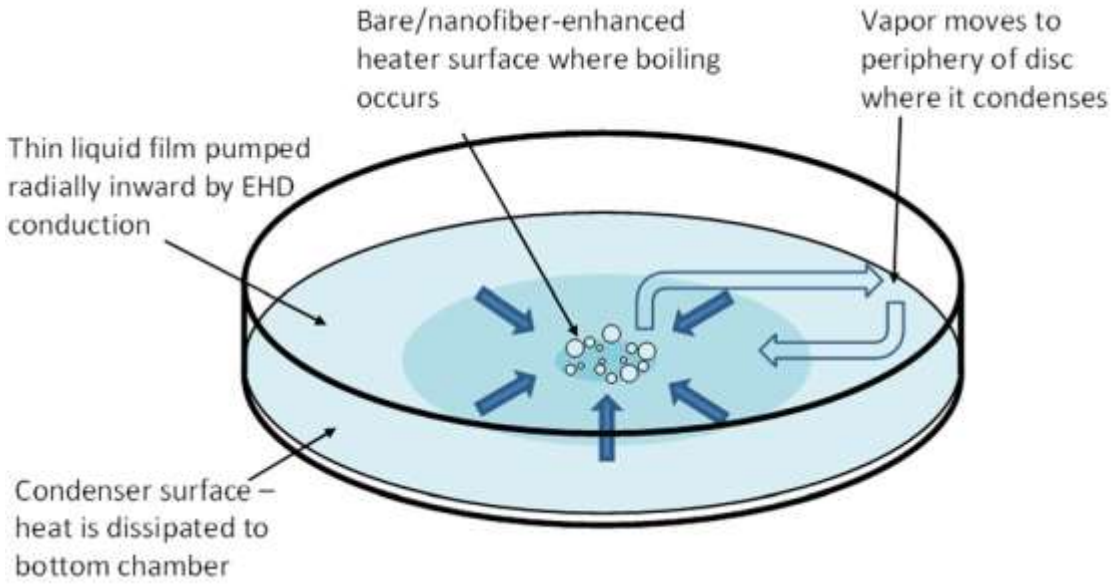

Figure 39: EHD-driven liquid film flow boiling concept [93]

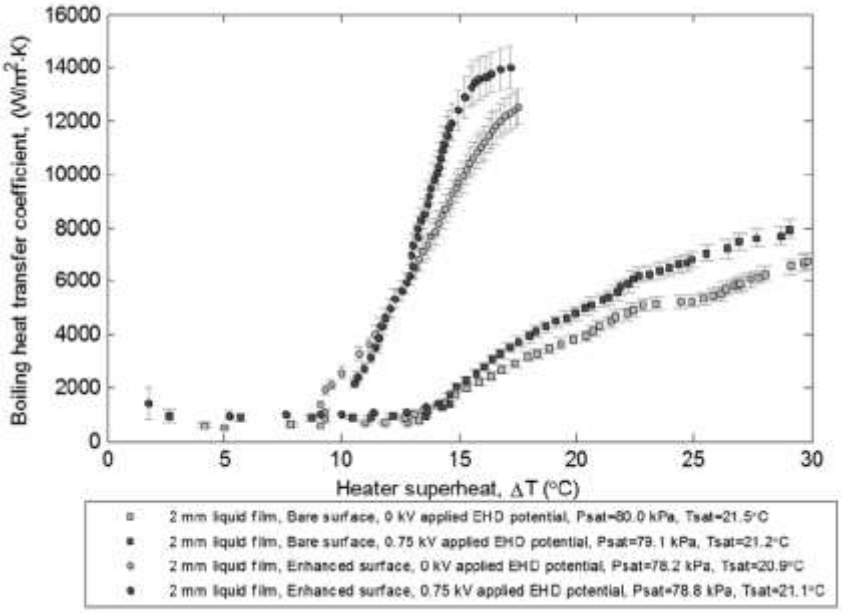

Figure 40: Boiling heat transfer coefficient for bare and enhanced surfaces with and without EHD conduction pumping [93]

1.3.3 Other EHD conduction pumping applications

Haonaoka et al. [95] investigated liquid-jet phenomenon induced by electrohydrodynamic (EHD) pumping isothermal dielectric liquids without direct charge injection at a metal/liquid interface using a pseudo-doughnut to plane electrode system and four different dielectric liquids: which are referred to as DBDN, BCRA, Tr-Oil, and FS-Oil. In addition, two special nozzles, referred to as a normal nozzle and spiral nozzle, were designed in order to obtain high directionality of the liquid jet.

They reported that a highly directed liquid jet was created by applying either a positive or a negative voltage to the pseudo-doughnut electrode and attributed generation mechanism of these to pure conduction pumping. More coherent and directed liquid jets were obtained by using a special nozzle and it was found that the flow pattern takes on a spiral structure. This structure was thought to be due to the synergistic effect of the conical hole shape and the Coanda effect. The maximum velocity and pumping pressure. The achieved were 1.5 m/s and 5.5 k Pa, respectively, at an applied voltage of 23 kV with an approximately 2.5 W of electrical power consumption in BCRA.

Haonaoka et al. [96] further designed and examined an EHD pump with up to nine pairs of the rod-to-rod and meshy parallel plates electrode assemblies arranged in series to develop a compact pump which was possible to generate the high pressure head. They observed vigorous liquid flow ejecting from the pump outlet and found that the flow direction was always from the cathode toward the anode. They also observed potential distributions between the electrodes which is an indication of ionic space charges gathering in the vicinity of the electrodes. By gathering ions, the electric field was reinforced at the inside of heterocharge layers and was dropped at the

outside zone of layers due to a space charge effect. The reinforcement of electric field particularly was remarkable at around the anode.

They concluded that the generated pressure increased with nearly the square of the applied voltage. The pressure and current also increased nearly in proportion to the number of electrode pairs. The maximum pressure head achieved with a series of nine electrode pairs was 25.3 k Pa at 18 kV with maximum power consumption of 7.2 W. The measured flow rate exhibited a linear dependence on the applied voltage. The flow rate also increased with increasing the number of electrode pairs, but the rate of increase reduced with the number of electrode pairs because of loss coefficients on the flow.

Feng and Seyed-Yagoobi [97] were the first researchers who studied the capability of EHD conduction pumping as an active way of controlling liquid phase flow distribution in a two parallel branch loop. Their study showed both the flow redirection and maldistribution recovery capabilities of EHD pumping at the macro-scale. The concept is illustrated in Figure 41.

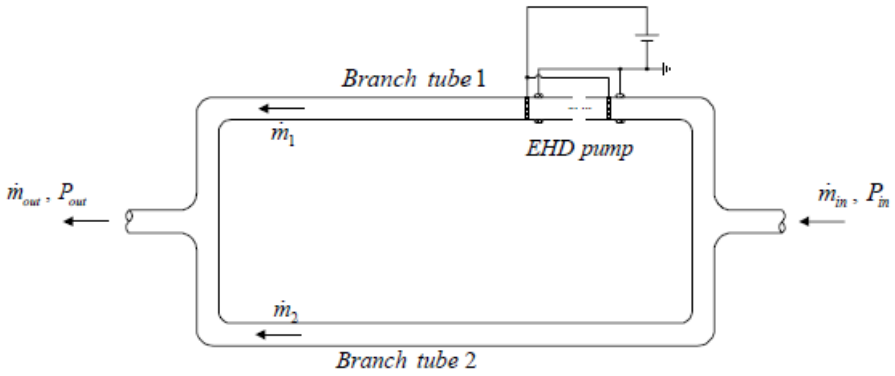

Figure 41: Illustration of flow distribution between two branch tubes with an EHD conduction pump installed [97]

Figure 42 shows the flow distribution control at a total mass flux, G_{total} = 100 kg/m^{2}s. Initially, the liquid flow was evenly distributed in two branch lines. At an applied voltage of 15

kV, the generated pressure head of the EHD conduction pump was so high that the liquid flow in the manifold was completely directed to one branch line and no liquid flow passed though the other branch line. Such phenomenon also took place for the flow distribution at an applied voltage of 10 kV and G_{total} = 50 kg/m^{2}s. They also evaluated two important criteria: the power consumption and response time of EHD conduction pumping mechanism, which are critical for evaluating the usability of this technology in actual thermal control systems. They found that, at the applied voltages ranging from 10 kV to 15 kV and the mass fluxes ranging from 100 kg/m^{2}s to 200 kg/m^{2}s, the electrical power consumptions were around 1 W, which is negligible compared with heat transfer rates (of magnitude of kW) for HVAC&R heat exchangers. The response time, calculated with equation 30 is on the order of the charge relaxation time of the working fluid, in milliseconds, and therefore sufficiently short for use in actual applications.

$$\frac{\varepsilon}{\sigma_e} \leq \tau_{res} \leq 2\frac{\varepsilon}{\sigma_e} \tag{30}$$

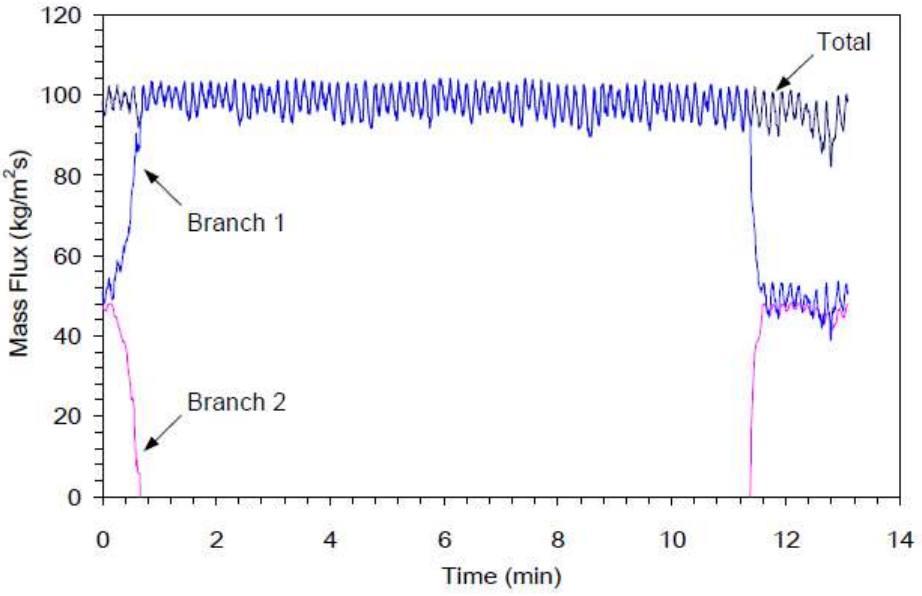

Figure 42: Liquid flow distribution at G_{total} =100 kg/m^{2}s and applied voltage of 15 kV [97]

Feng and Seyed-Yagoobi [98] then applied EHD conduction pumping to a two phase flow distribution system in macro-scale. They investigated EHD conduction pump for active thermal

control of the parallel heat exchanger, instead of the existing passive solutions, in a convective experimental apparatus with HCFC-123 as the working fluid. Their experimental work showed successful control of dielectric liquid/vapor flow distribution between two parallel branch lines utilizing an EHD conduction pump up to a certain mass flux level and vapor quality level under adiabatic condition. Experiments conducted at G_{total} =50 kg/m^{2}s were carried out at three vapor quality levels (6%, 20%, and 26%). Four high DC voltages, 15, 17, 18, and 20 kV, were applied to the EHD conduction pump to generate pressure heads.

Figure 43 shows the pressure drops along the branch tubes and the EHD conduction pump. At G_{total} =50 kg/m^{2}s, the EHD conduction pumping phenomenon became strong enough to alter the two-phase flow distribution. Steps of pressure drop along branch tubes were observable, when the applied voltage increased gradually. The maximum pressure gain along the EHD conduction pump reached up to approximately 1400 Pa at an applied voltage of 20 kV and a vapor quality of 6%. It is also interesting to see that the pressure drops along EHD pump became negative with the applied voltages (e.g. 15, 17, 18, and 20 kV). Such pressure measurements verified the generation of dominating EHD pressure head capable of overcoming the frictional force of flow inside the pump. When the quality increased, the pressure head generated by the EHD conduction pump decreased and its control capability of two-phase flow distribution also decreased.

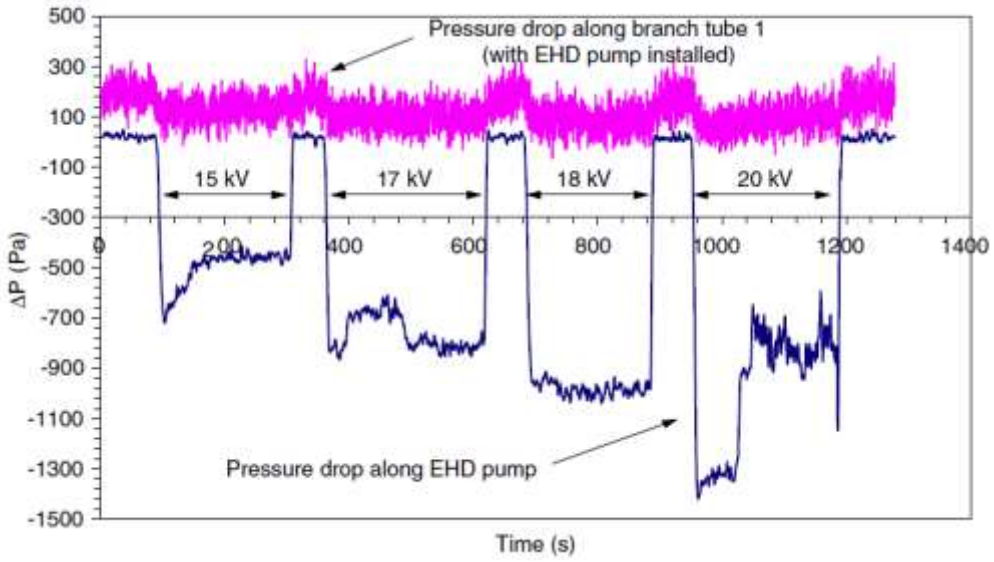

Figure 43: Pressure drop along EHD conduction pump and branch tube at G_{total} =50 kg/m^{2}s and a vapor quality of 6% [98]

They also argued that the large void fractions, defined as the vapor-flow cross-sectional area to the total cross sectional area of the tube of two-phase flow, was a challenge imposed on the EHD conduction pump. As an example, with the vapor qualities of 6% and 26%, the corresponding void fractions are 95% and 99%, respectively. Such high void fractions indicate that even with the vapor quality of 6%, the liquid phase occupies only a very small portion of tube cross-sectional area. However, EHD conduction pump can only influence the liquid phase portion of the two-phase flow and there is room for designing more effective electrodes by considering the associated void fractions.

In the above mentioned studies, the EHD conduction pumping was operated in the same direction as the mechanically generated main flow stream. Sinnamon [99] was the first researcher who demonstrated the successful control of flow distribution between two parallel lines using the EHD pump in two configurations: the first configuration oriented the EHD pump such that the net pumping forces acted in the same direction as the flow velocity and the second configuration

oriented the EHD pump such that the net pumping forces acted in the direction opposite to the flow velocity. For the second configuration, increasing the main flow velocity enhanced pressure generation rather than suppressing it, contrary to the first configuration. Based on the comparison of results from the two flow distribution tests, he concluded that the second configuration was more effective than the first configuration for increasing flow in one line.

1.4 Objectives of current study

The first objective of the proposed work is to provide a fundamental understanding of impacts of electrodydrodynamic (EHD) conduction pumping on two electrically driven heat transport systems: flow distribution control used in thermal management systems for microelectronics, and liquid mixing and thermal homogenization in a spherical reservoir simulating the fuel tank used in space station. The second objective is to investigate the enhancement of pool boiling via surface enhancement of various types such as nanofiber mats. Moreover, this study investigates the convective flow condensation of water vapor inder sub-atmospheric pressure.

Chapter 2 presents the first experimental study of liquid-phase and two-phase flow distribution control with EHD conduction pumping in meso-scale. A reverse EHD conduction pumping mode is also considered. Both configurations are examined in two scenarios: the redistribution of initially equal flow in two branches and the correction of an initially maldistributed flow in two branches. Experimental results confirm that the reverse pumping direction configuration of EHD pump is more effective than the same pumping direction configuration. The comparison of experimental results is provided for the fundamental understanding of the effect of upstream flow velocity on the formation of heterocharge layer and EHD conduction pumping mechanism.

In Chapter 3, a spherical reservoir with embedded EHD conduction pump, utilized for liquid mixing and thermal homogenization in a spherical enclosure, is experimentally studied. Temperatures at various locations are measured for the characterization of the proposed thermal homogenization process due to the EHD conduction pumping. In addition, a numerical analysis of a simplified model of the experimental setup is conducted, the electric field, net charge distribution, Coulomb force density, and the resultant velocity field at the steady-state condition as well as the numerically determined temperature distribution of the working fluid are provided to illustrate fluid mixing and thermal homogenization process. This study provides valuable information on the characterization of liquid mixing and thermal homogenization via EHD conduction pumping.

Chapter 4 provides a fundamental understanding of surface roughness and orientation effect on pool boiling. Several commonly used empirical correlations are examined for this purpose. In addition, pool boiling heat transfer enhancement, with nanofiber mat made of alumina ceramic substrate covered by electrospun nanofiber and several specifically machined surfaces, is characterized in terms of heat transfer coefficient and critical heat flux (CHF) and compared with bare surface data.

In Chapter 5, the in-tube convective condensation of distilled water in mini-channel under sub-atmospheric pressure is experimentally studied. The primary motivation and uniqueness of this study is providing fundamental understanding of convective flow condensation process of water vapor under sub-atmospheric pressure. It is also the first step in developing the condenser in the vapor compression cycle of refrigeration systems, which has a zero global warming potential, using water as working fluid,.

CHAPTER 2 EXPERIMENTAL STUDY OF LIQUID-PHASE AND TWO-PHASE FLOW DISTRIBUTION CONTROL IN MESO-SCALE WITH DIRECTIONALLY THE SAME AND REVERSE ELECTROHYDRODYNAMIC CONDUCTION PUMPING

2.1 Introduction

Efficient pumping and control of working fluid is a critical requirement for heat transport devices, especially for meso- and micro-scale cooling systems used in various applications, such as the cooling of aerospace components, microelectronics and power electronics. Thermal control solutions for these applications are expected to have features such as real-time recovery from dryout conditions, smart redirection of flow from areas of low need to areas of high need, and simultaneous autonomous management of multiple heat generating components [99]. Due to the advances in microelectronics, miniaturization of such thermal control solutions is also expected to handle heat loads in small scales, while incorporating desired characteristics such as low power consumption, low cost, and rapid and smart redistribution of flow to localized hot spots. EHD conduction pumping can be applied to enhance and control mass and heat transfer of both isothermal and non-isothermal liquids as well as two-phase fluids and shows its potential as an active control technique of flow distribution for multi-scale systems in both terrestrial and microgravity environment. It is believed to be a suitable method to address the above challenges [100].

Flow distribution control via EHD conduction pumping has been previously investigated only in macro-scale. The current study aims to expand the knowledge and understanding of EHD driven flow distribution control by experimentally examining its capability in controlling both isothermal liquid and two-phase flow distribution in meso-scale and facilitating the recovery from dry out condition in two-phase system. The corresponding Reynolds number range in this study

was 0-817. Consider a meso-scale flow distribution system with equal flow distribution between two branches shown in Figure 44, one of the objectives of the experimental study is to install a meso-scale EHD conduction pump in one branch (refer to Figure 45) and regulate the flow distribution via the activation of the EHD pump. The EHD conduction pumps used in this study were previously designed and investigated by Patel and Seyed-Yagoobi [85] and their performance is well documented and understood. For two-phase flow in meso-scale, gravity plays a less important role, heat transfer and pressure drop characteristics are remarkably different than those in macro-scale. This study gave new insights into the distribution of two-phase flows in smaller scales than previously examined. An understanding of the two-phase flow instability, typically occurs in meso- and micro-scale, and the associated back-flow phenomenon observed is also provided.

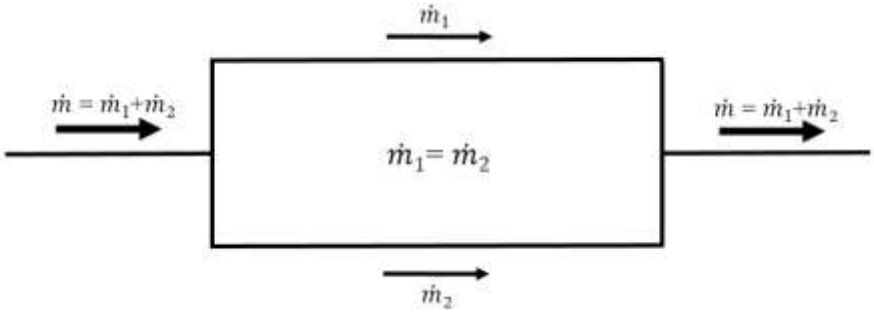

Figure 44: Equal flow distribution

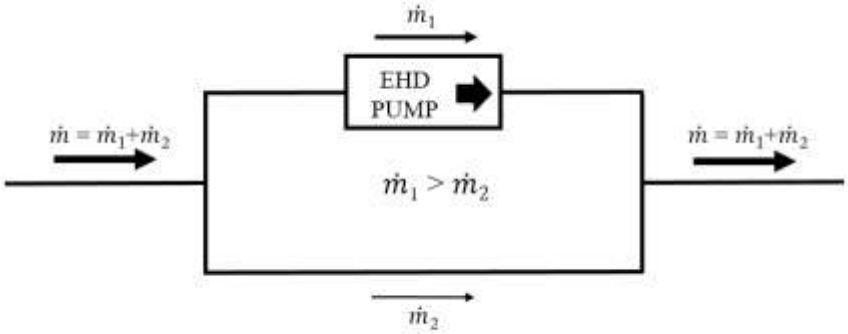

Figure 45: Flow distribution control with EHD conduction pumping

In addition, the performance of EHD conduction pumping operating in the opposing direction (Figure 46) was experimentally characterized. Two different scenarios are considered: the redistribution of initially equal flow in two branches and the correction of an initially maldistributed flow in two branches. Its capability of actively controlling the flow distribution is examined in terms of the value of applied potential for initiation of flow divergence or flow equalization, the complete suppression of flow in the active branch, and the flow rate difference between the two branch lines when the applied potential is at its maximum allowed value. The comparison of experimental results with those achieved with the same EHD pumping direction configuration is also provided in order to investigate the effect of upstream flow velocity on the formation of heterocharge layer and EHD conduction pumping mechanism. A qualitative explanation for the better performance of EHD conduction pumping in the reverse mode is also given.

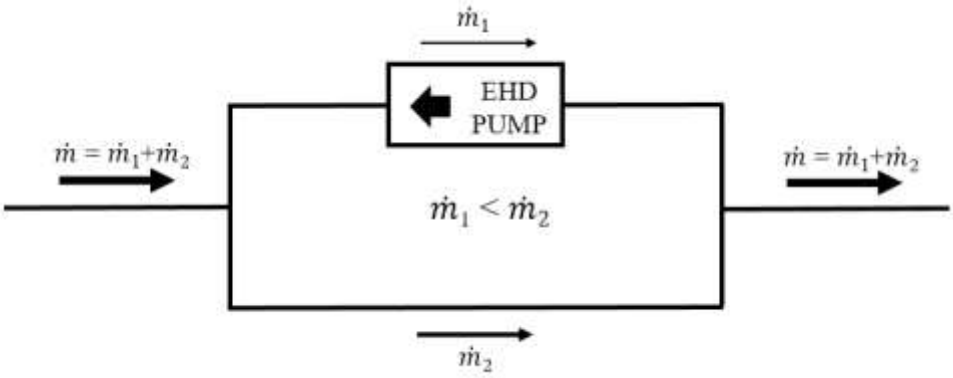

Figure 46: Flow distribution control with directionally reverse EHD conduction pumping

2.2 Experimental setup and procedure

2.2.1 Experimental setup 1 and 2

Experimental setup 1 is designed and assembled for EHD conduction pump driven single-phase liquid flow distribution control experiment and has three branch lines. Experimental setup

2 was modified from Experimental setup 1 by removing the middle branch and installing an evaporator in each remaining branch and a condenser behind them and was used for two-phase and directionally reversed EHD pumping mode experiments. The schematics of both experimental setups are shown in Figure 47.

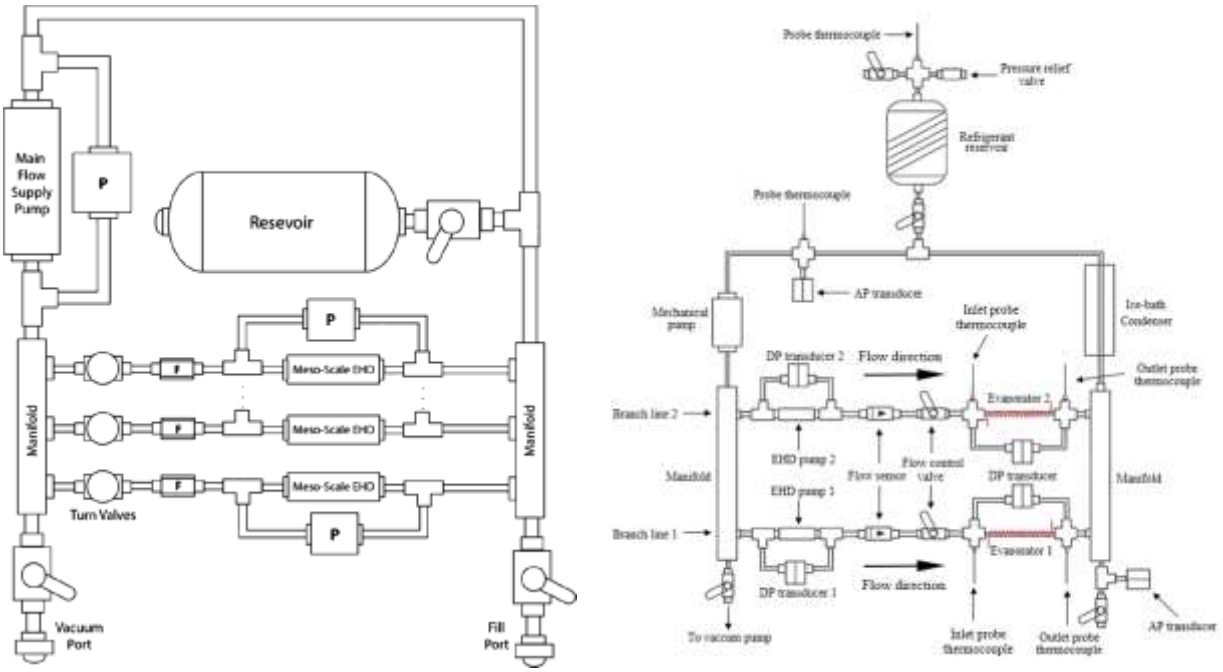

Figure 47: Schematics of experimental setup 1 (left) and 2 (right)

Their working principle will be explained with experimental setup 2 due to its structural complexity compared to 1 and their similarity. A Cole Parmer Model 75211-10 mechanical pump was utilized to generate the initial flow in the two parallel branches that diverged out of a manifold. Each branch contained an identical EHD conduction pump (refer to Figure 48 for its detailed design) followed by a Sensirion SLQ-HC60 liquid flow sensor which measured the flow rate of the liquid before the evaporator in each branch. The fact that identical EHD pumps were utilized allowed for the branches to be similar in dimensions. As the electrodes in both EHD pumps were flush with the tube wall, the directionality does not affect the dynamic flow resistance. Both pumps were connected to the same high voltage power supply with a specifically-made switching board,

which guaranteed that each pump could be disconnected from the power supply independently and that the same applied voltage would be received if both pumps were activated. The pressure generation of each EHD conduction pump was measured with a Validyne DP15 differential pressure transducer (DP transducer). The Precise needle valve after the flow sensor on each branch allowed for control of flowrate in each branch and therefore the initial flow distribution.

Identical copper evaporator tube (71 mm in length) was installed in each branch, after which another manifold was installed for the flow convergence. The copper evaporator tube has an inner diameter of 1.5 mm and an outer diameter of 2.5 mm, the thermal conductivity of the copper was 401 W/m·K. Uniform heat fluxes applied to the copper evaporator tube were guaranteed with an even wrapping of low-resistance 32 AWG Nichrome resistance heater wire, which had a thin layer of Polyimide electrical insulation. Five T-type thermocouples were attached to the out surface temperature of the evaporator. The voltage to the heater wire was accurately controlled with a programmable power supply. The evaporator was thermally well insulated to prevent heat loss to the surroundings, which was confirmed by the outer surface temperature measurement of the insulation layer using a wire T-type thermocouple. Two T-Type probe thermocouples were used to measure the bulk fluid temperature at the inlet and outlet of each evaporator. A condenser, made of a copper tube in an open box, was installed after the second manifold. The liquid exiting the condenser flowed back to reservoir and the mechanical pump, completing the loop. A pressure relief valve installed on the reservoir was set to open at approximately 150 kPa of absolute pressure.

The working fluid used in experimental setup 1 and 2 was 3M™ Novec™ 7600 Engineering Fluid and refrigerant HCFC-123 and their properties are given in Table II and Table III, respectively.

Table II: Properties of 3M™ Novec™ 7600 Engineered Fluid [101]

Physical Properties	3M™Novec™7600
Liquid Density	1540 kg/m^3
Liquid Dynamic Viscosity	164.8×10^{-11} Pa·s
Volume Resistivity	3×10^{10} ohm·cm
Dielectric Constant	6.4
Dielectric Strength, 2.54 mm gap	31 kV

Table III: Fluid properties of refrigerant HCFC-123 at 25°C and 1 atm [102-104]

Physical Properties	HCFC-123
Chemical Name	2,2-dichloro-1,1,1-trifluoroethan
Chemical Formula	CF_3-$CHCl_2$
Boiling Point	27.85 °C
Heat of Vaporization at Boiling Point	170 kJ/kg
Liquid Density	1463 kg/m^3
Saturated Vapor Density at Boiling Point	6.47 kg/m^3
Liquid Thermal Conductivity	0.08 W/m·K
Saturated Vapor Thermal Conductivity at Boiling Point	0.0112W/m·K
Liquid Viscosity	0.456 mPa·s
Saturated Vapor Viscosity at Boiling Point	0.011 mPa·s
Liquid Electrical Conductivity [104]	4.7×10-11 S/m
Liquid Electrical Permittivity [104]	42.43×10-12 F/m

National Instruments PCI 6024E, USB-6009, USB-6211 and USB-9219 data acquisition systems were used to acquire experimental data along with an NI LabVIEW Virtual Instrument software program. The differential pressure transducers had a range of 0-2200 Pa with an accuracy of ±0.25% of the full scale range, and the absolute pressure transducer had a range of 0-140 kPa with the same accuracy as the DP transducers. The flow sensors had a range of 0-80 ml/min with an accuracy of ±10% of the measured value and a repeatability of ±1.5% of the measured value.

The high voltage power supply was used in the range of 0-1.5 kV with an accuracy of ±1% of the full scale range plus ±1% of the voltage setting and a repeatability of ±0.1% of the full scale range. The current was in the range 0-100 μA with accuracy and repeatability in the same percentage values as the voltage. The power supply for the resistance heater wire on the evaporator had a range of 0-120 VDC and an accuracy of ±0.05% of the full scale range, with a 5 mV ripple.

The electrical power generated by the heater wire on the evaporator was calculated from the applied voltage and known resistance. The heater power divided by the evaporator tube inner surface area was used as the applied heat fluxes to the working fluid for two-phase flow experiment. The required energy for full phase change was determined from the real-time measurement of the mass flow rate, and the latent heat of vaporization of HCFC-123, h_{fg} from the thermodynamic tables in [102]. The vapor quality *x*, at the exit of the evaporator, was found based on the energy balance and is given below.

$$x = \frac{q}{\dot{m}h_{lv}} \tag{31}$$

The systematic errors associated with all measurement devices are given in Table IV, along with an uncertainty analysis for derived quantities.

Table IV: Maximum systematic error of various measurement devices and experimental uncertainty for chapter 2

Measurement	Maximum systematic error
Temperature	±0.5°C
Differential Pressure	±5 Pa
Absolute Pressure	±350 Pa
Flow Rate*	±0.2 mL/min
Voltage of HV Power Supply	±30 V
Current of HV Power Supply	±2 µA
Voltage of Evaporator Power Supply	±0.06 V
Derived quantity	**Maximum Uncertainty**
Evaporator Heater Power, Q	±0.7%
Evaporator Heat Flux, q''	±0.7%
Vapor Quality, x	±10.02%

* Unlike other quantities, flow rate error is based on maximum measured value during the experiment and not the full scale range of the device.

2.2.2 Electrode design of EHD conduction pump

The electrode design of EHD conduction pump used for all flow distribution experiments were the same as the ones used in previous studies of Patel et al. [85], and they were fabricated from stainless steel discs with a central hole of 1 mm diameter. The high voltage electrodes were made to be thicker than the ground electrodes. The exact thicknesses and thickness-ratios of these electrodes and spacers were designed based on numerical simulations of EHD conduction pumping [90], such that an asymmetric electric field would form between the electrodes, resulting in an optimal net electric force to generate favorable fluid flow.

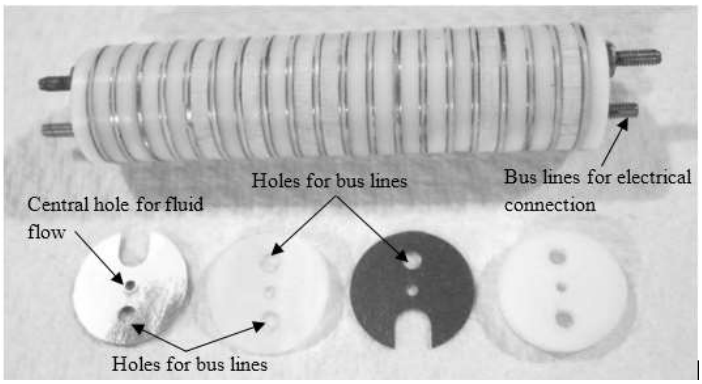

Figure 48: Assembled EHD conduction pump with 20 electrode pairs and individual electrodes and spacers [85]

The pumps were built with 20 pairs of electrodes, each with PTFE Teflon spacers in between, as shown in the top of Figure 48. At the bottom of Figure 48, from left to right, are the thin ground electrode, the thin inter-electrode spacer, the thick high voltage electrode, and the thick spacer used between electrode pairs. The electrode and spacer dimensions are given in Table V.

Table V: EHD conduction pump electrodes and spacers dimensions [85]

Component	Thickness
Narrow electrode	0.127 mm
Narrow spacer	0.127 mm
Wide electrode	0.381 mm
Wide spacer	1.588 mm

The pump performance curve of the EHD conduction pump used in the third branch of the experimental setup 1 (Figure 47) is shown in Figure 49 as an example. The pressure generation of the EHD conduction pump reached a maximum in the static case, in which the pump was isolated from the loop via valves and the flow rate was zero. In this case, steady state heterocharge layers formed in the vicinity of the electrodes at a maximal thickness for the pump design, since the layers were not disturbed by any net flow. When the EHD conduction pump was reconnected to the loop by opening the valves, the fluid inside the pump was driven by net electric force, and the resulting

convection lead to the shrinking of the heterocharge layers and therefore lower pressure generation. In addition, the pressure drop due to the flow resistance of the EHD pump section increased with flow rate. The combination of these two effects resulted in a decrease in the net pressure generation of the EHD conduction pump. Figure 49 also clearly shows that the EHD conduction pump performance improved with higher applied voltages. For the static pressure generation case, Figure 50 shows the current in micro-amp and power consumption in Watts for the same EHD conduction pump as well for the static case.

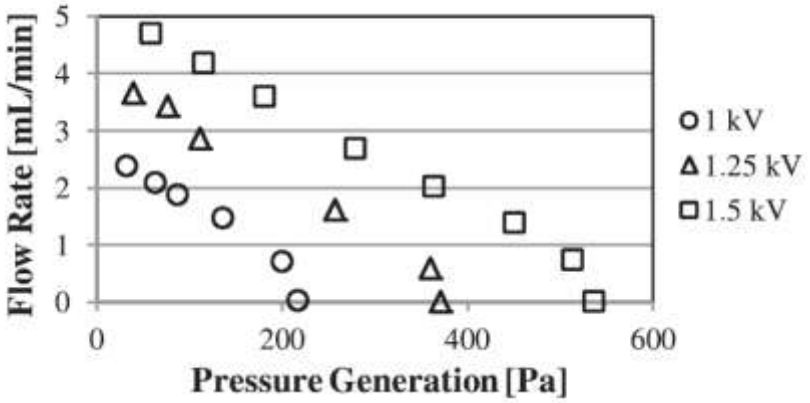

Figure 49: EHD conduction pump performance curve.

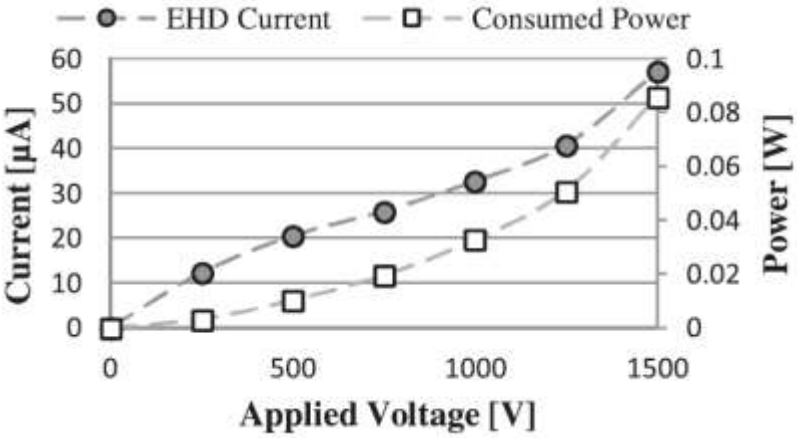

Figure 50: EHD pump power and current performance.

2.2.3 Experimental procedure

The entire experiment was first evacuated to 500 mTorr over a period of one hour, 3M™Novec™ 7600 Engineered fluid or refrigerant HCFC-123 was then allowed to enter the experimental setup until it was fully filled. An initial flow distribution was achieved with the activation of main mechanical pump and the regulation of needle valve in each branch. One of the EHD conduction pumps was then activated and the voltage applied to the EHD pump for all cases was gradually increased from 0V to 1.5kV in increments of 100V, 300V or 400V. After each increment, the system was allowed to settle until no measurable changes were observed in the recorded flow rate and pressure measurement. The upper limit of the applied voltage to the EHD conduction pump was set to 1500V, due to the maximum electric field that could be applied on the working fluid without initiating breakdown and potential failure of the EHD conduction pump when exceeding this voltage.

For two-phase experiments, the evaporator inlet fluid temperature was used to confirm that the bulk fluid temperature was at least 1°C below the saturation temperature, indicating that the liquid entering the evaporator was always sub-cooled. The evaporator exit fluid temperature, along with the absolute pressure close to the exits of the evaporators, monitored using a VALIDYNE P55 absolute pressure transducer (AP transducer) as shown in Figure 47, was used to determine the thermodynamic state of the fluid exiting the evaporator. For the duration of all two experiments, the outer surface temperature of evaporator insulation layer did not exceed the ambient temperature by more than 0.2°C, which corresponded to approximately 0.05W of total heat loss to the surroundings. Based on a one-dimensional radial conduction analysis, the difference between the inner and outer evaporator wall temperature at any point along the evaporator tube was less than 0.01°C at the highest heat flux of 1W/cm^2. Thus, the outer wall

surface temperatures measured by thermocouples were approximated as the inner wall surface temperatures.

Enough crushed ice was placed in the box for two-phase experiments to fully condense the vapor exiting the evaporators. This produced sub-cooled liquid at the condenser exit, which was verified by the fact that the liquid temperature at the exit of the condenser was always 5 °C lower than the corresponding saturation temperature.

2.3 Experimental results and discussion

2.3.1 Liquid-phase flow distribution control

For all the liquid-phase experiments, the voltage on the activated EHD pump was gradually increased from 0 V to 1.5 kV in increments of 100 V. After each increment, the system was allowed to settle until no significant changes were observed in the recorded flow rate and pressure measurements for at least 30 s.

A. Flow Redistribution

Experiments examining the ability of one EHD pump to adjust the flow distribution between three branches (refer to Figure 47) were performed with different initial flow rates. Figure 51 shows an initially equal flow distribution of 1.5 mL/min in each branch. As the EHD voltage is increased, the flow rates begin to diverge between the active branch, on which the EHD pump is activated, and the inactive branches, on which the EHD pump is not activated. In this case, the divergence began after an EHD voltage of about 500 V. At 1300 V the measured flow rates in the two inactive branches go down to zero, with no flow going forward or back-ward in those branches. After this flow starvation, back flow into the inactive branches is observed as the flow rates become negative at higher voltages. In this situation, flow from the main supply enters only into the active branch and circulates back through the inactive branches.

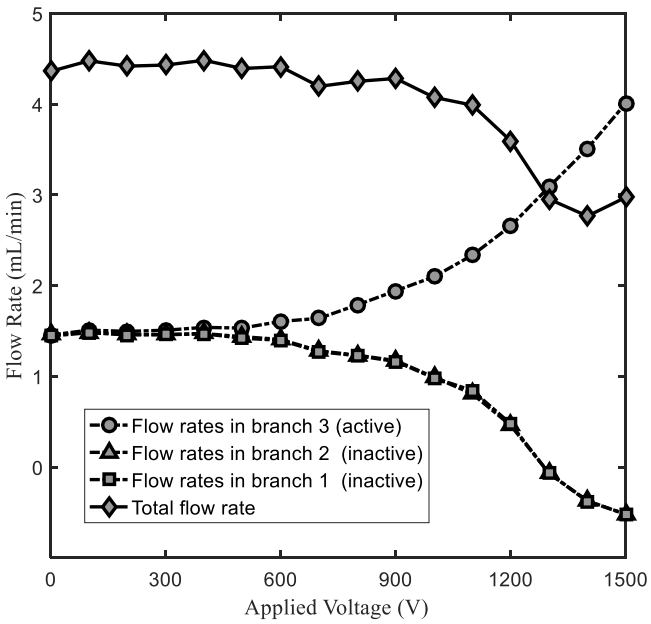

Figure 51: Experimental flow rates in three branches versus EHD voltage with initially equal 1.5 mL/min flow distribution.

The total experimental flow rate is also presented in this figure, it is significantly lower than the initial total flow rate of 4.5 mL/min at higher voltages. This difference is due to the changes in the flow distribution generating a greater pressure load on the mechanical supply pump, which was not automated to maintain the input flow rate by varying its output pressure. Considering the Poiseuille's law (the liquid flow in both branches is predominately laminar), if the initial total flow rate is divided into two branches equally, the pressure loss will be one half of that of a single branch receiving the total flow rate. This means the pressure load on the mechanical pump increases as all flow was redirected to the inactive branch, and therefore the total flow rate can no longer be maintained. The EHD generated flow rate opposed this decrease, but its contribution was relatively small.

The experimental pressure drop in three EHD pumps and the current of the active EHD pump for this case are presented in Figure 52. In this figure the initial pressure drops, at each zero

applied voltage, are slightly different between each branch due to non-uniformity between the flow paths caused by the manifold and unavoidable differences between the assemblies of each branch. Note that for the active branch, the negative pressure drop corresponds to the EHD pump's pressure generation. A lower pressure in the inactive branches corresponds only to changes in flow resistance due to changes in flow rates. In Figure 52, the pressure drop in the inactive branches changes to about zero at 1300 V upon the flow starvation and becomes slightly negative afterward due to the back flow.

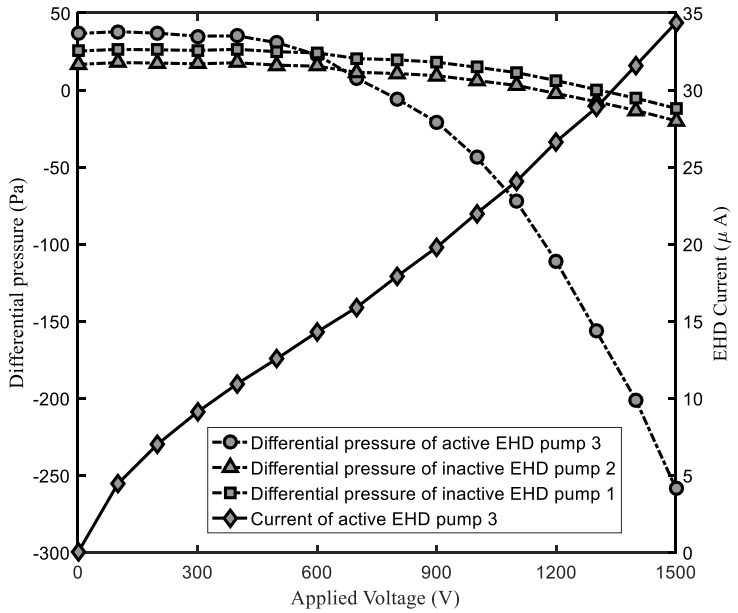

Figure 52: Experimental pressure drop across three EHD pumps and EHD current versus EHD voltage with initially equal 1.5 mL/min distribution.

As the initial flow rate in each branch was increased, flow starvation and back flow in the inactive branches were no longer possible, as can be seen in Figure 53. This figure shows an initial distribution of 5 mL/min in each branch. As the EHD voltage was increased, the flow was redistributed between three branches as it was the case in 1.5 mL/min test, but the flow rates in the inactive branches remained positive. Compared with Figure 51, it can be seen that the onset of the

divergence in flow rates for this case was delayed until after 800 V. Unlike the previous case, the total flow rate was not affected by the activation of the EHD pump at higher initial flow rates, since the pressure load in the system did not change as drastically as before, so it is omitted from the plot.

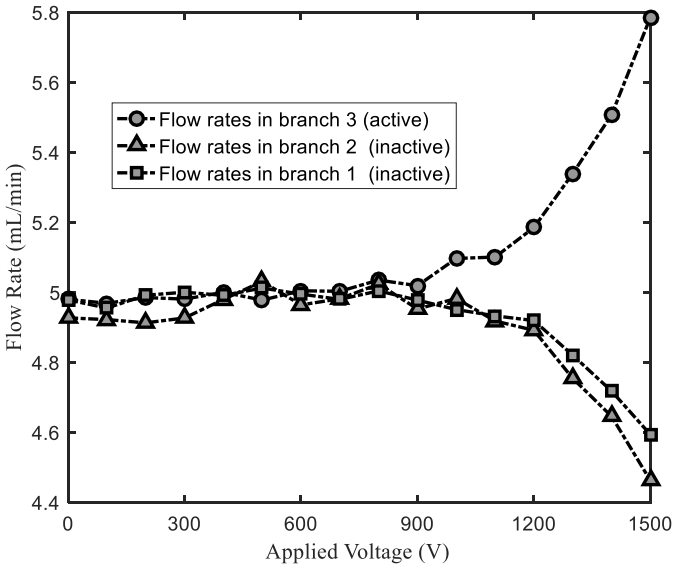

Figure 53: Experimental flow rates in three branches versus EHD voltage with initially equal 5 mL/min flow distribution.

Figure 54 shows the experimental pressure drop in three EHD pumps and the EHD current for this case. A comparison between Figures 52 and 54 show that the net pressure generation in the active branch for this case was significantly reduced versus the previous case. Figure 54 also shows a much larger difference between the pressure drops in each branch, regardless of the EHD voltage. These differences are due to the increase in flow rate through the non-uniform flow paths in each branch, resulting in different pressure losses between three branches.

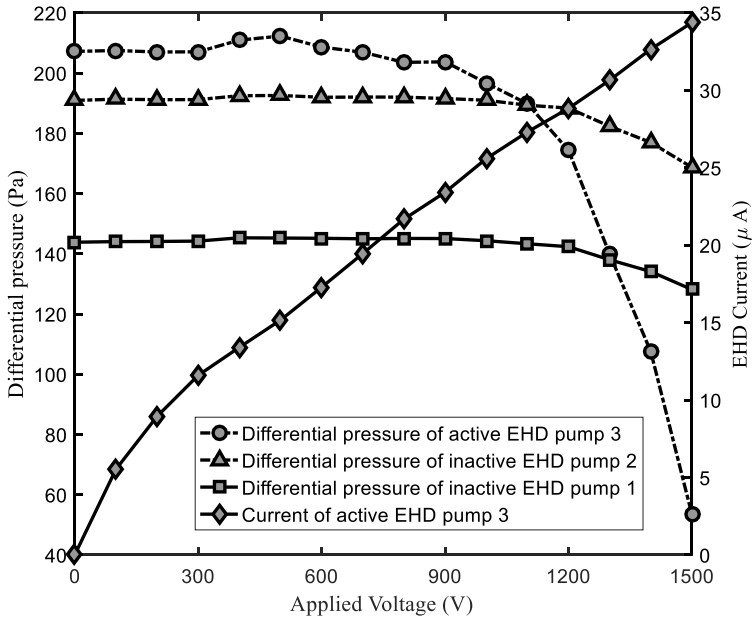

Figure 54: Experimental pressure drop across three EHD pumps and EHD current versus EHD voltage with initially equal 5 mL/min distribution.

The trend of delayed flow divergence and reduced final separation of the flow rates continued until an experimentally obtained limit of 8 mL/min initial flow rate per branch, as shown in Figure 55. At this limit, the EHD pump in the active branch did not have a significant effect on the flow distribution, even at the maximum applied potential of 1.5 kV. This behavior can be explained in part by the large pressure drop that the EHD pump had to overcome to increase the flow rate in its branch. However, the heterocharge layers that form near the surfaces of the EHD pump's electrodes must be considered as well. The thickness of these layers depends on the ratio between the electric relaxation time and the transit time of ions across the gap between the electrodes [105]. This thickness governs the amount of space charge available and therefore the magnitude of the net force generated by the pump. As the initial flow rate is increased the ion transit time is reduced, the ionic charges lose their charge faster due to recombination, and the heterocharge layers become thinner. The space charge available for the Coulomb force is therefore

reduced and the EHD pump is not able to generate as much pressure. This effect has been previously observed by Patel and Seyed-Yagoobi [13]. At the limiting case it would be possible for the transit time to become so short that the heterocharge layers would form only at a minimal thickness and apply only a minimal net force at any input voltage. This suggests that the heterocharge layers have eroded to the dimensions they would have had at this lower voltage.

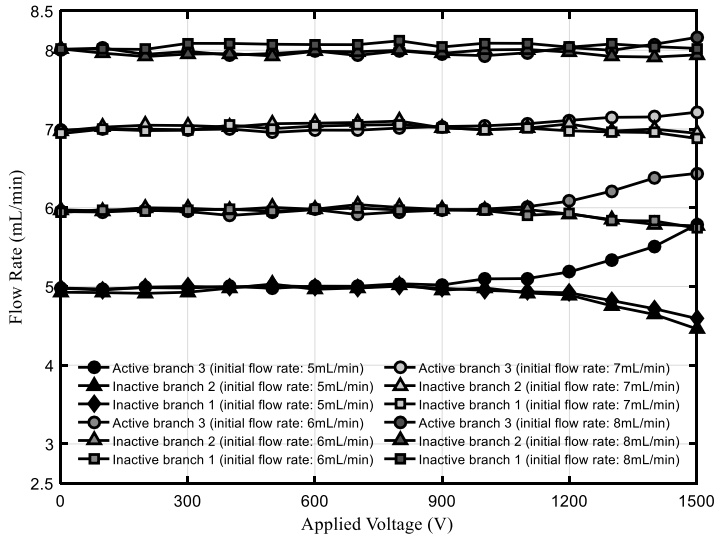

Figure 55: Comparison experimental flow rates in three branches versus EHD voltage with initially equal 5 mL/min, 6 mL/min, 7 mL/min and 8 mL/min flow distribution.

B. Maldistribution Correction

To examine the ability of the EHD driven setup to equalize an initially maldistributed flow, the needle valves on three branches were used to introduce initially unequal flow distributions. After handicapping the active branch with a lower flow rate than in the remaining branches, the EHD pump in the active branch was activated in an attempt to equalize the flow in each branch.

Figure 56 shows an initial distribution of 1.2 mL/min in the handicapped active branch versus 1.8 mL/min in the inactive branches (0.6 mL/min difference). Activating the EHD pump allowed the handicapped branch to recover and equalized the distribution to 1.6 mL/min in each

branch at about 900 V. Supplying additional voltage initiated a similar flow divergence and redistribution behavior as shown in the previous section. The pressure and current magnitudes shown in Figure 57 for this case are very similar to those shown in Figure 52, since the flow rates through all three branches were similar in magnitude to those shown in Figures 51 and 52.

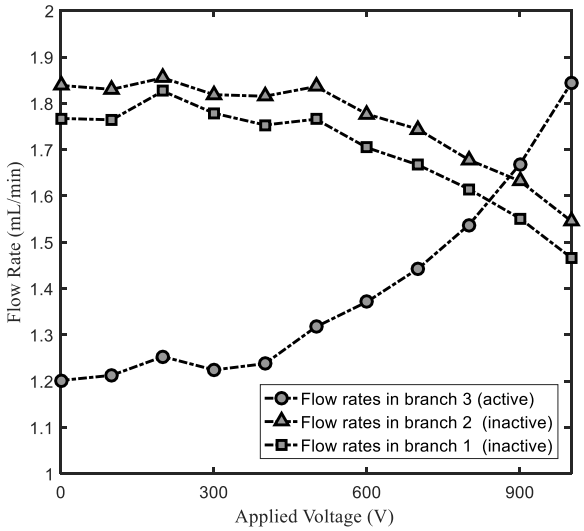

Figure 56: Experimental flow rates versus EHD voltage with 1.2 versus 1.8 mL/min initial maldistribution.

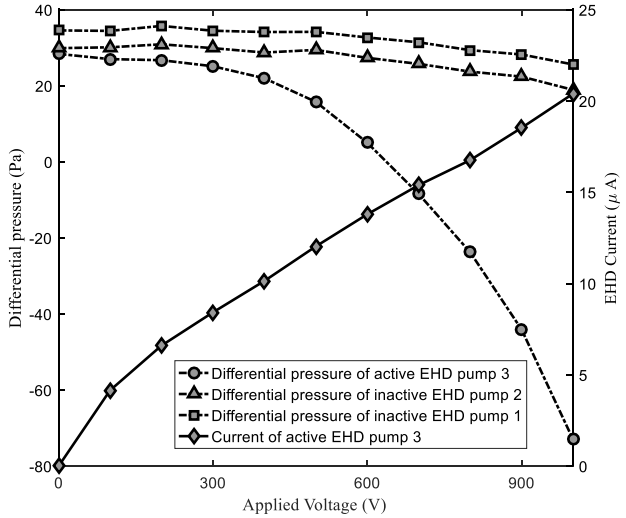

Figure 57: Experimental pressure drop of three EHD pumps and current versus EHD voltage with 1.2 versus 1.8 mL/min initial maldistribution.

Figures 58 and 59 show the flow rates, the pressure drop of three EHD pumps and EHD current for a case with a larger initial flow rate difference. The active branch flow rate was 0.8 mL/min and each inactive branch had a flow rate of 2.2 mL/min (1.4 mL/min difference). The total flow rate was not affected at higher voltages and was therefore omitted from Figure 58.

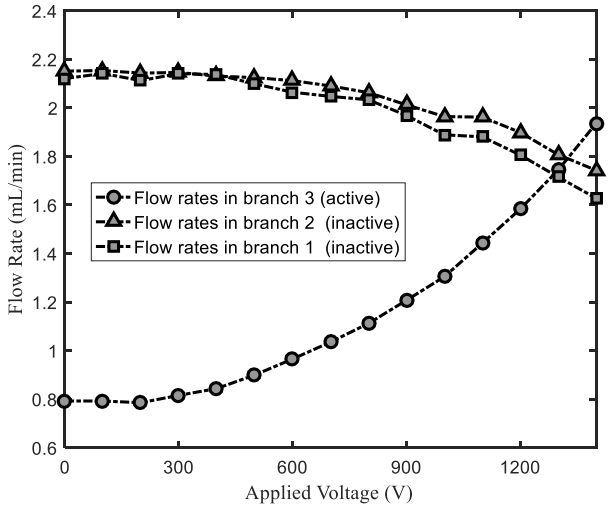

Figure 58: Experimental flow rates versus EHD voltage with 0.8 versus 2.2 mL/min initial maldistribution.

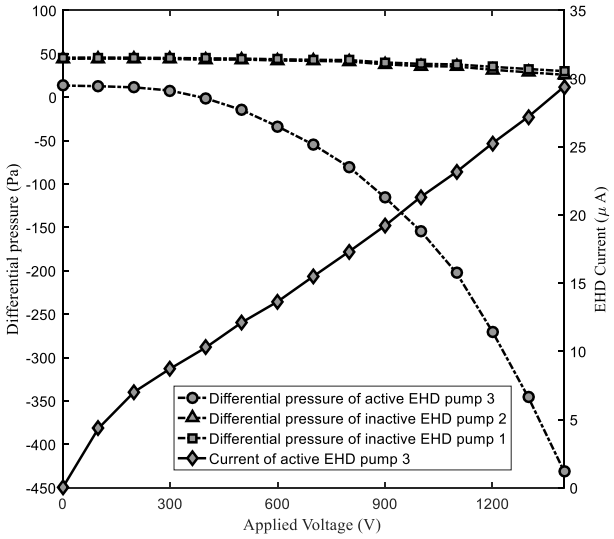

Figure 59: Experimental pressure drop of three EHD pumps and current versus EHD voltage with 0.8 versus 2.2 mL/min initial maldistribution.

Figures 60 and 61 show a case with 0.65 mL/min in the active branch and 2.35 mL/min in each inactive branch (1.7 mL/min difference). Unlike the previous two cases, the active branch was not able to fully equalize the flow even at the maximum applied voltage, with a final flow rate difference of 0.45 mL/min. This case shows the limit of the ability of the EHD pump in the active branch to recover from maldistribution at this total flow rate.

Finally, Figure 62 shows the flow rates versus EHD voltage for all the maldistribution cases. It clearly shows that as the initial flow rate difference between three branches increased, higher applied voltage to EHD pump was required for the flow equalization, which means the effect of the EHD pump became weaker.

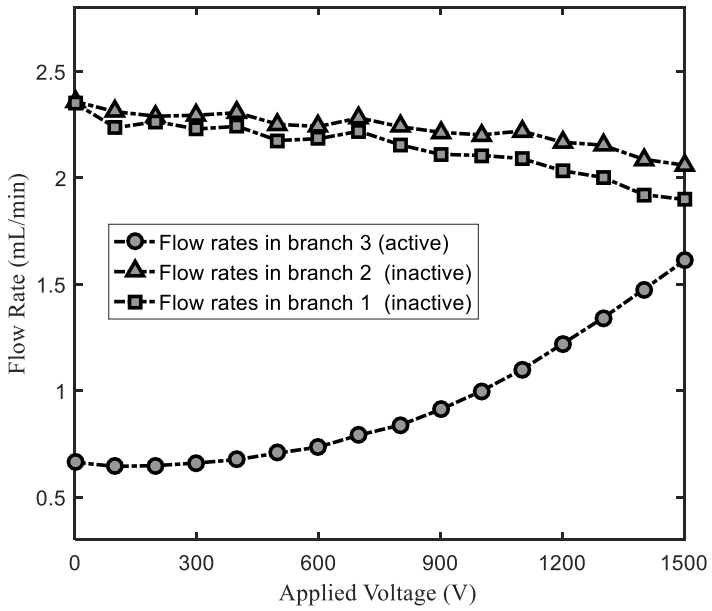

Figure 60: Experimental flow rates versus EHD voltage with 0.65 versus 2.35 mL/min initial maldistribution.

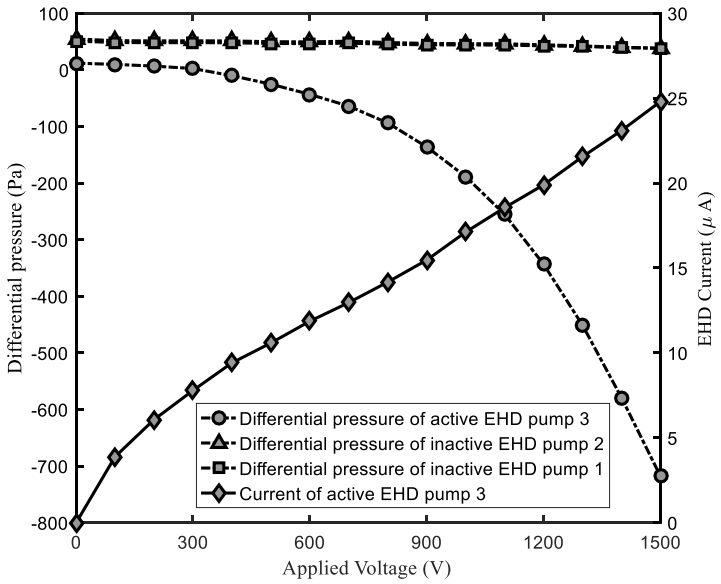

Figure 61: Experimental pressure drop of three EHD pumps and current versus EHD voltage with 0.65 versus 2.35 mL/min initial maldistribution.

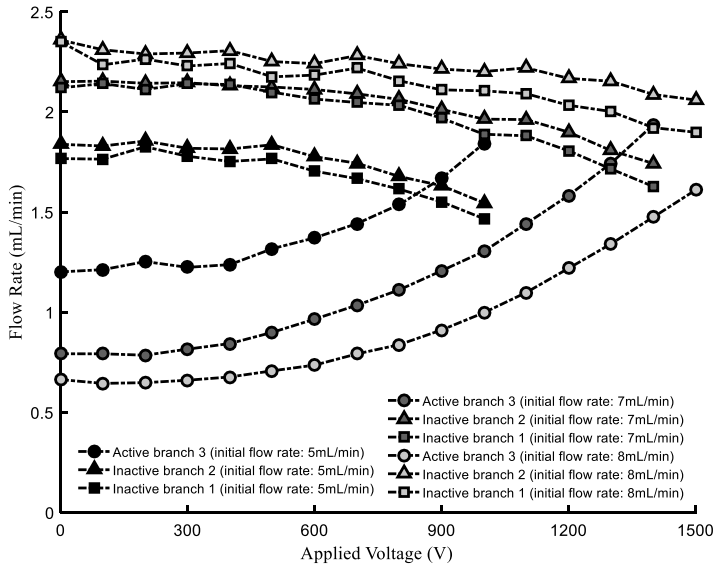

Figure 62: Experimental flow rates versus EHD voltage for all the maldistribution cases.

2.3.2 Two-phase flow distribution control

Initially, the mechanical pump in the main loop was activated to generate an equal liquid-phase flow distribution in each branch, 2.67 W of power (corresponding to 0.8 W/cm^2 applied heat

flux) was then applied to both evaporators to generate two-phase flow in both branches. The thermodynamic state of the two-phase flow was determined using the fluid temperature (29.05°C) and the absolute pressure (105.05 kPa) at the exit of the evaporators. As two-phase flow reached quasi-steady state, the EHD conduction pump in branch 1, as shown in Figure 47, was activated and the applied voltage was gradually increased from 0V to 1500 V in initial increments of 450V and subsequent increments of 300V when the applied voltage was higher than 900V. After each increment, the system was allowed to settle until no significant changes were observed in average flow rates and differential pressure measurements of EHD conduction pump section for at least 60 seconds.

With the activation of the EHD conduction pump installed in branch 1, the pressure generated by the activated EHD conduction pump adjusted the flow distribution between the two branches, as was the case for liquid-phase experiments. The flow rate measurement for each branch was averaged on a time interval of 30 seconds and is shown in Figure 63, at an applied voltage of 450V, the effect of the EHD conduction pump was not significant. The flow rates began to diverge between the active branch 1 and the inactive branch 2 at 900V. The effect of the EHD conduction pump on the flow rates of both branches became significant at applied voltage of 1200V or higher. At the maximum applied voltage of 1500 V, the flow rate in the inactive branch 2 became very low. In this situation, most of the liquid from the main loop flowed through branch 1, resulting in too little liquid being supplied to the inactive branch and a dryout phenomenon in the evaporator of branch 2, which caused the temperature measurement at the outlet of evaporator 2 to be significantly higher than the saturation temperature related to the absolute pressure measured at the same location. It is also marked by a sharp increase in the calculated vapor quality in at the exit of evaporator 2.

After the onset of dryout condition, a voltage of 1500 V was applied to the EHD conduction pump in branch 2 to facilitate the recovery from dryout condition. It can be seen in Figure 63 that the newly energized EHD conduction pump immediately began enhancing the flow in branch 2 while decreasing the flow rate in branch 1 and the vapor quality at the outlet of evaporator 2. The flow rates in both branches became steady in 10 minutes. Both flow rates did not change significantly after both of the EHD conduction pumps were deactivated and were very similar to those before the EHD conduction pump in branch 1 was activated.

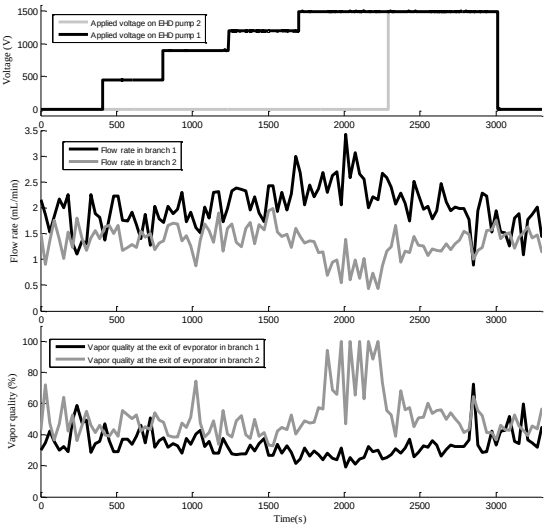

Figure 63: Measured flow rate in both branches and calculated vapor qualities at the exit of both evaporators

The net EHD conduction pump pressure generation averaged over a time interval of 30 seconds in both branches is illustrated in Figure 64. The initial negative differential pressure measurements were due to the pressure drop in EHD pump sections and predictably increased with the applied voltage. It is interesting to observe that the pressure generation of the EHD conduction pump in branch 1 at 1500V further increased when 1500V voltage was also applied to the EHD conduction pump in branch 2. This could be explained by the relationship between flow rate,

heterocharge layer thickness and pressure generation, as previously explained. The activation of the pump in branch 2 increased the flow rate in that branch and lead to a decrease of flow rate in branch line 1, reducing the flow resistance (pressure drop) as well as reducing the erosion of the heterocharge layers in the pump in branch line 1. These combined effects resulted in a higher net pressure generation in branch 1 than previously observed.

Figure 65 illustrates the current levels and associated power consumption of the EHD conduction pump in branch 1 (averaged on a time interval of 30 seconds) during the entire test. The EHD conduction pump current and power consumption increased with the increase in the applied voltage but always stayed below 200 μA and 0.3 W respectively. The maximum total electrical power consumption of the EHD pump in branch 1 (0.3W) was small compared with the actual total heat transport rate (5.34W) and its flow redistribution capability. It demonstrated that EHD conduction pumping is a very effective, low power method of controlling flow distribution and heat transfer in meso-scale systems.

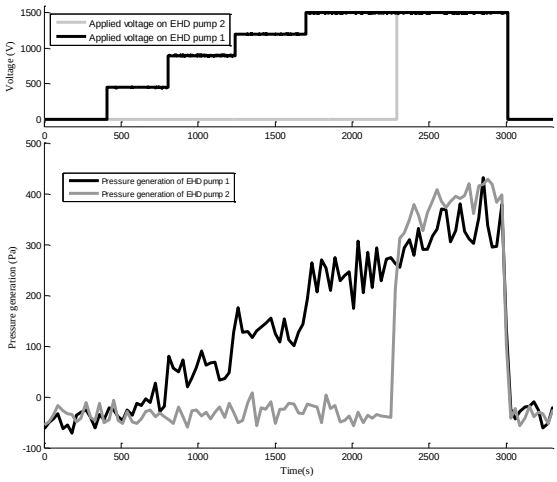

Figure 64: Measured pressure generation of the EHD conduction pumps in both branches

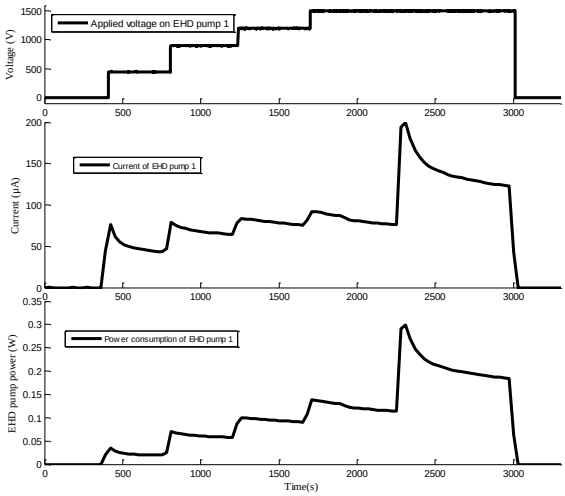

Figure 65: Current and power consumption of the EHD conduction pump in branch 1

The oscillation of the flow rates and pressure generation, shown in Figure 63 and Figure 64 respectively, indicates that the two-phase flow was unstable. It is typical for micro-channels and has been investigated by several researchers. The onset of two-phase flow instability in uniformly heated horizontal micro-channels was experimentally investigated by Kennedy et al [106]. Their study also proposed a correlation for predicting the onset of the flow instability, which is shown in equations 32 and 33. It was achieved via the pressure demand curve (pressure drop versus mass flow rate curve for a fixed heat flux and fixed channel exit pressure), along with the experimental data based on tubular test sections (1.17mm and 1.45mm in diameter, which are similar to the 1.5mm tubular evaporator used in the current study).

$$G_{sat} = \frac{q'' p_H L_H}{A(h_f - h_l)} \tag{32}$$

$$G_{OFI} = 1.11 G_{sat} \tag{33}$$

G_{OFI} is the maximum mass flux at which the onset of two-phase flow instability in micro-channels can initiate and it is 423 kg/m^2·s for the current study. It indicates that the entire flow rate

range examined in the current study, which was 6.9 kg/m^2·s – 46.9 kg/m^2·s, is within the flow instability regime.

The flow reversal phenomenon associated with this two-phase flow instability was also observed in the parallel branches in the current study. Figure 66 shows the instantaneous flow rates in both branches before and after the EHD pumps were activated. The vapor back-flow occurred when the flow rates decreased below zero. The figure clearly shows that the instantaneous flow rates in the two parallel branches are coupled and follow opposite trends from each other, whereby if the flow rate in one branch is increased, the flow in the other branch decreases and vice versa. The likely physical explanation is that the expansion of nucleating bubbles in the evaporator belonging to one branch caused the fluid in the other branch to be pushed back, nucleating in the second branch evaporator would then resist this effect and cause the fluid in the first branch to be pushed back as well, creating a coupled, oscillating instability between the parallel branches.

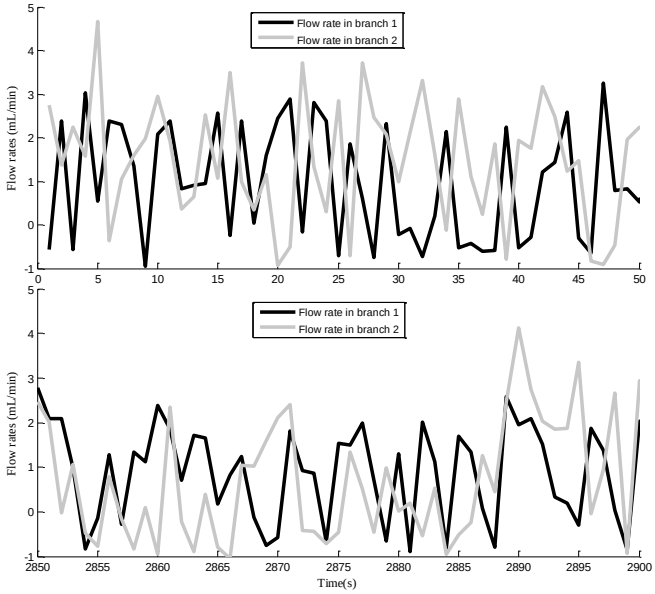

Figure 66: Instantaneous flow rates in both branches before (top) and after (bottom) the EHD pumps were activated

2.3.3 Flow distribution control with directionally reversed EHD pumping configuration

All the liquid phase flow distribution experiments discussed herein can be classified into two categories: initially uniform flow redistribution cases and flow maldistribution correction cases. For both categories, the liquid flow distribution was regulated by either activating the same direction EHD pump (installed in branch 1, see Figure 47) such that the flow in the active branch was facilitated and the flow in the inactive branch was suppressed, or by activating the reverse direction EHD pump (installed in branch 2, see Figure 47) in order to oppose the main flow stream, enhancing the flow in the other inactive branch 1.

A. Flow Redistribution

For all flow redistribution cases, the initial flow rates in both branches were adjusted to be equal. Flow distribution control with the activation of reverse EHD conduction pump was examined in this study and compared to those of the EHD pumping operating in the same direction. The measured steady state flow rates in both branches are shown in Figure 67 for an initially equal flow distribution of 0.5 mL/min, 1 mL/min, and 2 mL/min in each branch. As shown in Figure 67, for 0.5 mL/min case, the flow rates began to differ between the active branch 2 and inactive branch 1 immediately after a 100V of voltage was applied. The measured flow rate in active branch 2 became smaller than zero at 1000V and kept further decreasing as higher voltages were applied, indicating that flow from the main loop entered only the inactive branch and partially circulated back through the active branch as fluid always flows thorough the path with minimum pressure drop which was the active branch in this case. At an applied voltage of 1500 V, the flow rate difference between active and inactive branches reached a maximum, which was 1.8mL/min.

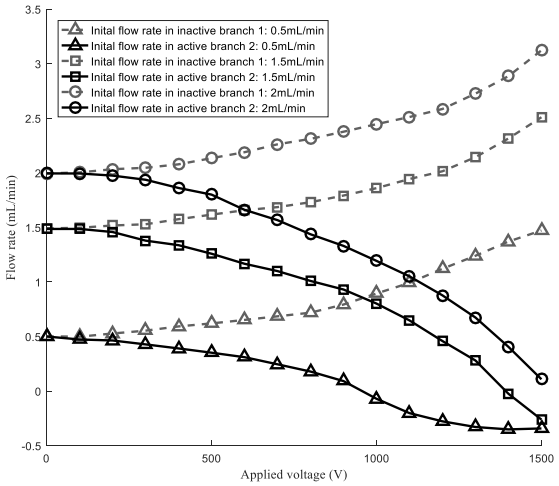

Figure 67: Measured flow rates in both branches for the reverse EHD pumping direction configuration (0.5 mL/min, 1.5 mL/min, and 2 mL/min case)

The incipient voltage for flow rate divergence between two branches was postponed to 200V when the initial flow rates were increased to 1.5 mL/min and 2 mL/min in each branch. The complete suppression of flow in the active branch 2 was also observed for 1.5 mL/min case, but it was no longer possible for 2 mL/min case. As the initial flow rates in both branches were increased, it required higher pressure generation by the EHD conduction pump in order to completely stop the flow in the active branch. The reverse flow would not be observed if the EHD conduction pump could not generate enough pressure and flow power for the corresponding initial flow rate, which was 2 mL/min in this case. The flow rate separation between two branches are summarized in Table VI with total flow rate of both branches at an applied voltage of 1500V. A maximum of 3.01 mL/min of flow rate separation was achieved for an initial flow rate of 2 mL/min in each branch. The differences between initial and final total flow rate of both branches for 1.5 mL/min and 2 mL/min cases are related with the increased pressure load on the mechanical pump in the main loop.

Table VI: Final flow rates difference between two branches and total flow rate of both branches

Initial flow rate in each branch	Initial total flow rate	Final flow rates difference	Final total flow rate
0.5 mL/min	1 mL/min	1.81 mL/min	1.01 mL/min
1.5 mL/min	3 mL/min	2.77 mL/min	2.25 mL/min
2 mL/min	4 mL/min	3.01 mL/min	3.23 mL/min

Additional experiments were conducted to determine the limit of the reverse EHD conduction pump being used to diverge the flow as an active flow distribution control mechanism. Measured flow rates in both branches for cases of initially equal flow distribution of 5 mL/min, 8 mL/min, 10 mL/min and 12 mL/min in each branch are shown in Figure 68. The corresponding applied potential for initiating flow divergence were 500V, 700V and 900V for 5 mL/min, 8 mL/min and 10 mL/min case, respectively. It is clear that the influence of EHD conduction pump on the flow distribution control became weaker as the initial flow rates increased. A higher flow rate required a higher applied potential to the EHD pump to initiate flow divergence between the two branches. At about 12 mL/min in each branch, the EHD pump considered in this study was not able to influence flow distribution even at the maximum applied potential of 1.5 kV.

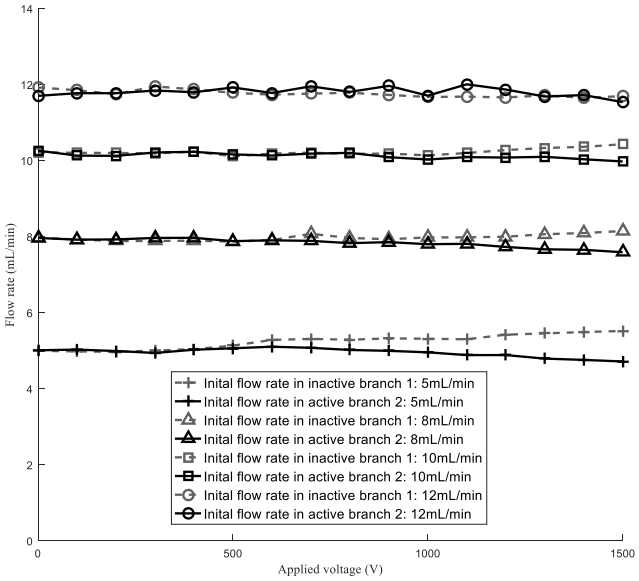

Figure 68: Measured flow rates in both branches for the reverse EHD pumping direction configuration (5 mL/min, 8 mL/min, 10 mL/min and 12 mL/min case)

Control experiments were conducted for comparisons of measured flow rates in both branches between activating the reverse direction pump and activating the same direction pump, which are shown in Figures 69-71 for initial flow rates of 0.5 mL/min, 1.5 mL/min and 2 mL/min. It can be seen in these figures that the same direction EHD pumping allowed for more flow on the branch where EHD pump was installed and reduced the flow on the other branch, whereas the reverse direction EHD pumping allowed for more flow on the branch with no EHD pumping and reduced the flow on the branch where EHD pump was installed.

The incipient voltage for the onset of flow rate difference between two branches for the same pumping direction configuration was about 400V for 0.5 mL/min case and was further postponed to 600V and 700 V for 1.5 mL/min and 2 mL/min case, respectively, while those values were not affected significantly for the reverse pumping cases. It is clear that the reverse pumping direction configuration was more favorable than the same pumping direction configuration for initiating flow redistribution. The final flow rates separation with both pumping directions are

similar for 0.5 mL/min case, whereas for the remaining cases, as the initial flow rate increases, larger final flow rates difference could be achieved with reverse EHD pump, showing that the reverse pumping direction configuration can be utilized to attain a higher maximum flow rate separation.

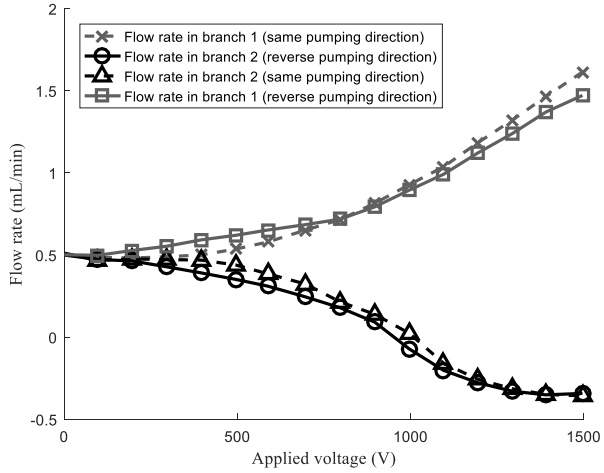

Figure 69: Comparison of measured flow rates in both branches between the two pumping direction configurations (initially equal flow distribution of 0.5 mL/min in each branch)

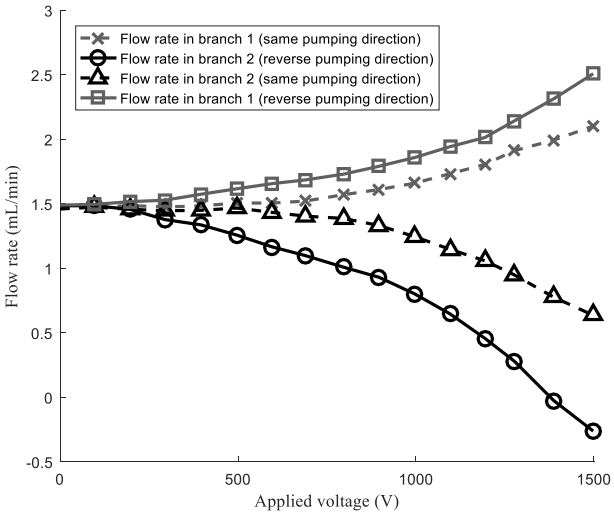

Figure 70: Comparison of measured flow rates in both branches between the two pumping direction configurations (initially equal flow distribution of 1.5 mL/min in each branch)

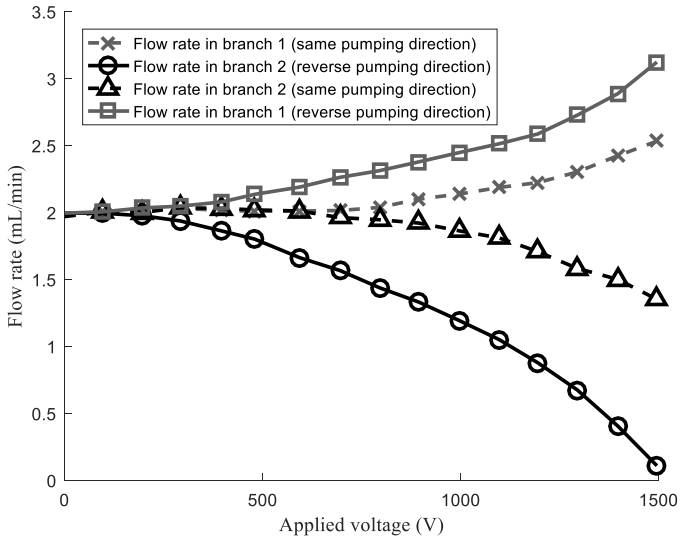

Figure 71: Comparison of measured flow rates in both branches between the two pumping direction configurations (initially equal flow distribution of 2 mL/min in each branch)

More significant influence the reverse pumping direction configuration had on flow distribution control can be further explained with the comparison of measured differential pressure illustrated in Figure 72. For all the tests, the upstream pressure of EHD pump minus the downstream pressure was used as the measured differential pressure. It should be pointed out that the absolute value of measured pressure was used for comparison as it was negative and decreased with applied voltage of EHD pump for the same pumping direction cases and was positive and increased with applied voltage for the reverse pumping direction cases. The negative pressure difference leads to suction of more liquid into the active branch for the same pumping direction cases, whereas the positive pressure difference hinders the flow from entering the active branch for the reverse pumping direction cases. In either case, it is the pressure generated by the activated EHD conduction pump that regulated the flow distribution between the two branch lines.

The non-zero measured differential pressure in Figure 72 agrees well with the incipient flow divergence showed in Figures 69-71. It occurred at 400V, 600V and 700V applied voltages

for 0.5 mL/min, 1.5 mL/min and 2 mL/min cases for the same pumping direction configuration and was almost immediate for the reverse pumping direction cases. The difference in incipient flow divergence between the same and reverse pumping directions can be attributed to the effect of flow directions on the interior flow condition within the EHD pump as well as the EHD conduction pumping mechanism. Once the EHD conduction pump is activated, the flow condition inside its inner channel is very different than elsewhere: the velocity profile near the channel wall induced by the EHD pump is superimposed on the main flow, resulting in a higher velocity close to the wall for the same pumping direction and a lower velocity near the wall for the reverse pumping direction. The higher velocity causes higher flow resistance for the same pumping direction and impairs the capability of EHD pump of regulating the flow. The opposite effect of the reverse pumping direction strengthens its influence on flow control.

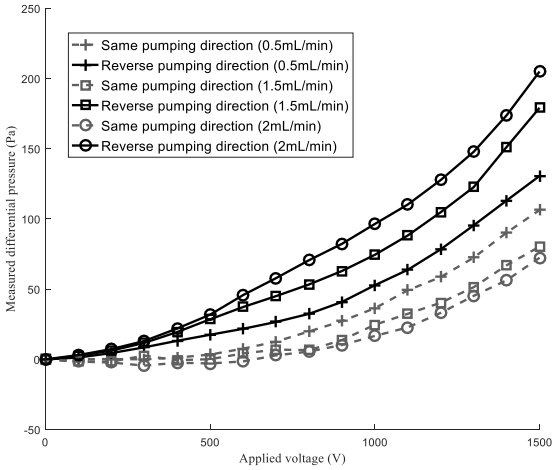

Figure 72: Comparison of measured differential pressure across EHD conduction pumps in the active branch between the two pumping direction configurations (0.5 mL/min, 1.5 mL/min and 2 mL/min cases)

This difference in flow condition also manifests itself in space charges density in the heterocharge layers that form near the walls of the EHD pump's electrodes. The net space charge

density depends on the ratio between the electric relaxation time and the transit time of ions across the gap between the electrodes [105]. For the reverse pumping direction, the flow velocity in the heterocharge layers is reduced, resulting in longer ion transit time and thus higher net space charge density. Coulomb force associated with space charge density is therefore increased and the EHD pump becomes more effective. The decrease in flow resistance inside the EHD pump and increased Coulomb force generation combine to make the reverse pumping direction more efficient.

The change in flow rate in the active branch of reverse EHD pump is also favorable to performance since it kept decreasing with applied voltage, whereas for the same pumping direction configuration, the flow rate kept increasing in the active branch. Lower flow rate in the active branch of reverse EHD pump results in lower flow resistance and, in turn, strengthen its influence on the inactive branch. It is concluded that the higher space charge density within the heterocharge layer, thus higher Coulomb force and pressure generation, combined with lower flow resistance in the active branch, makes directionally reversed EHD conduction pumping a better pumping configuration.

Figure 73 illustrates the current and power consumption levels of the EHD conduction pump in the active branch for both pumping direction configurations. The current and power consumption of EHD conduction pump increased with applied voltage but always stayed below 110 μA and 0.3 W, respectively.

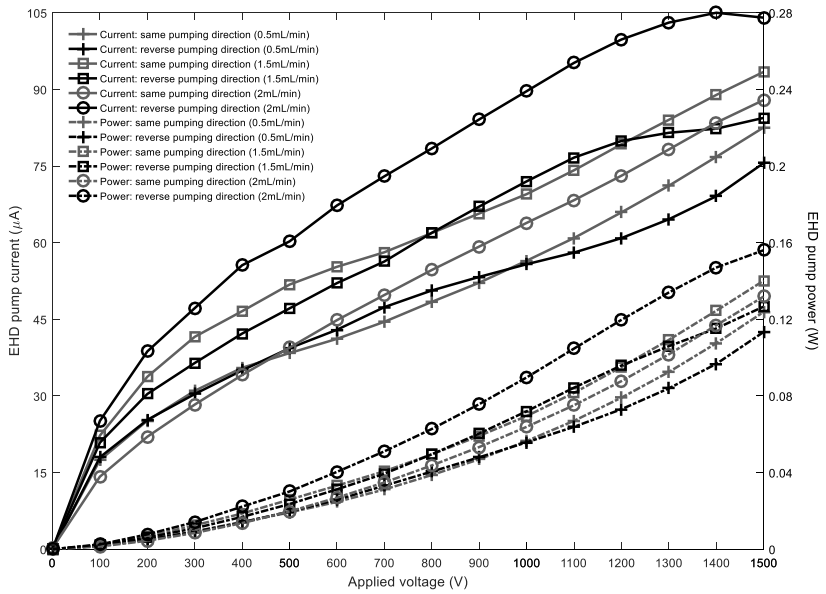

Figure 73: Comparison of EHD pump current and power in the active branch between the two pumping direction configurations (0.5 mL/min, 1.5 mL/min and 2 mL/min cases)

B. Flow Maldistribution Correction

The reverse pumping direction configuration was also examined with its capability of equalizing an initially maldistributed flow, and then compared with the same pumping direction configuration. Three different initial maldistributed flow distributions were tested: 1.15 mL/min and 1.75 mL (0.6 mL/min difference), 1 mL/min and 1.9 mL (0.9 mL/min difference) and 0.55 mL/min and 2.35 mL (1.8 mL/min difference), the total flow rate was kept at 2.9 mL/min for better comparison and the experimental results are shown in Figures 74, 75 and 76 respectively.

For all the cases, the flow rate difference between the two branches diminishes with the activation of the EHD pump either by facilitating the flow in active branch 1 for the same pumping direction configuration or by reducing the flow in active branch 2 for the reverse pumping direction configuration. A comparison of Figures 74-76 shows that as the difference in initial flow rates increased, the flow rate equalization between the two branches was postponed as it required higher

pressure generation of EHD pump with higher applied voltage to overcome larger flow rate difference. This phenomenon was achievable for an initial flow rate difference of 0.6 mL/min and 0.9 mL/min case, but unfulfilled for 1.8 mL/min case which shows the limit of EHD pump being able to equalize the flow rates in two branches from an initial maldistribution condition for both pumping direction configurations.

Similar to flow distribution cases, compared to the same pumping direction configuration, an almost immediate control on the initial maldistributed flow was realized with the reverse pumping direction configuration and therefore the flow equalization between two branches was advanced. The more favorable inner flow condition inside the EHD conduction pump and lower flow rate in the active branch in the reverse pumping direction configuration accounts for these better performance.

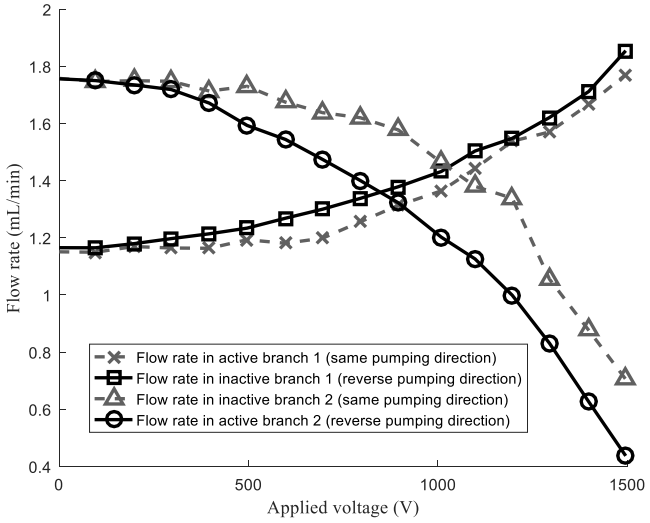

Figure 74: Comparison of measured flow rates in both branches between the same pumping direction and the reverse pumping direction (initially maldistributed flow distribution of 1.15 mL/min and 1.75mL/min)

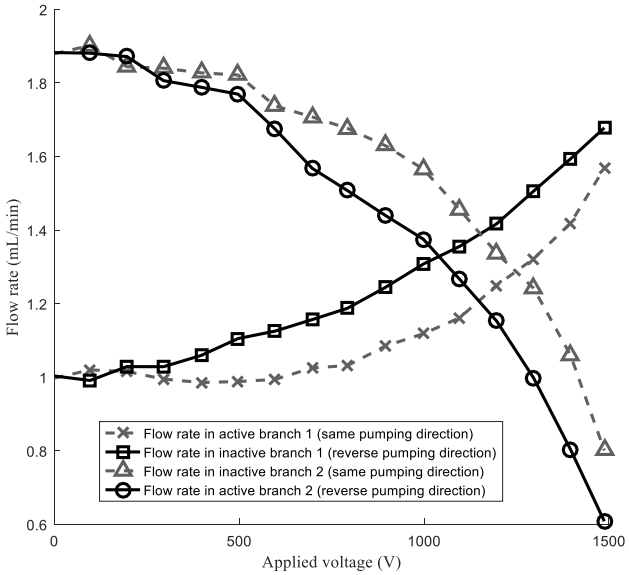

Figure 75: Comparison of measured flow rates in both branches between the same pumping direction and the reverse pumping direction (initially maldistributed flow distribution of 1 mL/min and 1.9 mL/min)

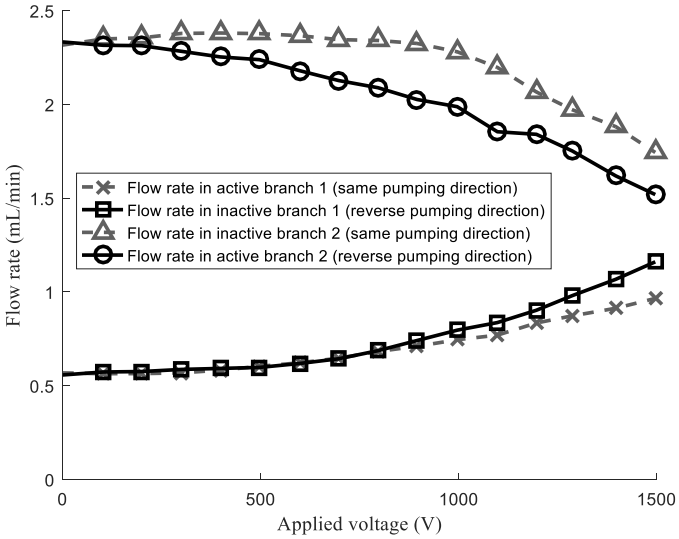

Figure 76: Comparison of measured flow rates in both branches between the same pumping direction and the reverse pumping direction (initially maldistributed flow distribution of 0.6 mL/min and 2.3 mL/min)

C. Two-phase flow distribution control

The initial flow rates in both branches were adjusted to 0.75mL/min. Flow distribution control with the activation of either the reverse or the same EHD conduction pump was examined. The measured steady state flow rates in both branches are shown in Figure 77. It can be seen that, just as with the liquid flow tests, the same direction EHD pumping allowed for more flow in the branch where EHD pump was installed and reduced flow in the other branch, whereas the reverse direction EHD pumping allowed for more flow in the branch with no EHD pumping and reduced flow in the branch where EHD pump was installed. The onset of flow rate difference between two branches for the same pumping direction configuration was not seen until 900V of voltage was applied to the EHD conduction pump, while for the reverse pumping configuration, it was seen with the activation of EHD conduction pump. A much larger final flow rate difference was again observed with reverse EHD pumping, indicating that the reverse EHD pumping mode is more effective for two-phase flow redistribution control than the same EHD pumping mode. The comparison of measured differential pressure across the active EHD conduction pump sections for both pumping direction modes is illustrated in Figure 78. The general trend was the same as those for liquid phase experiment and can be explained similarly.

Comparison of wall temperature of evaporator in branch 2 at various locations for the reverse and the same pumping direction configurations is shown in Figures 79 and 80, respectively. It can be seen that the dry out phenomenon, characterized by a quick continuous temperature rise, happened with the reverse pumping configuration at an applied voltage of 1200V, while for the same pumping configuration, it did not happen even at a maximum of 1500V applied voltage. It is interesting to observe that the last wall temperature of evaporator for the reverse pumping configuration decrease as 1200V voltage was applied. Similar phenomenon happened for all the

other evaporator wall temperatures as the EHD pump applied voltage was increased to 1500V. This is due to the reverse flow into the evaporator in branch 2, this had a good agreement with the flow rates measurement (very close to 0 mL/min as shown in Figure 77) and was observed through a small sight glass section after the evaporator during the experiment.

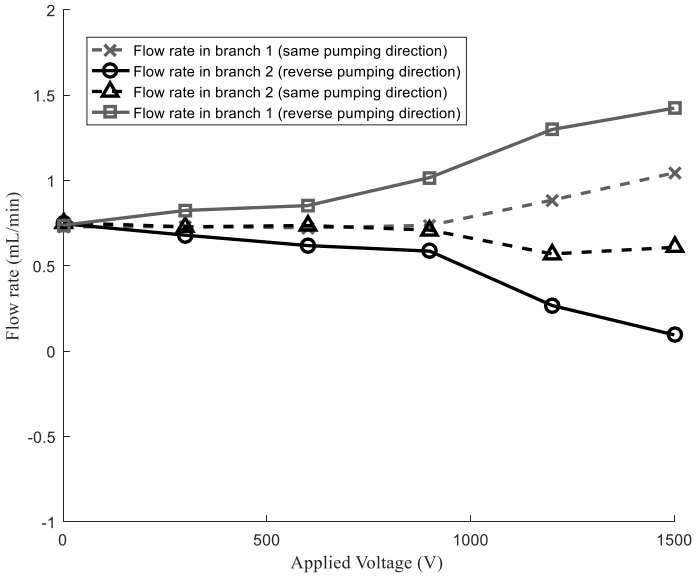

Figure 77: Comparison of measured flow rates in both branches between the two pumping direction configurations (initially equal two-phase flow distribution of 0.75 mL/min in each branch)

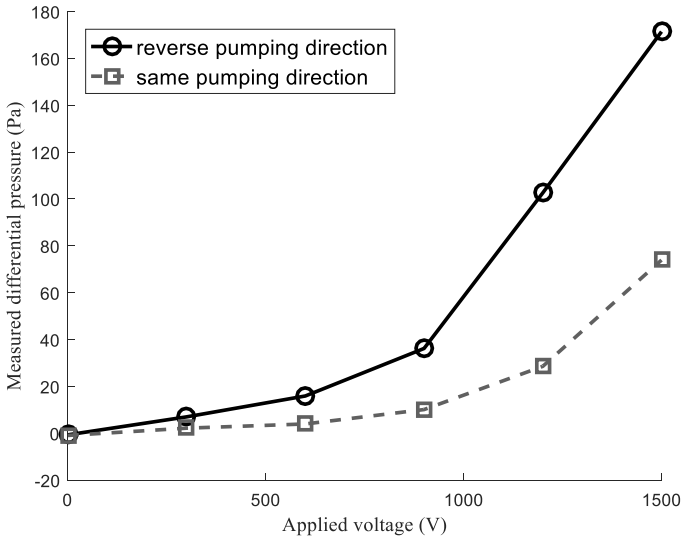

Figure 78: Comparison of measured differential pressure across EHD conduction pumps in the active branch between the two pumping direction configurations (initially equal two-phase flow distribution of 0.75 mL/min in each branch)

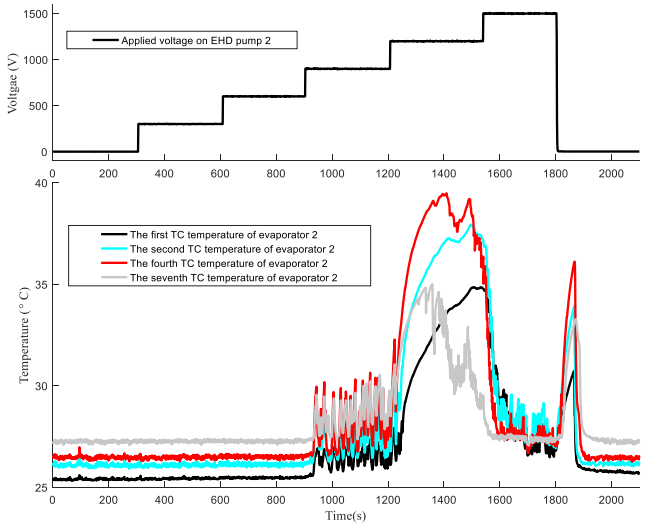

Figure 79: Comparison of wall temperature of evaporator 2 at various locations for the reverse pumping direction configurations (initially equal two-phase flow distribution of 0.75 mL/min in each branch)

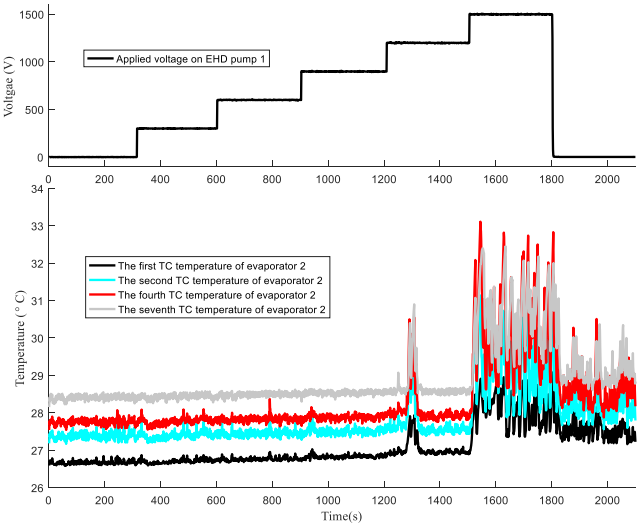

Figure 80: Comparison of wall temperature of evaporator 2 at various locations for the same pumping direction configurations (initially equal two-phase flow distribution of 0.75 mL/min in each branch)

2.4 Conclusions

Liquid flow distribution control driven by EHD conduction pumping was first successfully demonstrated in meso-scale with experimental setup 1. It was shown that with the activation of one of the EHD conduction pumps, flow rates could be directed to a corresponding branch in a controllable fashion by increasing its applied voltage, resulting in a decrease in the flow rates of other branches. Its applications include diverting flow to location with a higher heat transfer need than others and recovering from a maldistribution of flow.

Meso-scale flow distribution control of two-phase flow via EHD conduction pumping was then examined with experimental setup 2. The experimental results showed that two phase flow distribution between two meso-scale parallel evaporators can be effectively controlled via EHD conduction pumping. The maximum total electrical power consumption of the EHD pump in branch 1 (0.3W) was small compared with the actual total heat transport rate (5.34W) and its flow

redistribution capability. The successful recovery of evaporator dryout condition via the activation of the EHD conduction pump in the initially inactive branch was demonstrated. The two phase flow instability and the back-flow phenomenon observed were caused by the interaction between the coupled two-phase flows in both branches and this conclusion is supported by the instantaneous flow rate measurement in both branches.

Liquid-phase and two-phase experimental study demonstrated that EHD conduction pumping is a very effective low power method capable of controlling flow on demand in meso-scale flow distribution and heat transfer systems. EHD driven flow distribution is therefore shown to be viable in smaller scales, with possible applications in electronics cooling.

Both liquid-phase and two-phase flow distribution control in meso-scale with directionally reversed EHD conduction pumping mode was experimentally investigated lastly. Experimental results showed that the same direction EHD pumping allowed for more flow on the branch in which EHD pump was installed and reduced the flow on the other branch, while the reverse direction EHD pumping allowed for more flow on the branch with no EHD pumping and reduced the flow on the branch in which EHD pump was installed. The results also showed that the reverse pumping direction configuration was more effective than the same pumping direction configuration: 1. Almost immediate influence on the flow distribution with lower applied voltage on EHD conduction pump. 2. Advancing the flow equalization for the maldistribution correction cases. 3. Attaining larger flow separation between the active and inactive branches. The better performance of reverse EHD conduction pumping was believed to be related to the favorable heterocharge layer development which is also affected by the main flow including its direction with respect to the pumping direction.

CHAPTER 3 EXPERIMENTAL STUDY OF LIQUID THERMAL HOMOGENIZATION IN A SPHERICAL RESERVOIR WITH EHD CONDUCTION PUMPING MECHANISM

3.1 Introduction

Thermal homogenization with non-mechanical fluid circulation and mixing inside an enclosure is of significant importance in various applications such as maintaining isothermal conditions in a liquid reservoir in space applications. As a promising method, fluid circulation in an enclosure with electrohydrodynamic (EHD) pumping were studied in several research. Shu and Lai [107] studied the effect of electric field on buoyancy-induced flows in an enclosure. Their geometry consisted of a 2D rectangular configuration with a wire passing through to provide the electric field. EHD-enhanced heat transfer was numerically examined for laminar natural convection in this rectangular enclosure with differentially heated vertical walls. The effect of added electric field on the flow stability was investigated and they found that for a given Rayleigh number, the flow and temperature fields change from a steady state to periodic and non-periodic convection as the applied voltage increases. Heat transfer enhancement increases with the applied voltage but decreases with the Rayleigh number and the maximum enhancement in heat transfer can be as high as seventeen times of that with no electric field. They [108] then numerically examined the effects of Joule heating resulting from the corona discharge on electrodydrodynamically enhanced natural convection based on the same geometry. Numerical results of transient variation of isotherm and streamline patterns as well as a parameterization of the Nusselt-versus-Rayleigh number relation in terms of the electrical field conditions showed that the effect of Joule heating diminishes as the Rayleigh number increases. Therefore, they concluded that EHD-enhanced natural convection is most effective for Rayleigh numbers in the intermediate range (i.e., $10^4 \leq \mathrm{Ra} \leq 10^5$).

Despite the significant heat transfer enhancement achieved in the above researches, the EHD mechanism, however, was due to ion injection. As another mechanism of electrohydrodynamic pumping, EHD conduction phenomenon can also be utilized to create flow circulation and mix one or multiple fluids within an enclosure; a related numerical study was initially carried out by Jeong et al. [109] for an isothermal fluid. They showed that, with a proper electrode design, a significant flow circulation and mixing could be achieved. Their numerical results therefore confirmed the presence of the induced flow (i.e. circulation and mixing) within an enclosure based on the EHD conduction phenomenon.

Yazdani and Seyed-Yagoobi [110] extended his work by numerically studying the characteristics of electrically driven fluid circulation in a spherical reservoir based on the conduction phenomenon and presenting numerical results of the electric field, net charge density, and electric body force distributions, as well as the resultant flow fields. They considered two types of electrode designs. The first electrode design, as shown in Figure 81, is of the form of five flush embedded electrode pairs on the inner surface of the spherical reservoir, with the narrower (ground) electrode located above the wider (high-voltage) electrode. The flow field result followed the systematic pattern generated from the narrower electrodes toward the wider electrodes in the vicinity of the embedded electrodes, although EHD effect is restricted to the region close to the wall. The second electrode design, also shown in Figure 81, is one pair of concentric electrodes located on both sides of the central plane and is a simplified representation of perforated electrodes inserted into the reservoir. The major consideration of this design is to penetrate the effects of the EHD conduction phenomenon into the fluid, which is necessary for large reservoirs. For this design, the electric body force was present near the electrode pair and local fluid circulation are generated between the two electrodes. The effects of essential dimensionless numbers on the

performance of the EHD-induced fluid circulation were also studied. Numerical results showed that EHD pumping performance increased with Re_{EHD} and M_0 and decreased with C_0 for both electrode designs.

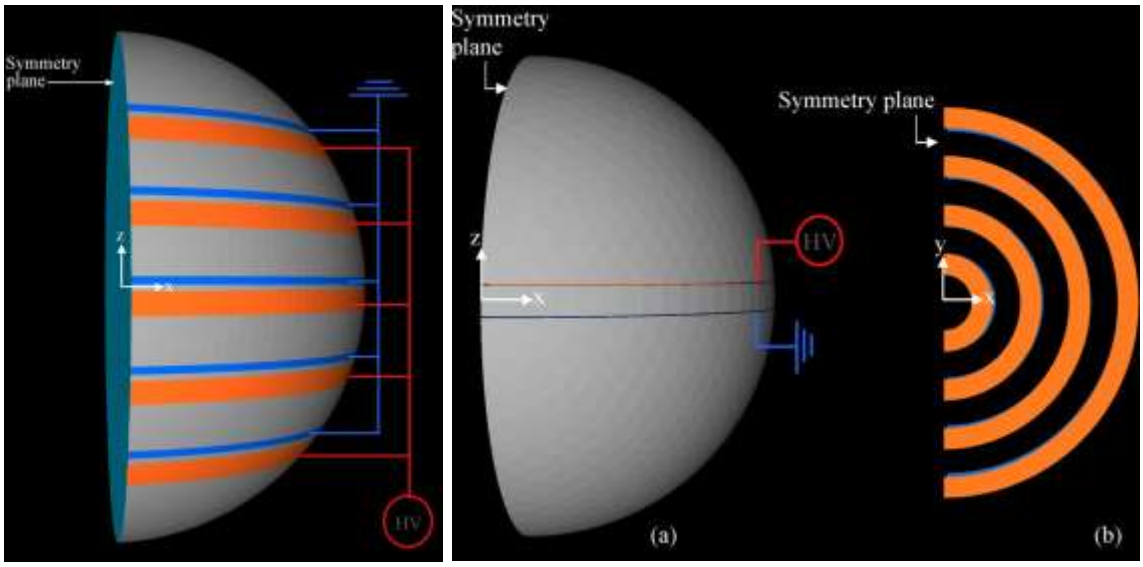

Figure 81: Electrode design No.1 (left) and No. 2 (right) [110]

They [111] then further investigated the thermal homogenization of a dielectric liquid with an initial non-uniform temperature distribution based on the first EHD conduction pump design in [110] and presented the numerical simulation results of electric field and electric body force distributions along with resultant velocity field at the final steady-state condition. The mixing mechanism is illustrated by the time evolution of temperature distribution inside the reservoir. The effects of primary dimensionless numbers on the mixing time are studied. The results confirmed that the EHD conduction mechanism can be utilized to effectively circulate and mix a thermally non-homogenous liquid inside a reservoir.

As an extension of Yazdani and Seyed-Yagoobi's [111] work, this paper experimentally and numerically studies fluid circulation and thermal homogenization characteristics inside a spherical reservoir due to the EHD conduction pumping with a new electrode design, which is

different than the symmetric design considered in [111]. This design is an asymmetric design, and thus can generate a global motion of dielectric liquid instead of local circulation. A test facility was developed and used for experimental study of which the results were compared with numerical analysis.

3.2 Experimental apparatus and procedure

3.2.1 Experimental apparatus

The SolidWorks design and photograph of the experimental apparatus are shown in Figure 82; the apparatus was specifically designed in such a way that a spherical reservoir (130 mm in diameter) formed in its interior. A clear plastic, Veroclear, was chosen as the material of the tank for observation of liquid mixing. It is also more electrically insulated than metals and poses a much smaller risk of creating and accumulating charges on the body of the tank.

The experimental apparatus with all of its features including holes for fittings was 3D printed using an Objet260 Connex Rapid Prototype machine. To make the reservoir more transparent, its interior surface was polished using sandpaper. The process started with the use of 220 grit and 320 grit sandpapers and was finished using 400 grit sandpaper. This sanding changed the rough interior surface of the reservoir into a smooth one. When liquid corn oil was put into the reservoir, the top of the apparatus became translucent, allowing the electrodes to be visible.

A cartridge immersion heater was inserted into the spherical reservoir and was used to provide an initial thermal inhomogeneity of the corn oil, which was used as the testing fluid for this study. This heater has a maximum voltage output of 240 V and a maximum output power of 400 W, allowing it to heat the corn oil to well above the desired value. A sight glass was installed into the side of the apparatus as well for better visualization of the experimental process.

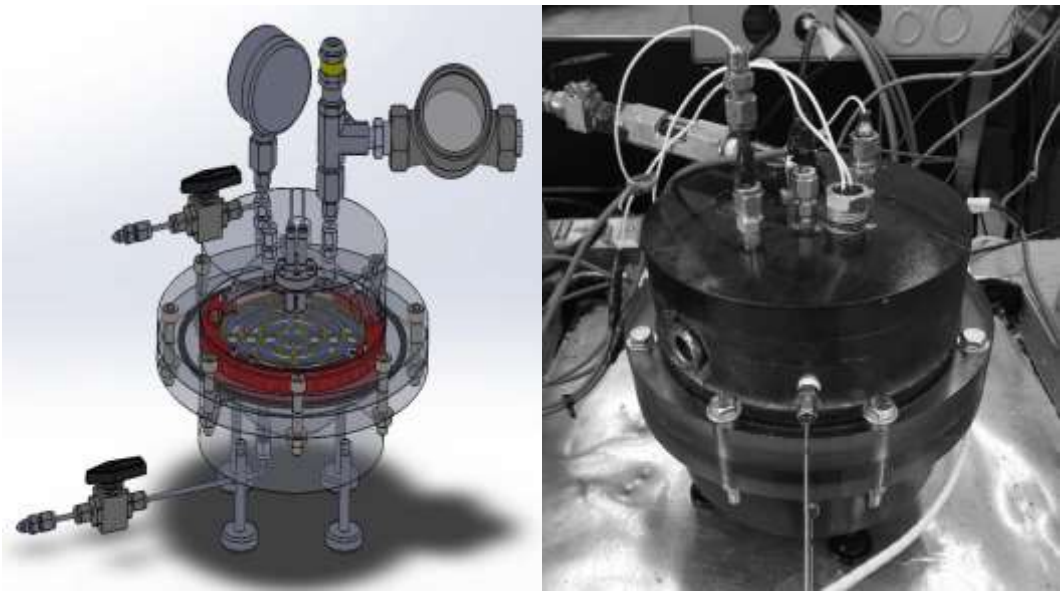

Figure 82: SolidWorks design and photograph of the experimental apparatus

Two T-type probe thermocouples and a probe RTD were used to measure fluid temperature in six locations, illustrated in Figure 83, in two separate sets of experiments. A high voltage power supply was used to apply voltage to the EHD conduction pump and another power supply was used for the cartridge insertion heater.

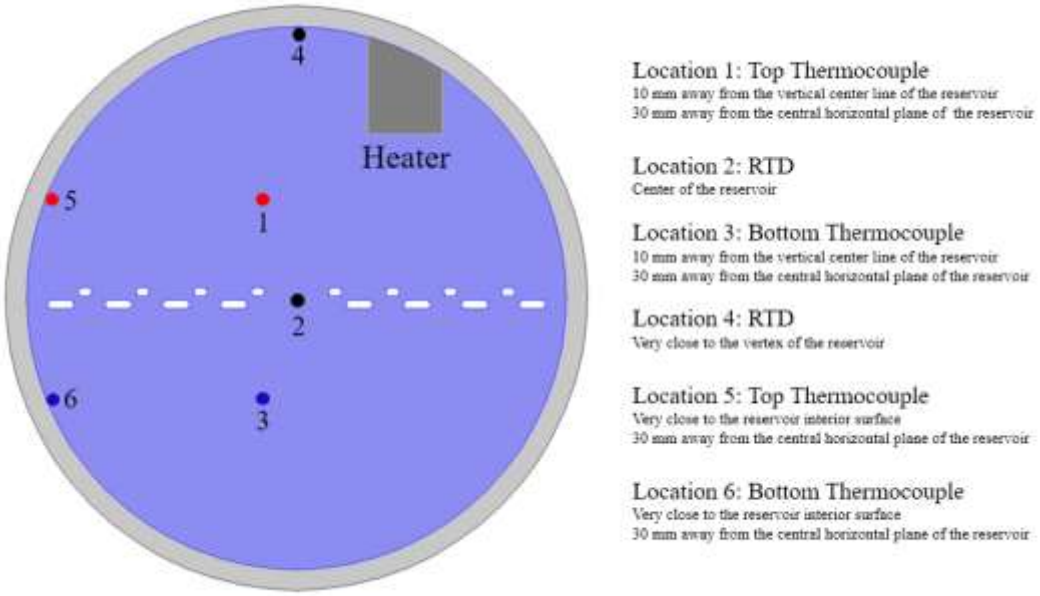

Figure 83: Locations for fluid temperature measurement

National Instruments PCI 6024E and USB-9219 data acquisition systems were used to acquire experimental data along with an NI LabVIEW Virtual Instrument program. The Maximum systematic error of various measurement devices and experimental uncertainty are listed in Table VII.

Table VII: Maximum systematic error of various measurement devices and experimental uncertainty for chapter 3

Measurement	Maximum systematic error
Temperature (RTD)	±0.15°C
Temperature (Thermocouple)	±0.5°C
Voltage of HV Power Supply	±30 V
Current of HV Power Supply	±2 μA
Voltage of Evaporator Power Supply	±0.06 V
Derived quantity	**Maximum Uncertainty**
Evaporator Heater Power, Q	±0.1%

3.2.2 Electrode design of EHD conduction pump

The electrodes of EHD conduction pump were made of copper and were held in the central plane of the spherical reservoir with a four-piece insulating ring which was also 3D printed. The width of the ground electrode was set to be half the size of the high voltage electrode to create the asymmetry. The center of each concentric ring for both electrodes was placed in the same location, the gap between each ring was adjusted so that there was a 1 mm horizontal gap between the closest edges of each electrode ring. The major consideration of this design is to penetrate the effect of the EHD conduction phenomenon into the fluid, which is necessary for large reservoirs and allow for a larger mixing effect than the previous electrode configuration

consider in [110]. The dimensions of EHD pump electrodes and a photograph of the EHD pump electrodes are provided in Table VIII and Figure 84, respectively. The high voltage electrode is represented with blue and the ground electrode is represented with gold. Two 20 kV rated wires were soldered onto the electrodes and connected to the high voltage power supply and the common ground.

Table VIII: Dimensions of EHD pump electrodes

HV electrode width (mm)	***Ground electrode width (mm)***	***HV electrodes spacing (mm)***	***Ground electrode spacing (mm)***	***Electrode pair spacing (mm)***
6.4	3.2	7.4	10.6	3

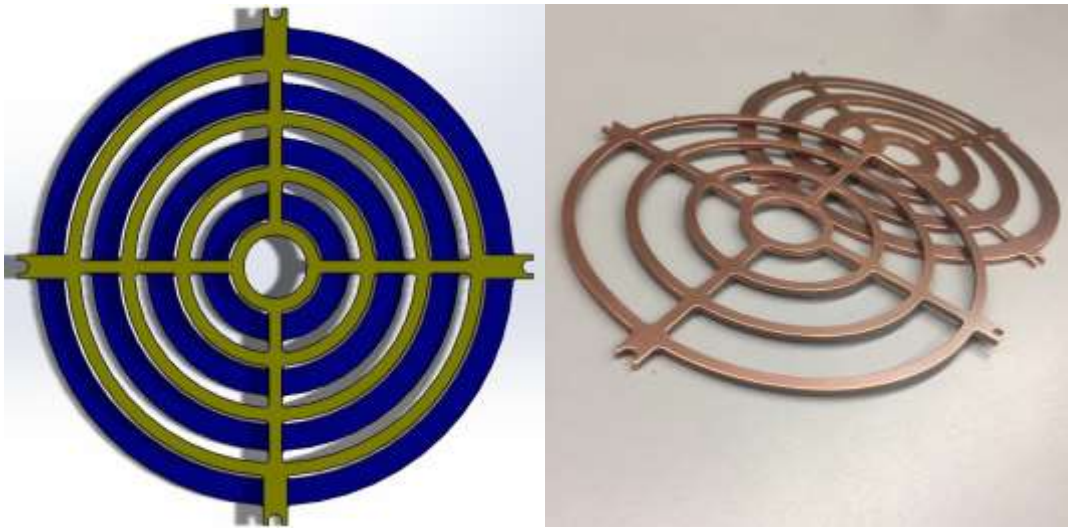

Figure 84: SolidWorks design and photograph of EHD pump electrodes

The electrodes were machined using CNC machines and were then deburred and put into a mass finisher to create smoother edges, preventing corona from happening during the experiment. The electrodes were held in place inside the tank by a four-piece insulating ring, which is shown in Figure 85. It was also 3D printed using a Mark 2 rapid prototype machine which is specifically used for creating the nylon infused with fiberglass material.

Figure 85: Photograph of the four-piece insulating ring

Corn oil was chosen to be used as the working fluid. The conductivity and permittivity values of corn oil were needed to be used as parameters in numerical analysis and were measured using a unique test cell, which is shown in Figure 86. The test cell consisted of an outer and an inner cylinder made out of steel attached to a Teflon™ piece. The test cell was filled with oil to the top edge of the inner cylinder and then a multimeter or a capacitance meter was attached to both the inner and outer cylinder of the test cell for resistance and capacitance measurement, which was then converted to conductivity and permittivity. The detailed description of the test cell and measurement procedure can be found in reference [112]. The properties of liquid corn oil used in the current numerical study are listed in Table IX.

Table IX: Properties of liquid corn oil used in the numerical analysis [113-115]

Physical Properties	Corn oil
Density [113]	919 kg/m^3
Viscosity [114]	37.92 mPa·s
Heat Capacity [114]	1673 J/kg·K
Thermal Conductivity [115]	0.165 W/m·K
Electrical Conductivity	3.51×10^{-11} S/m (±1%)
Electrical Permittivity	33.4×10^{-12} F/m (±1%)

Figure 86: Photograph of the test cell for conductivity and permittivity measurement

3.2.3 Experimental procedure

Two sets of experiments, experiment set 1 and experiment set 2, were conducted for temperature measurement at locations illustrated in Figure 83. The only difference between them was that the first set was performed with the RTD and top and bottom thermocouples at locations 2, 1 and 3, respectively, whereas for the second set, they were moved to locations 4, 5 and 6, respectively. For every experiment, the corn oil in the spherical reservoir was first heated by supplying 72 V voltage (corresponds to a power of 36W) to the cartridge heater for 300 seconds. The power and duration was specifically chosen so that total energy released by the heater would be able to heat up liquid in the upper hemisphere by 20 °C (temperature setting used in the numerical analysis). The heater was then turned off. For experiments with the EHD conduction pumping, the EHD pump was energized to and maintained at 9000 V for over an hour, until all temperature readings reached equilibrium. For experiments without EHD conduction pumping, all temperature data was recorded for more than 3 hours.

3.3 Theoretical model and numerical technique

The numerical model used in this study is a 2D axisymmetric one and is shown in Figure 87. Although it is a simplified representation of the electrodes and the spherical reservoir used for experimental study, it provides an insight of liquid mixing and thermal homogenization process with the activation of EHD conduction pumping and can be used for explaining the general trend of experimental results.

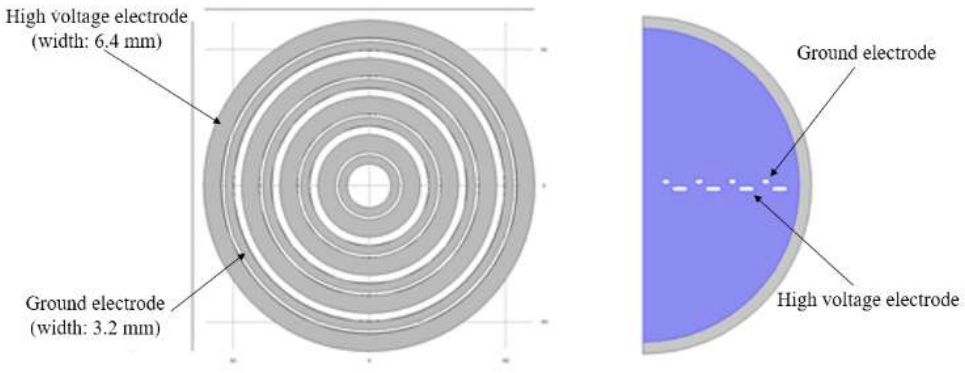

Figure 87: Schematic of asymmetric electrode configuration used in the numerical analysis: top view (left) and side view (right)

3.3.1 Assumptions

1) The numerical model is 2D axisymmetric
2) The reservoir is filled with only one kind of liquid, corn oil, the temperature in the upper and lower hemisphere are initially 313K and 293K, respectively.
3) The reservoir is thermally insulated from the surrounding environment.
4) Liquid flow is laminar.
5) Mobility and diffusion coefficients of positive and negative ions are the same.
6) The effects of gravity and Joule heating are not considered.
7) Charge injection is absent.

3.3.2 Governing equation and boundary conditions

EHD conduction pumping is modeled with the following equations of mass continuity, electrostatics, Navier-Stokes momentum rate conservation, charge conservation, and energy rate conservation:

$$\nabla \cdot \boldsymbol{u} = 0 \tag{34}$$

$$\boldsymbol{E} = -\nabla \phi \tag{35}$$

$$\nabla \cdot \boldsymbol{E} = (p-n)/\varepsilon \tag{36}$$

$$\rho \partial \boldsymbol{u}/\partial t + \rho(\boldsymbol{u} \cdot \nabla)\boldsymbol{u} - \mu \nabla^2 \boldsymbol{u} = -\nabla P + (p-n)\boldsymbol{E} + \rho \boldsymbol{g} \tag{37}$$

$$\partial p / \partial t + \nabla \cdot (b_+ p \boldsymbol{E}) + \nabla \cdot (p \boldsymbol{u}) - D_+ \nabla^2 p = k_d c - k_R p n \tag{38}$$

$$\partial n / \partial t + \nabla \cdot (b_- n \boldsymbol{E}) + \nabla \cdot (n \boldsymbol{u}) - D_- \nabla^2 n = k_d c - k_R p n \tag{39}$$

$$\rho c_p \, \partial T / \partial t + \rho c_p (\boldsymbol{u} \cdot \nabla T) = k \nabla^2 T \tag{40}$$

Where u, V, E, P and T are the velocity, electric potential, electric field, pressure and temperature respectively. c, p and n denote the concentration of neutral species, positive and negative charges, respectively. D_+ and D_- are diffusion coefficients of positive and negative charges, b_+ and b_- stand for ionic mobility of positive and negative charges. k_d and k_r are the dissociation and charge recombination coefficients, respectively. All the boundary conditions used for these equations are listed in Table X.

Table X: Summary of boundary Conditions

Equations	***HV electrode***	***Ground electrode***	***Reservoir inner wall***
Electrostatics	ϕ = 9000V	ϕ = 0	$\phi = 0$
Navier-Stokes	$\boldsymbol{u}$ = 0	$\boldsymbol{u}$ = 0	$\boldsymbol{u}$ = 0
Transport of charges	p = 0 $\mathbf{n} \cdot \nabla n$ = 0	n = 0 $\mathbf{n} \cdot \nabla p$ = 0	$\mathbf{n} \cdot \nabla n$ = 0 $\mathbf{n} \cdot \nabla p$ = 0
Heat transfer	-	-	$\mathbf{n} \cdot \nabla T$ = 0

3.3.3 Numerical technique

The transport equations were solved with COMSOL Multiphysics 5.2 using finite element scheme. The governing equations are discretized in cylindrical coordinates. The mesh for the simulation domain was generated using the automated Laminar Flow physics driven algorithm in the COMSOL Multiphysics software. The convergence criteria, $|y_{i+1}-y_i / y_i| < 10^{-4}$, is applied for all involved parameters.

3.4 Results and discussion

3.4.1 Experimental results

A. Experiment set 1 with and without EHD conduction pumping

For no EHD pumping experiment, temperatures in the locations of top thermocouple and the RTD in the center kept increasing after the heater power was turned off, as shown in Figure 88, due to transient heat conduction through the corn oil. After the temperatures reached their maximum, they deceased very slowly due to heat loss to the environment. In contrast, the temperature at the location of bottom thermocouple did not increase initially as it was far away from the heater, it started increasing slowly after 3000 seconds as a consequence of slow heat conduction process. It took more than 20000 seconds for the liquid in the reservoir to cool back down to its starting temperature.

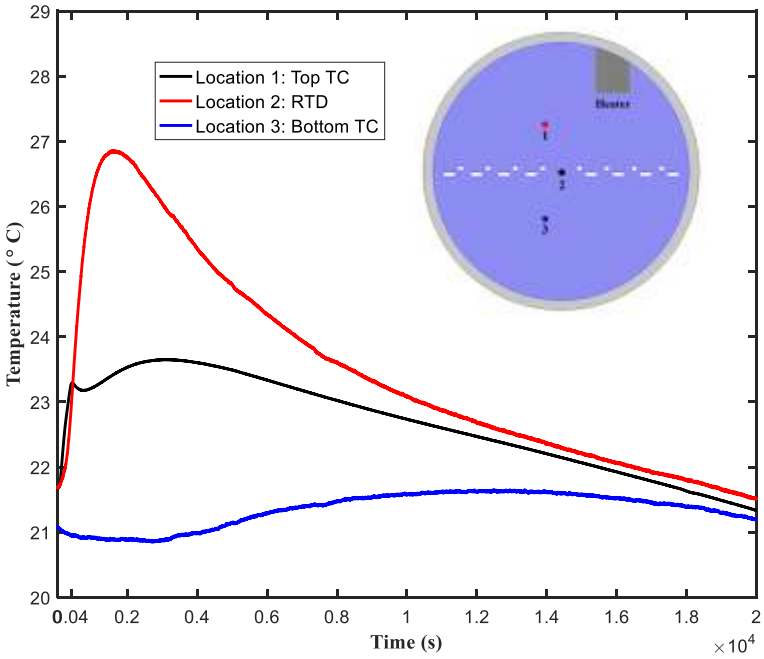

Figure 88: Temperatures in three locations of experiment set 1 without EHD conduction pumping

Temperature data for the experiment with EHD conduction pumping is shown in Figure 89, it is obvious that the activation of EHD conduction pump at the 400th second had a strong influence on the temperatures in three locations. The temperatures in the locations of top thermocouple and RTD in the center dropped rapidly over a full degree Celsius, which is due to a liquid mixing induced by EHD conduction pumping. This liquid mixing, on the other hand, immediately led to a temperature rise in the location of bottom thermocouple. Temperatures reached their maximum and became similar at around 2500 seconds, indicating that the liquid corn oil in the region of central axis of the spherical reservoir was fully mixed. The temperatures then decreased because of heat loss to the environment. This is similar to the observation in no-EHD pumping experiment. After 4000 seconds the EHD pump was turned off and a small temperature gradient in the tank began to emerge once again.

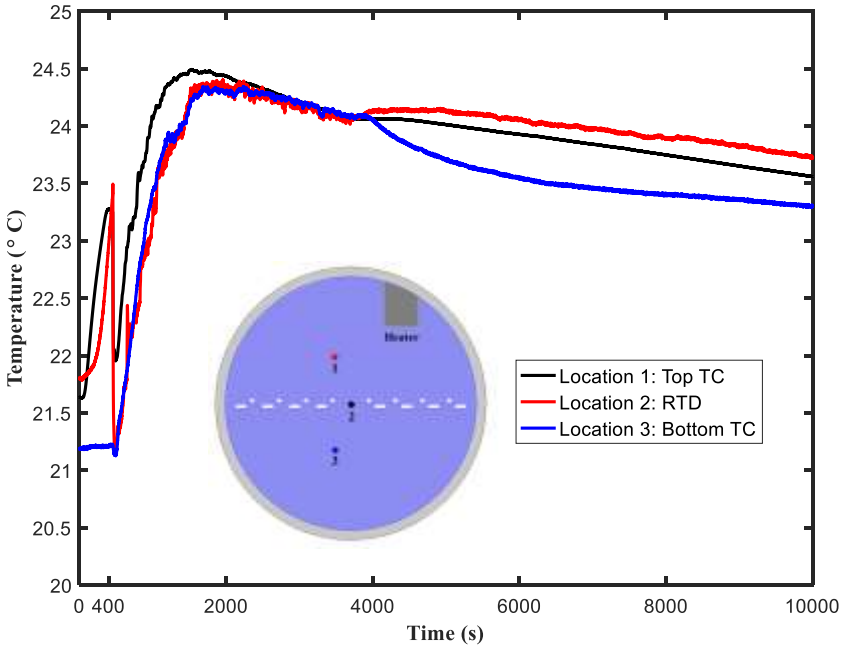

Figure 89: Temperatures in three locations of experiment 1 with EHD conduction pumping

B. Experiment set 2 with and without EHD conduction pumping

For no EHD pumping experiment, after the power supply to the heater was turned on, temperature in the location of top thermocouple measured by the RTD rose by 47 °C dramatically, as shown in Figure 90, due to the fact that this area was very close to the heater. It then dropped exponentially due to heat dissipation to the environment. The temperature measured by the top thermocouple close to reservoir wall did not change initially and but then increased gradually to its maximum. The temperature at the bottom of the reservoir had almost no change the entire experiment. Eventually, after about 20000 seconds, all three temperatures had reached their initial values.

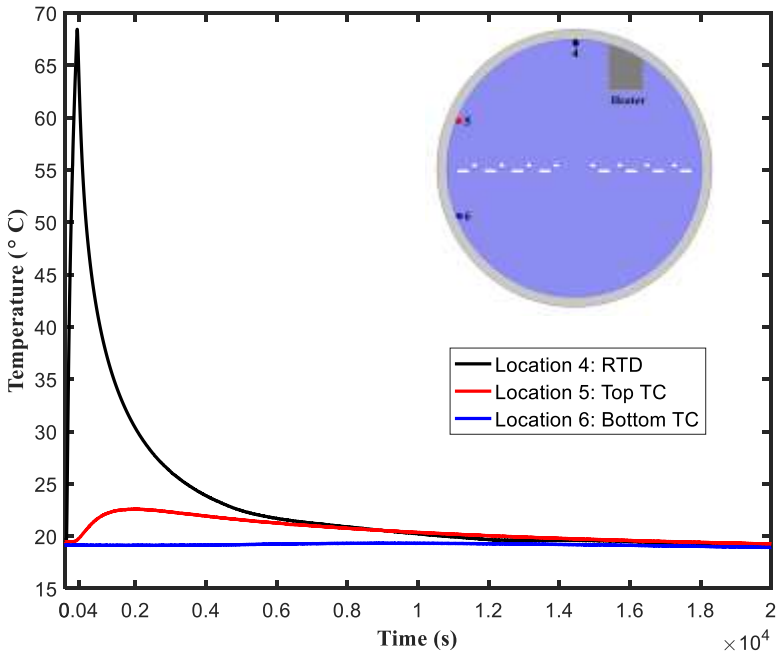

Figure 90: Temperatures in three locations of experiment set 2 without EHD conduction pumping

With the activation of EHD conduction pumping, the drop of the RTD's temperature was more abrupt and faded more erratically as it got close to the equilibrium temperature, which is shown in Figure 91. The temperature at the top thermocouple dropped down to match the bottom thermocouple in less than 500 seconds after the EHD conduction pumping was activated. At about 4000 seconds, or 66 minutes, all three temperatures were all within 0.1°C of each other, indicating the tank was fully mixed.

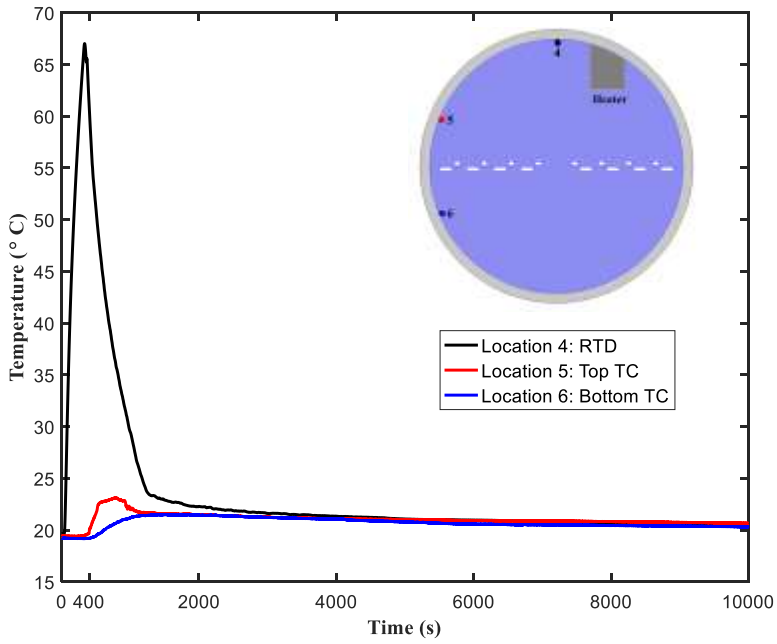

Figure 91: Temperatures in three locations of experiment set 2 with EHD conduction pumping

C. Individual comparison

The comparison of temperatures at various locations with and without EHD pumping are shown in Figures 92-97, respectively. These graphs display the effects of the EHD much more effectively than the previous ones. The black line and gray line represent the change in temperature monitored for experiments with and without the activation of EHD conduction pumping, respectively.

Comparison of temperature at location 1 is shown in Figure 92; it can easily be seen that the EHD pump was turned on around 400 seconds. At this point, the temperature drops rapidly before it starts to increase again. With EHD pumping, maximum temperature was slightly above 24 °C. Without EHD pumping, it climbs to a temperature slightly below 27°C. The leveling off of temperature at around 2000 seconds indicates the liquid corn oil in the region of central axis of the spherical reservoir was fully mixed. It can be seen that the two temperature curves crossed at

around 7000 seconds, the main reason is that fluid circulation and heat transfer induced by EHD pumping helped maintain the temperature.

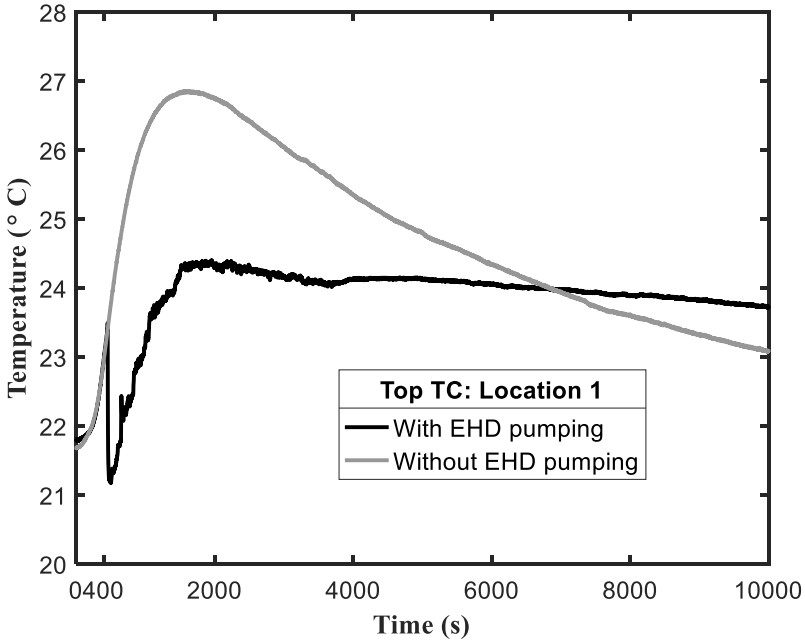

Figure 92: Temperature at location 1 measured with top thermocouple

Comparison of temperature at location 5 is shown in Figure 93, the temperature trend for the trial without EHD pumping is very similar to its counterpart in Figure 92 except that the maximum temperature is lower and happened later as point 5 was further away from the heater than point 1, it is a natural result of transient heat conduction. For EHD pumping case, after the activation of EHD pumping at around 400 seconds, the temperature increased rapidly. This is because that the downward flow along reservoir wall (shown in Figure 101), induced by the EHD conduction pumping, brought the heat accumulated at the top of reservoir.

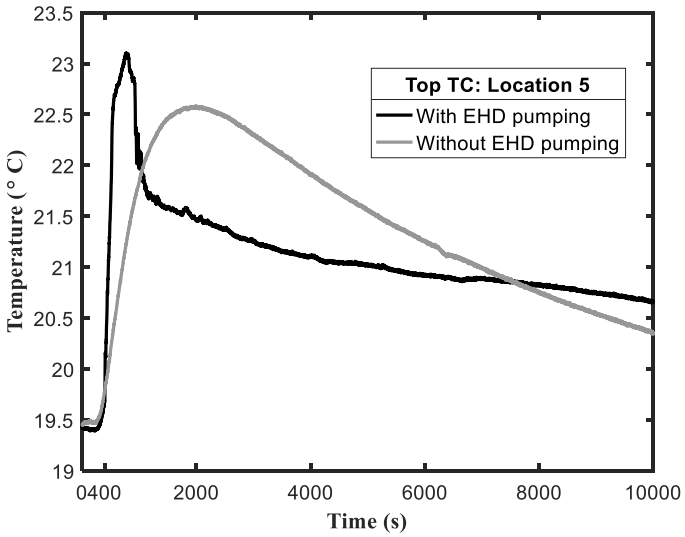

Figure 93: Temperature at location 5 measured with top thermocouple

Figure 94 shows the temperature comparison at location 2 measured with RTD. As with Figure 92, at 400 seconds when the EHD high voltage is turned on, the black line displaying the EHD data immediately spikes downwards and then begins to progress upwards to slightly above 24°C at 1500 seconds where it becomes the same as both the thermocouples in the experiment. When there is no EHD pumping, the temperature rises about 1.5 °C and then begins to regress back to where it started.

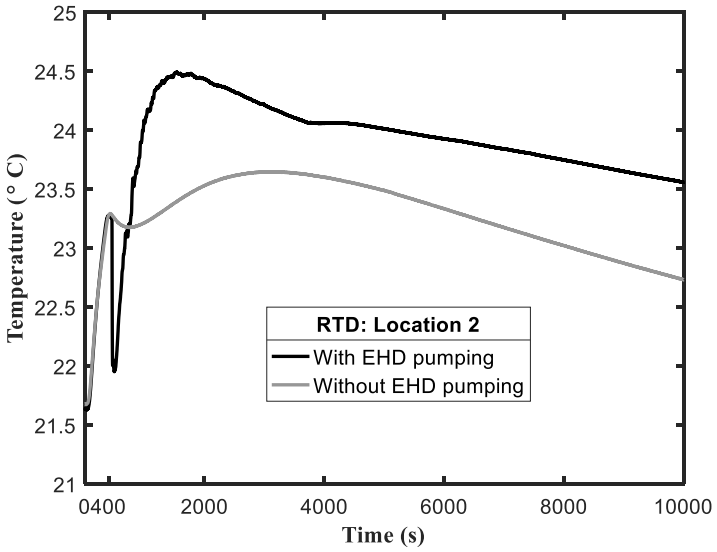

Figure 94: Temperature at location 2 measured with RTD

As shown in Figure 95, the temperature at location 4 measured with RTD is significantly higher than temperature measurement elsewhere since locations 4 is closest to the heater. As seen in the graph, the temperature quickly reaches approximately 68 °C right before the heater is turned off in both the EHD and no EHD trials. The difference between the two trials is that the temperature of the RTD in the EHD trial rapidly drops due to EHD mixing compared to the exponential decline in temperature of the no EHD trial.

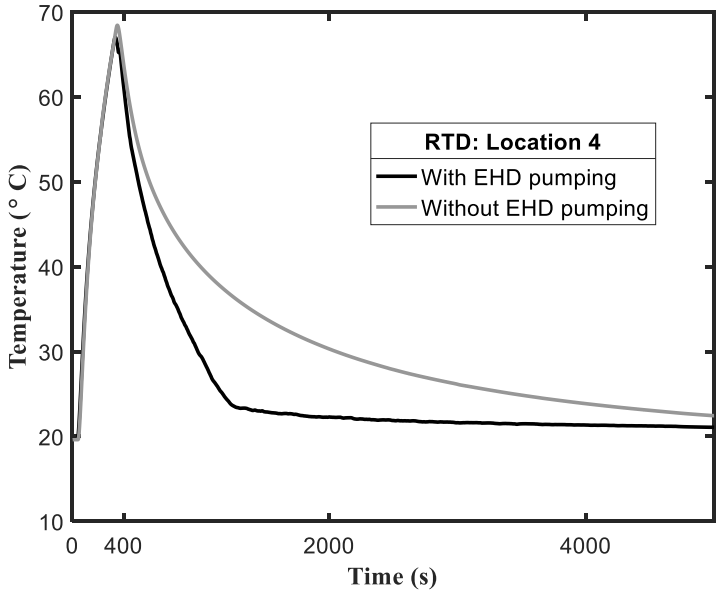

Figure 95:Temperature at location 4 measured with RTD

Figure 96 and 97 shows the comparison of temperature measured with bottom thermocouple at location 3 and location 6, respectively. Temperature trend at these two locations were similar. The black line displaying the EHD data shows that the temperatures increase when the EHD voltage is turned on at around 400 seconds. For the experiment without EHD pumping, temperature remained almost unaffected until around 4000 seconds when natural convection reaches the bottom of the tank.

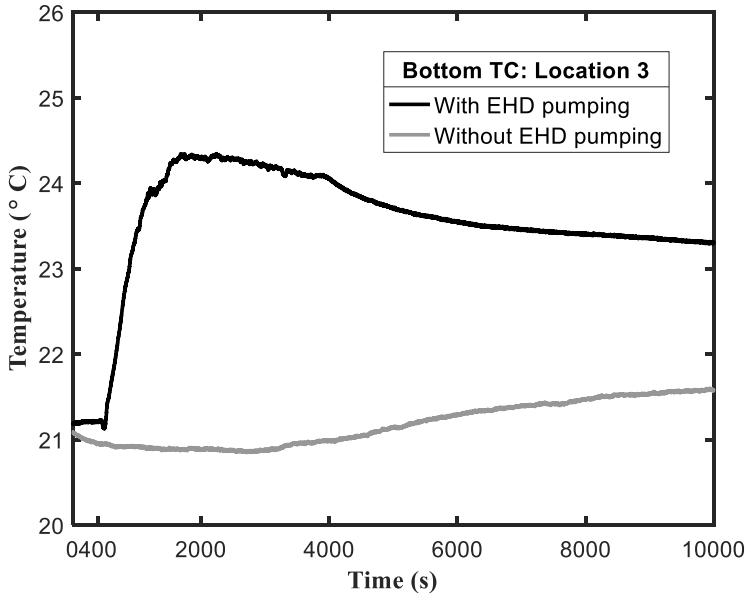

Figure 96: Temperature at location 3 measured with bottom thermocouple

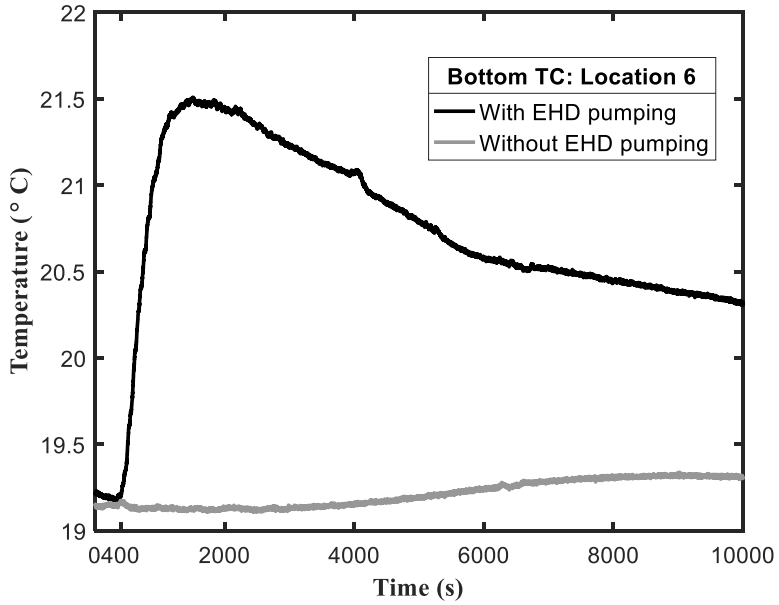

Figure 97: Temperature at location 6 measured with bottom thermocouple

3.4.2 Numerical results

It should be pointed out that the numerical solutions in this study are based on a 2D axisymmetric model and a totally different initial temperature profile than the experimental one; thus, they do not correspond to the experimental data. However, the numerical solutions provide

fundamental understanding of the physics behind the problem in hand. The comparison between experimental data and exact numerical simulation is beyond the scope of this study. The results presented in this section illustrate the mixing mechanism and thermal homogenization process with EHD conduction pumping.

As shown in Figure 98, a high intensity electric field exists in the inter-electrode region, which is because of the closeness of the two electrodes surfaces. On the other hand, the majority of the interior of the spherical reservoir is characterized by substantially lower electric field, indicating that the electric field enhanced charge dissociation and electric conduction is confined mainly to the inter-electrode region close to the central plane of the reservoir.

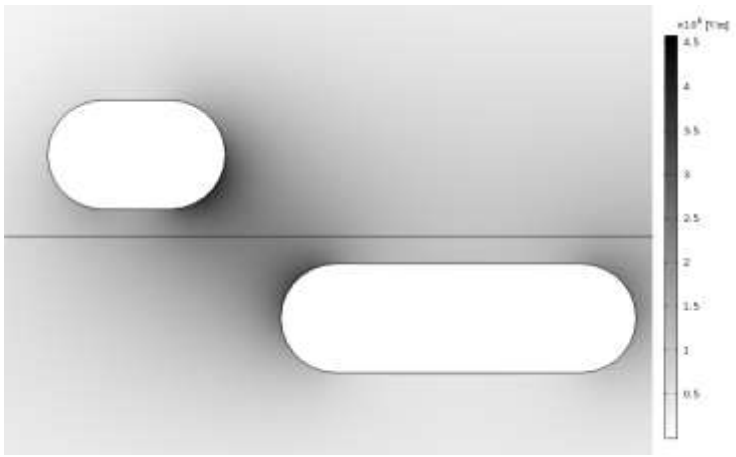

Figure 98: Electric field in the vicinity of electrodes close to the vertical center line of the reservoir

The steady state net charge concentration (positive charge concentration minus negative charge concentration) in the vicinity of electrodes close to the vertical center line of the reservoir is illustrated in Figure 99. The attraction of electric charges to the electrodes leads to the formation of heterocharge layers.

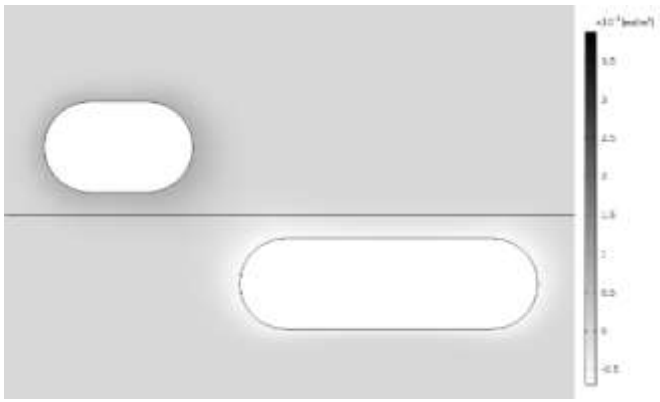

Figure 99: Steady state net charge concentration in the vicinity of electrodes close to the vertical center line of the reservoir

As shown in Figure 100, the majority of the Coulomb force is within the inter-electrode region, as a result of the high intensity electric field and net charge density in this region. The asymmetry of the electrodes, however, results in a flow out of the inter-electrode region as compared to the flow recirculation inside the inter-electrode region with symmetric electrode design [111].

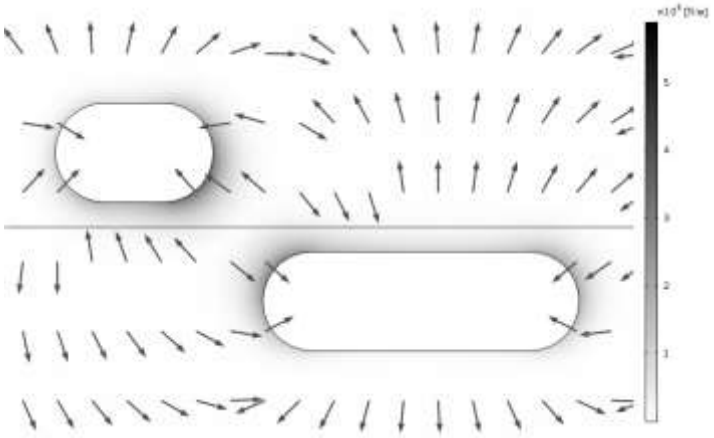

Figure 100: Steady state Coulomb force in the vicinity of electrodes close to the vertical center line of the reservoir

The contours of velocity magnitude embedded by the velocity stream traces are displayed in Figure 101. It shows that the velocities in the region close to the electrodes and central axis of

the reservoir are significantly higher than those elsewhere. The upward flow along central axis in the upper hemisphere of spherical reservoir accompanied by the downward motion along central axis in the lower hemisphere.

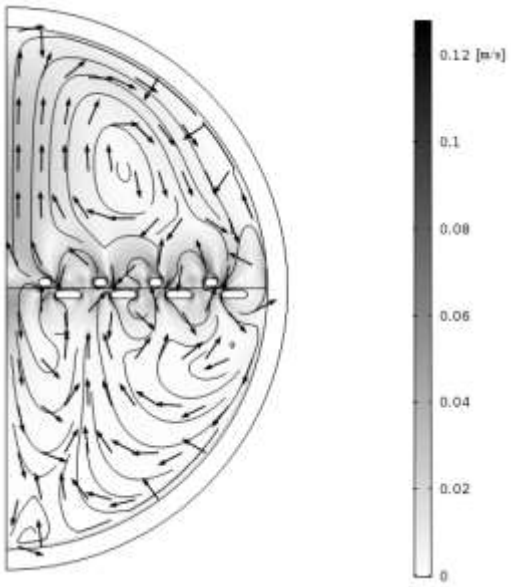

Figure 101: Steady state flow field

Time evolution of temperature distribution at two intermediate time steps, 0 second and 20 second, is presented in Figure 102. At *t*=0 s, fluid temperature in the upper and lower hemispheres are 313 K and 293 K, respectively. Please note that this temperature distribution is a simplified representation. For the actual experiment, the temperature was not uniformly distributed especially in the upper hemisphere as heat conduction was the only heat transfer mechanism for the heating process. At *t*=20s, working fluid close to the central axis region of the reservoir is well mixed, which is manifested with the uniform temperature distribution in this region. As previously mentioned, thermal homogenization in this region is achieved with the upward flow along central axis in the upper hemisphere of spherical reservoir and the downward motion along central axis in the lower hemisphere.

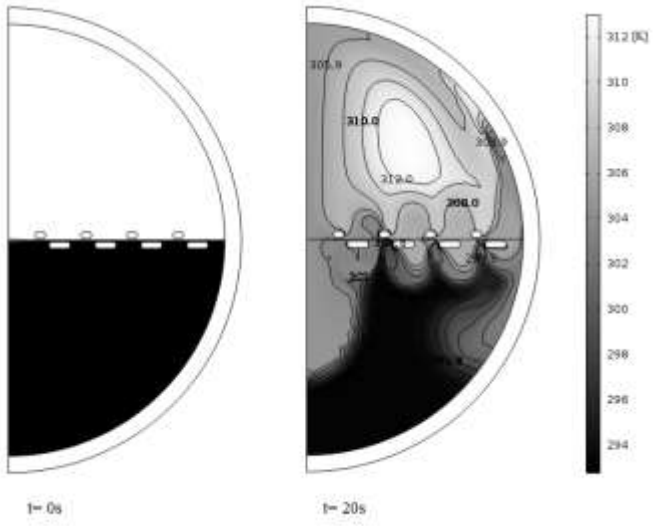

Figure 102: Temperature distribution at two intermediate time steps, 0s and 20s.

3.5 Conclusions

The effect of EHD conduction mechanism on thermally homogenizing a fluid with a temperature jump in a spherical reservoir was experimentally and numerically studied. The proposed asymmetric electrode design was especially effective for reservoirs with large diameters given the fact that the resultant electric body forces penetrate into the interior of working fluid. Temperatures at six locations in a spherical reservoir were measured and compared with temperature evolution results derived from a simplified numerical model. The numerical results of electrical field, space charge distribution, Coulomb force density, and steady state liquid flow velocity distribution were also presented to illustrate the liquid mixing and thermal homogenization process. Both experimental and numerical results confirmed that EHD conduction mechanism can be utilized to effectively circulate and mix a thermally non-homogenous liquid inside a reservoir and thus, should be an attractive alternative to current methods of mixing fluids within a storage tank in space application.

CHAPTER 4 EXPERIMENTAL STUDY OF POOL BOILING HEAT TRANSFER ENHANCEMENT WITH ENHANCED SURFACES AND THE EFFECT OF SURFACE ROUGHNESS AND ORIENTATION ON POOL BOILING

4.1 Introduction

As a very effective heat transfer mechanism that can provide a large heat transfer rate, the nucleate boiling of a pool of liquid has been a subject of intensive research for several decades. However, pool boiling on a bare surface is still not sufficient to meet thermal management requirement for many applications such as high-heat-flux microelectronics and power electronics, where performance is highly sensitive to core temperatures, and with need to be further miniaturized. Despite the ongoing research, which is briefly describe in the introduction section, the application of nano-textured surfaces in pool boiling heat transfer enhancement merit further investigation from the viewpoint of improvement and flexibility of usage and cost effectiveness. In addition, more research needs to be carried out to fundamentally understand the mechanisms of various parameters on pool boiling.

The nucleate boiling heat transfer coefficient (HTC) is an indicator of the heat removal rate. The higher it is, the smaller temperature difference between liquid saturation temperature and surface temperature in boiling fluid will be, for a given heat flux. Therefore, increasing the nucleate boiling heat transfer coefficient in two-phase cooling systems is a promising method to improve performance of high-heat-flux devices. On the other hand, pool boiling heat transfer is severely diminished at CHF condition, which represents the limit of pool boiling. In this study, nucleate pool boiling was experimentally studied at ambient temperature on various modified surfaces including surfaces with electroplated polymer nanofiber coatings with refrigerant R-123 as working fluid. The associated pool boiling heat transfer enhancement is characterized in terms of

nucleate boiling HTC and CHF. Moreover, the effect of boiling surface roughness and orientation on nucleate boiling HTC and CHF are also examined and compared with predictions based on Rohsenow's and Cooper's correlation.

4.2 Experimental setups and procedure

4.2.1 Experimental setup 1 and 2

Two test facilities were developed for the experimental study of pool boiling heat transfer enhancement. Experimental setup 1 was used for samples with nanofiber mats and experimental setup 2 was used for 1 micron surface, 10 micron surface and several specifically machined surfaces. Due to their similarity, the schematics of both test facilities and photographs of both test chambers are shown together in Figure 103 and Figure 104, respectively. Under normal operation, the test facilities were partially filled with refrigerant R-123. Liquid R-123 was drawn out of the bottom of the test chambers and passed through a condenser supplied with chilled water by a chiller in order to maintain a constant saturation pressure and temperature in the test chambers. Two needle valves, one fitted across the pump and the other fitted on the liquid return line from the pump to the test chamber allowed for the flow rate to be controlled. A variable frequency drive also provided flow rate control by varying the speed of the 3-phase AC motor that drives the pump. Large transparent tube glass and flat glass were installed as part of the test chambers for observation and visualization with high speed camera of the pool boiling phenomenon. PTFE gaskets were used to provide a hermetic seal between the aluminum or stainless steel and the glass. Four threaded rods or eight bolts running parallel to test chamber were used to provide clamping force of the hermetic seal.

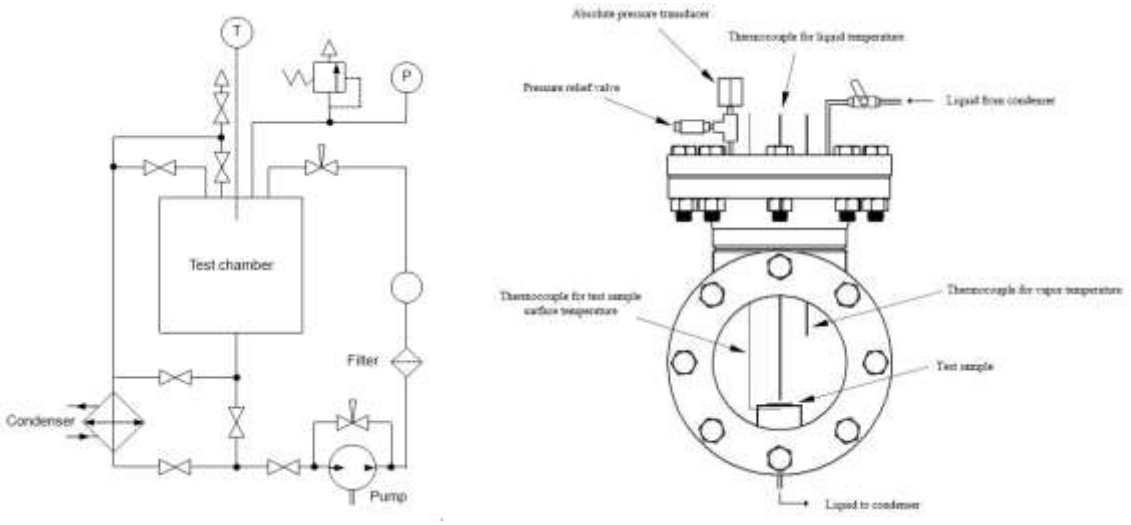

Figure 103: Schematics of experimental setup 1 (left) and 2 (right)

Figure 104:Photographs of test chamber 1 (left) and 2 (right)

The absolute pressure inside the test chambers was monitored using a VALIDYNE AP-10-42 or a VALIDYNE P55 pressure transducer. Analog pressure gauges were also installed as backup gauges for safety reasons. The test chambers were also fitted with pressure relief valves that were set to open at approximately 70 kPa of positive differential pressure, which is well below the maximum operating pressure of the glass cylinder (which had the lowest pressure rating among

all the components) but well above the normal operating pressure of the experiment. The pressure was used to calculate the corresponding saturation temperature, which was then compared with the liquid temperature measured by T-type thermocouple. The working fluid was refrigerant R-123 for all the experiments and its properties are listed in Table 2.

The experiment was designed to allow for safe determination of the critical heat flux point, which is marked by a rapid temperature rise on the pool boiling surface. However, at this point the heat transfer also experiences a sudden and drastic loss of performance. This critical point corresponds to the inability of fresh liquid to reach the heated surface, with its movement inhibited by the rapid and repeated departure of large vapor bubbles from the surface. Consequently, the heated surface becomes blanketed in a vapor and the surface temperature can rise rapidly due to the sudden reduction in heat transfer. To accomplish this, programmable power supplies were used to supply voltage to the heaters, and they were controlled by the output of the USB-6211 data acquisition system. When the temperature of the heaters exceed a threshold temperature of 50 °C, a LabVIEW program immediately switches off the power supply, cutting the power to the heater. Power to the heaters remains off even after the temperature of heaters and rate of change of temperature have returned to an acceptable level. As an additional safety feature, power to the heater is also cut if the absolute pressure of the test chambers rises above 200 kPa. The Maximum systematic error of various measurement devices and experimental uncertainty are given in Table XI.

Table XI: Maximum systematic error of various measurement devices and experimental uncertainty for chapter 4

Measurement	Maximum systematic error
Temperature (RTD)	0.15°C
Temperature (Thermocouple)	0.5°C
Voltage of heater Power Supply	±0.6 V
Derived quantity	**Maximum Uncertainty**
Heater Power, Q	±1%
Heat Flux, q''	±1%
Heat transfer coefficient, h	±11.4%

4.2.2 Bare surface, surfaces with nanofiber mats, and heaters used in test facility 1

The test samples used in test facility 1 were made with 25.4 mm × 25.4 mm square pieces of 96% alumina ceramic substrate. The thickness of this substrate was 1 mm and two types of nanofiber mats (made with fast and slow copper-plating process) were electrospun onto the top surfaces of test samples using equipment and procedures discussed in the next section. The top bare surface of a sample with no nanofiber mat electrospun, was used as a reference surface for comparison. Photograph of bare surface and nano-textured surfaces is shown in Figure 105.

Figure 105: Photograph of the top surfaces of test samples; left (fast copper-plated nano-textured surface) middle (bare surface) and right (slow copper-plated nano-textured surface)

A solid 25 Ω, 22.86 mm × 22.86 mm resistor was centrally printed onto the bottom surface of the substrate to form an electrically resistive heating element. PdAg bus-lines ran along each side of the resistor to ensure an approximately uniform current flow (hence a uniform heat flux from Joule heating) throughout the resistor and to facilitate the soldering of connecting wires. A photograph of the bottom surface of a test sample is shown in Figure 106.

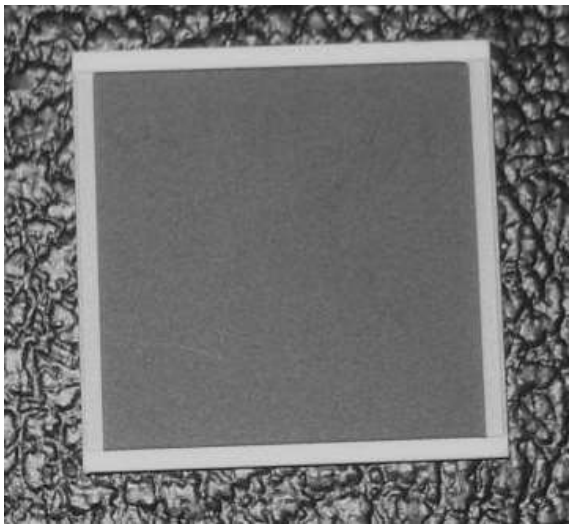

Figure 106: Photograph of the bottom surface of a test sample

100 Ω platinum RTDs was cemented to the back of the heaters and their resistance were measured for pool boiling surface temperature measurement using a data acquisition system. RTD connections were made using the four-wire method, which allows the resistance of the leads to be excluded from the resistance measurement, thereby improves accuracy.

The Materials used for the preparation of nanofiber mats are as follows: Polyacylonitrile (PAN, Mw = 150 kDa) obtained from Polymer Inc., N-Dimethylformamide (DMF) anhydrous 99.8%, sulfuric acid, hydrochloric acid, copper sulfate, and formaldehyde obtained from Sigma-Aldrich, and Ethanol (100%) obtained from Dacon Laboratories Inc..

A standard electrospinning setup [116-118] was used to prepare PAN nanofiber mats. Fibers were elecrospun for 2 min onto the top surface of a substrate producing nanofiber mat of

thickness ~30 μm. During electrospinning the solution flow of 1.0 ml/h was sustained, and the process was conducted at the electric field strength of 1.1 kV/cm. After collecting the electrospun mat on the substrate surface, DI water was dripped onto the nanofibers to wet the whole surface. Then, the mat was left in open atmosphere to dry up the wet PAN nanofibers prior to further treatment.

The electric conductivity of the polymer nanofiber mats is insufficient to be used as an electrode in the electroplating process. The procedure described in [119] was used for electroplating nanofibers. In brief, nanofiber mats were sputter-coated with Pt/Pd to a thickness of 15 nm by using a 120 Cressington sputter controller. Then, the sputter-coated nanofiber mats were immersed in the copper plating solution which consisted of sulfuric acid (5 g), hydrochloric acid (0.5 g), copper sulfate (16 g), formaldehyde (10 g), and DI water (100 ml). The sputter-coated PAN nanofibers were used as a cathode immersed into the electroplating bath. A bare copper substrate served as an anode. A laboratory electroplating station HSEPS-10 with a cathode stand was used to electroplate nanofiber mats. For electroplating the electrospun polymer nanofiber mats, two different electric current density were used: 50-100 mA/cm^2 (to be termed as slow process) and 150-250 mA/cm^2 (to be termed as fast process) for 1.5 min. Then the copper-plated nanofiber mats were extracted from the electroplating bath and submerged in 10% formaldehyde for 5 min. After that they were rinsed with DI water and dried. SEM images of the copper-plated PAN nanofiber mats are shown with zoomed out view in Figure 107 and with zoomed in view in Figure 108. Figure 108 clearly shows the nanostructured surfaces on top of a single nanofiber.

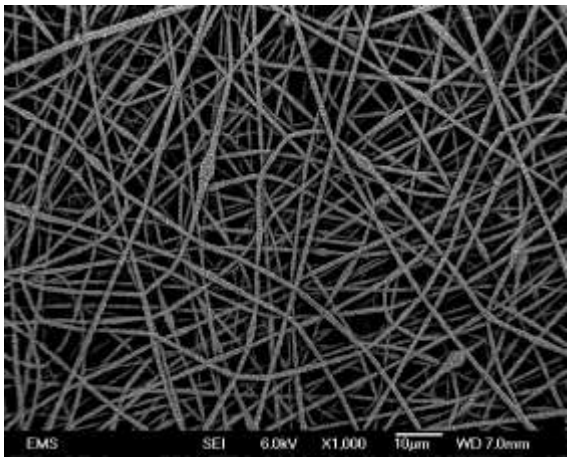

Figure 107: SEM image of Copper-plating of PAN nanofiber mats (zoomed out view).

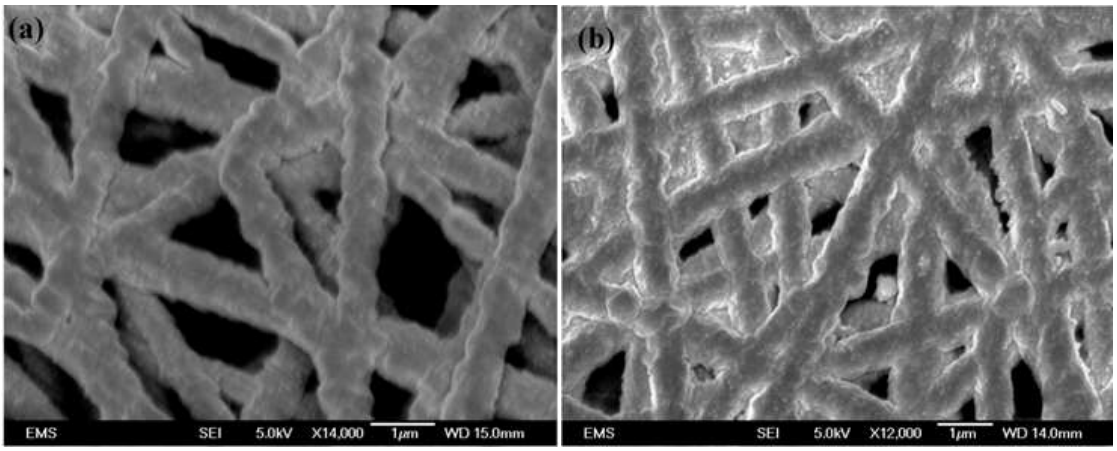

Figure 108: SEM images showing zoomed in view of nano-texture of copper-plating of PAN nanofiber mats (a) fast process, (b) slow process

4.2.3 Specifically machined surfaces and heaters used in test facility 2

Photographs of the specifically machined test samples are shown in Figure 109. The heaters for pool boiling used in test facility 2 were 32-gage resistance wires (with a resistance of 34Ω/m at 25°C) wrapped around cylindrical copper pieces which had a thermal conductivity of 390W/m·K. The resistance wire had a thin layer of Polyimide electrical insulation and the outer diameter of the wire (including the insulation layer) was 0.241 mm. The cylindrical copper pieces are 0.375 inch in diameter and the top surfaces were soldered to the test samples. Holes with a depth of 5.0 mm and 2mm away from sample surface was drilled into the side of the test samples.

36-gage T-Type wire thermocouples were inserted in the holes and then soldered for temperature measurement of pool boiling surface.

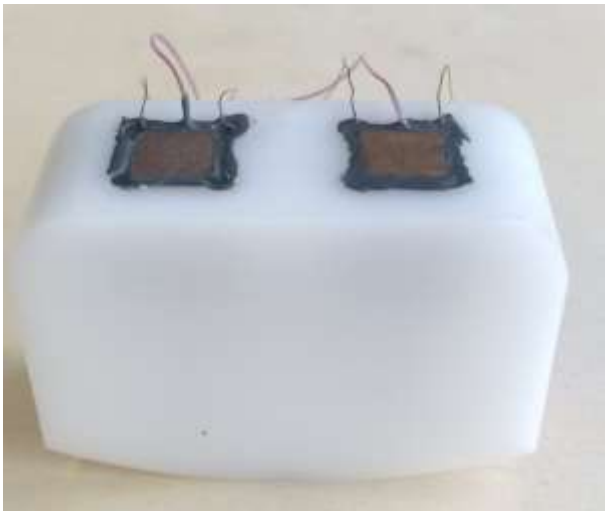

Figure 109: Photograph of test sample surfaces: left (10 μm surface), right (1 μm surface).

4.2.4 Test modules in test facilities 1 and 2

PTFE and acetal resin thermal insulator blocks were installed at the bottom of test chamber 1 and 2, respectively. Test samples were installed onto these mounting blocks, epoxy and screws were applied and used to ensure that working fluid would not infiltrate into the gap between the test samples and the mounting blocks. The thermal conductivity of PTFE and acetal resin are 0.25 W/m·K and 0.33 W/m·K, respectively. Heat loss from heaters to both thermal insulator blocks were estimated to be less than 5% at the maximum heat load. Photographs of both test modules at the bottom of test chambers are shown in Figure 110.

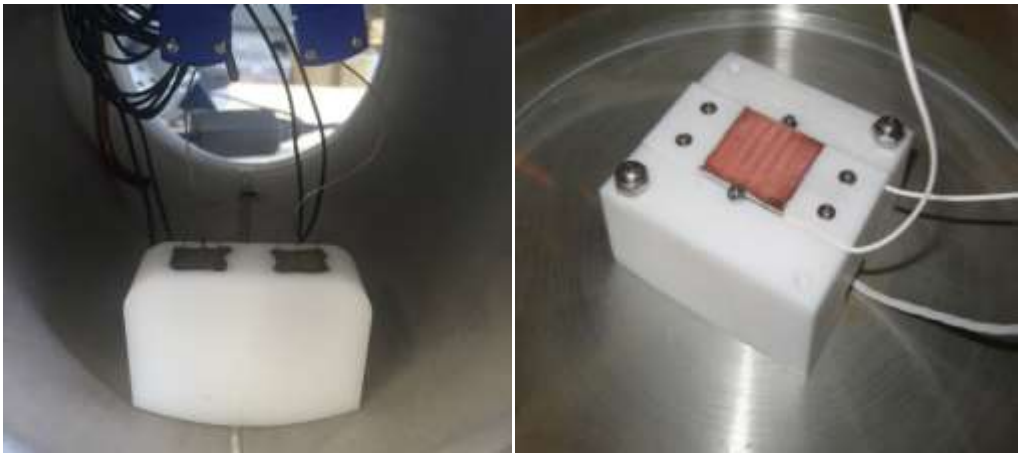

Figure 110: Photographs of both test modules installed at the bottom of the test chambers

4.2.5 Experimental Procedure

Once the test modules were installed in the test chambers and the flanges was fitted, a vacuum pump was used to evacuate the chambers to a vacuum level of at most 500 mTorr. The vacuum pump was then isolated from the system and HCFC-123 was allowed to enter through a filter-drier into the test chambers until the surface of the heaters were submerged by at least 2 cm of liquid refrigerant. Power was then applied to the heaters in small increments starting from zero, and at each power setting the temperature was allowed to reach steady state before recording the data. The heater power was gradually increased until the critical heat flux level was reached. At this point, the heater was shutdown automatically by LabVIEW program and data acquisition board.

As all the experiments were performed at room temperature, the heat leakage from the test facilities to environment was assumed to be negligible. The wall superheat was evaluated as the difference between the wall temperature T_{wall} and the liquid saturation temperature. As the thermal conductivity of the PTFE and acetal resin block under heaters is very low, heat generated by the heaters is assumed to be completely transferred to the refrigerant pool during the experiment. Pool boiling heat flux and heat transfer coefficient are calculated as follows:

$$q'' = \frac{U^2}{RS} \tag{41}$$

$$h = \frac{q''}{\Delta T} \tag{42}$$

where U is the applied voltage, R is the resistance of the heater, S is the surface area of the heater, and ΔT is wall superheat.

4.3 Experimental results and discussion

4.3.1 Effect of surface roughness on pool boiling heat transfer

The pool boiling data obtained with 1 μm surface roughness, along with its regression analysis using the method of least squares, is shown in Figure 111. The curve fit of the current experimental data indicates that wall superheat ΔT is proportional to the $q''^{0.298}$. It is similar to the coefficient m (0.33) used in the semi-empirical Rohsenow correlation, which is shown in equation 20.

As was mentioned in the introduction section, several researchers had proposed correlations of pool boiling heat transfer coefficient h and surface roughness, in which h is proportional to q''^{n}. For current experimental data obtained with 1 μm surface roughness, n is determined to be 0.67 based on the curve fit of experimental data, which is shown in Figure 112, it is the same as the value of n used in Cooper's correlation:

$$h = C(Pr^{0.12-0.2\log_{10}Rp})(-\log_{10}Pr)^{-0.55}M^{-0.5}q''^{0.67} \tag{44}$$

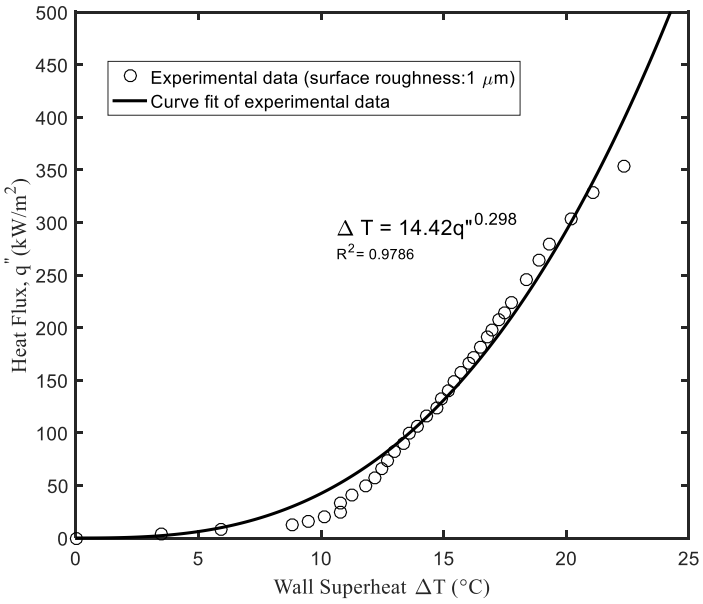

Figure 111: Pool boiling data obtained with 1 μm surface roughness and its curve fit using the method of least squares

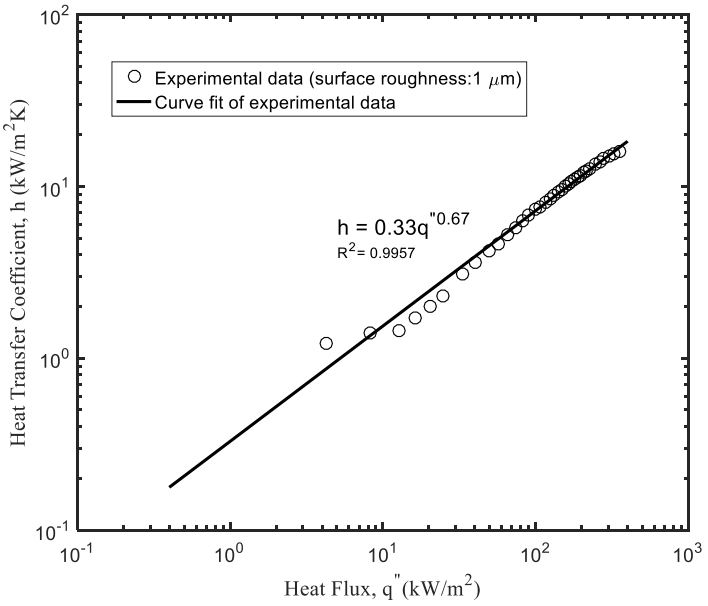

Figure 112: Relation between pool boiling heat transfer coefficient and heat flux based on curve fit of experimental data using the method of least squares

Comparison of pool boiling curves between 1 micron and 10 micron surfaces for horizontal surface orientations, along with Rohsenow correlation is shown in Figure 113. It can be seen that the pool boiling heat transfer coefficients on 10 micron surface are significantly higher than those of the 1 micron surface after the pool boiling starts and the critical heat flux for 10 micron surface is slightly higher than that of 1 micron surface. The values of C_{sf} in the Rohsenow correlation were obtained with the curve fit of experimental data of Saiz Jabardo et al. [49], and they are 0.0049 and 0.003 for 1 micron and 10 micron surface, respectively. The current experimental data lie in between the correlations.

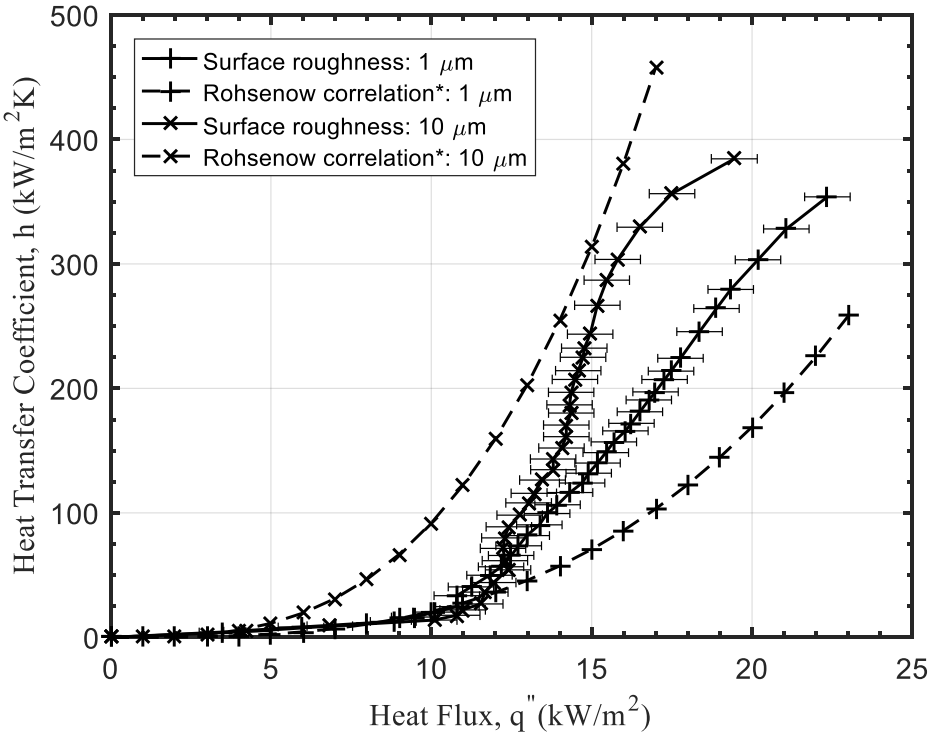

Figure 113: Comparison of pool boiling curves for 1 μm and 10 μm horizontal surface

Higher pool boiling heat transfer coefficients of 10 μm surface can be attributed to higher density and larger range of small cavities acting as active nucleation sites during pool boiling compared with 1 μm surface. Based on Hsu [120], the sizes of active nucleation sites during pool boiling range from 50 nm to 10 microns. Photographs of nucleate pool boiling taken for both

surfaces, shown in Figure 114, confirmed that for a given applied heat flux, low, moderate or high, the number of bubbles activated on 10 μm surface were much more than those on 1μm surface.

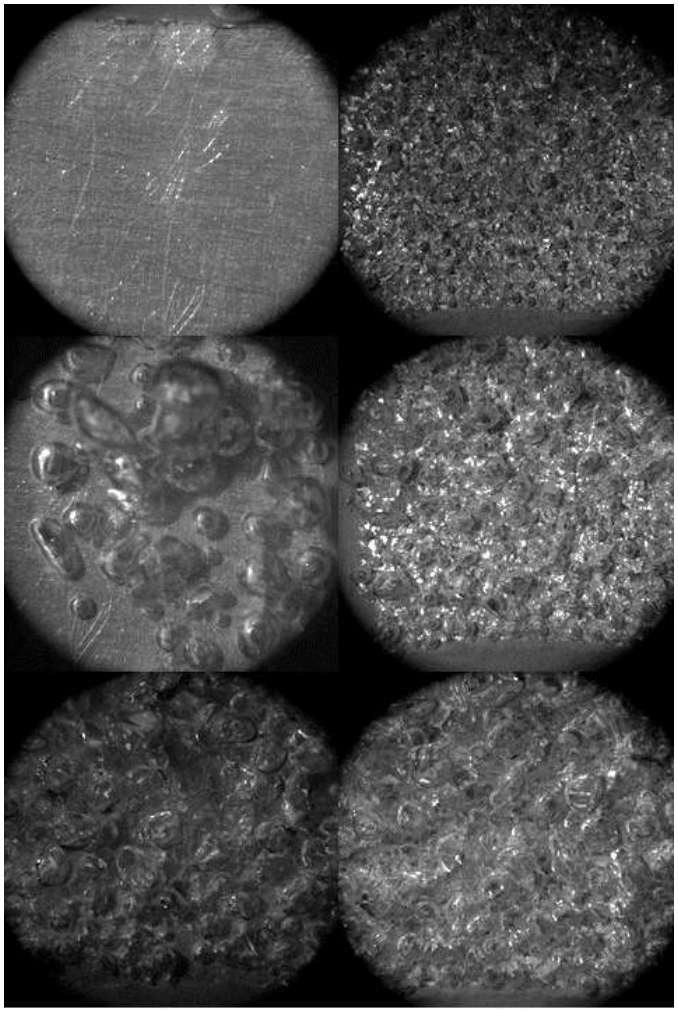

Pool boiling at low heat flux, q" = 1W/cm^2: 1 μm surface (top left), 10 μm surface (top right)

Pool boiling at moderate heat flux, q'' = 5W/cm^2: 1 μm surface (middle left), 10 μm surface (middle right)

Pool boiling at high heat flux, q'' = 15W/cm^2: 1 μm surface (bottom left), 10 μm surface (bottom right)

Figure 114: Photographs of pool boiling obtained during the experiment for both 1μm and 10μm vertical surface

4.3.2 Effect of surface inclination angle on pool boiling heat transfer

Figure 115 shows the nucleate boiling curves obtained with 1 micron surface at 0°, 45º and 90º surface inclination angles and their comparison with Rohsenow correlation with coefficient

C_{sf} determined with Jung's correlation, in which the dependence of C_{sf} and m on the surface inclination angel θ is expressed by:

$$C_{sf} = 7.218\times10^{-3} - 1.74\times10^{-6}\theta \quad (45)$$

$$m = 0.256 - 1.514\times10^{-4}\theta + 1.778\times10^{-5}\theta^2 - 7.16\times10^{-8}\theta^3 \quad (46)$$

Pool boiling on horizontal surface showed higher heat transfer coefficients than 45 degree inclined and vertical surfaces at low applied heat flux. However, the difference decreases as heat flux increases and the pool boiling heat transfer coefficients tend to be similar at higher applied heat flux. It is obvious that the CHF decreases as the inclination angle increases, this trend is the same as that of correlation.

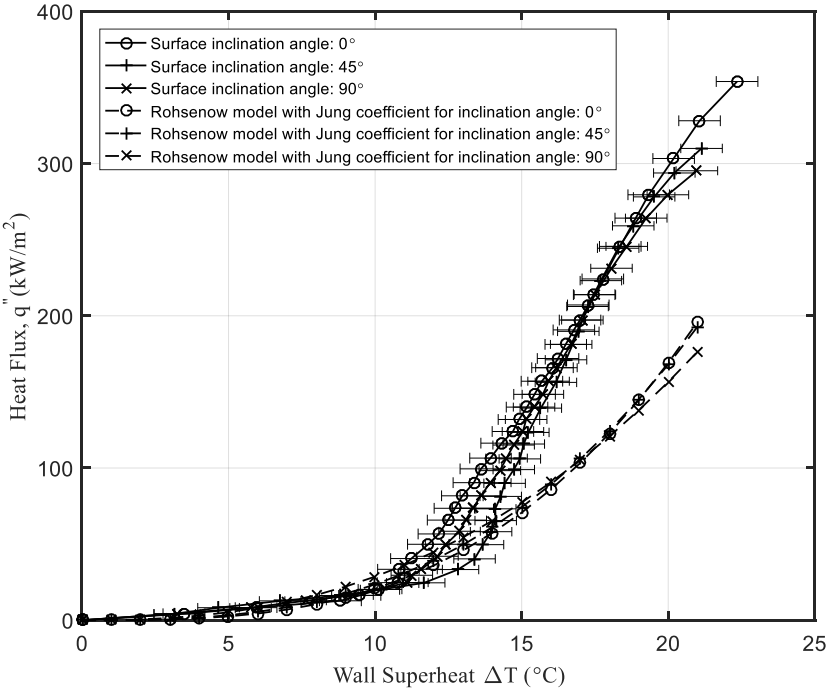

Figure 115: Comparison of pool boiling curves for 1 μm surface at 0°, 45°and 90° surface orientations

In order to quantify this change in CHF, it is convenient to normalize the CHF values obtained for different inclination angles by relating them to CHF_{max}, i.e. the maximum value of

CHF obtained with horizontal upward-facing surface. The correlations used for comparison with experimental data are listed as follows:

Vishnev's correlation [61] for the effect of surface orientation on normalized CHF in pool boiling:

$$\mathrm{CHF/CHF_{max}} = \frac{(190-\theta)^{0.5}}{190^{0.5}} \tag{47}$$

Chang and You's correlation [56]:

$$\mathrm{CHF/CHF_{max}} = (1.0 - 0.00120\theta \tan(0.414\theta) - 0.122\sin(0.38\theta) \tag{48}$$

El-Genk and Bostanci's correlation [57]:

$$\mathrm{CHF/CHF_{max}} = [(1\text{-}0.00127\theta)^{-4} + (3.03\text{-}0.016\theta)^{-4}]^{-0.25} \tag{49}$$

The results are compared in Figure 116 and Table XII. The current experimental $\mathrm{CHF/CHF_{max}}$ of both 1μm and 10 μm surface are almost the same and they lie in between the Vishnev's and EI Genk-Bostanci's correlations. Vishnev's correlation gives better estimation for 45 degree surface orientation, whereas for a vertical surface, prediction based on El-Genk and Bostanci's correlation seems more accurate. Figure 116 confirms that Vishnev's correlation, which was originally derived for cryogenic fluids, provides a good fit for cryogenic fluids and a lower bound for non-cryogenic fluids, whereas correlation by Chang and You provides an upper bound for both the cryogenic and non-cryogenic fluids.

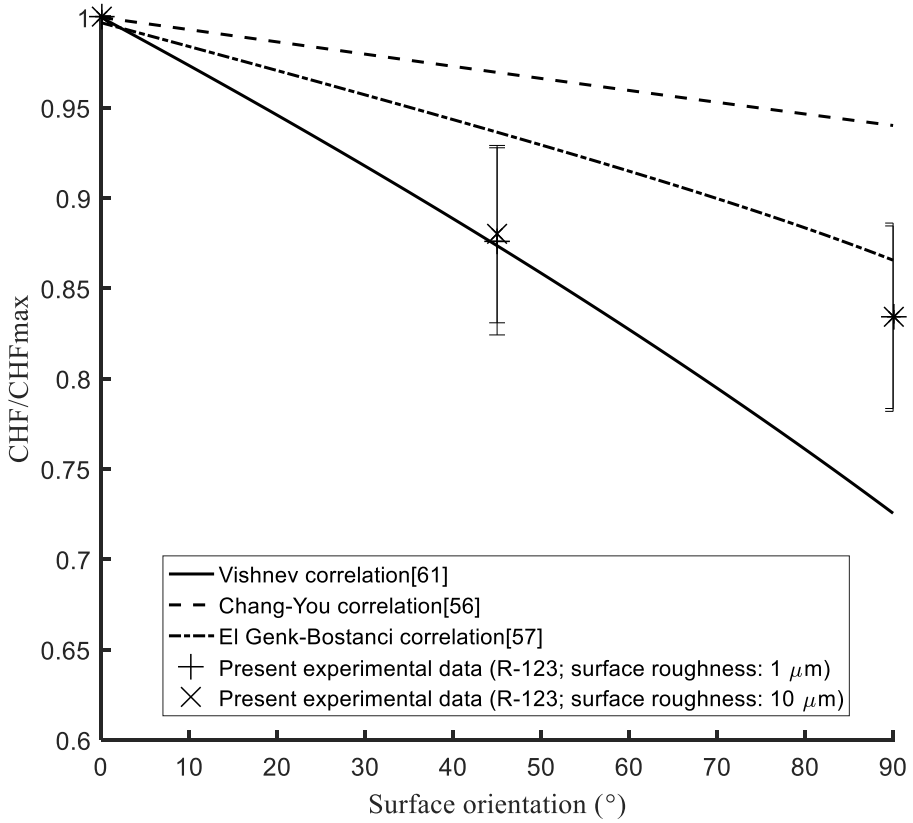

Figure 116: Comparison of normalized CHF between experimental data and correlations

Table XII: Comparison of normalized CHF between the experimental data and correlations

Angle	CHF/CHF_{max} Experimental data (1 μm surface)	CHF/CHF_{max} Experimental data (10 μm surface)	CHF/CHF_{max} (Vishnev's Correlation)	CHF/CHF_{max} (El-Genk's Correlation)	CHF/CHF_{max} (Chang-You's Correlation)
0	1	1	1	1	1
45	0.876	0.88	0.874	0.936	0.97
90	0.834	0.834	0.726	0.866	0.94

4.3.3 Pool boiling heat transfer enhancement with specifically machined surfaces

Comparison of pool boiling curves of increasing heat flux between surfaces machined with different techniques at three surface orientation: horizontal, 45° and vertical, are shown in Figure 117-119, respectively.

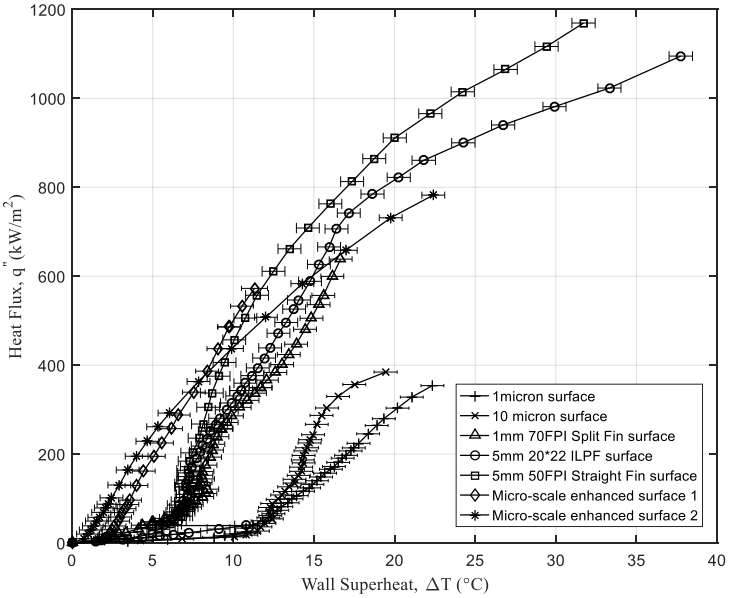

Figure 117: Comparison of pool boiling curves of bare surfaces and enhance surfaces (surface inclination: 0°)

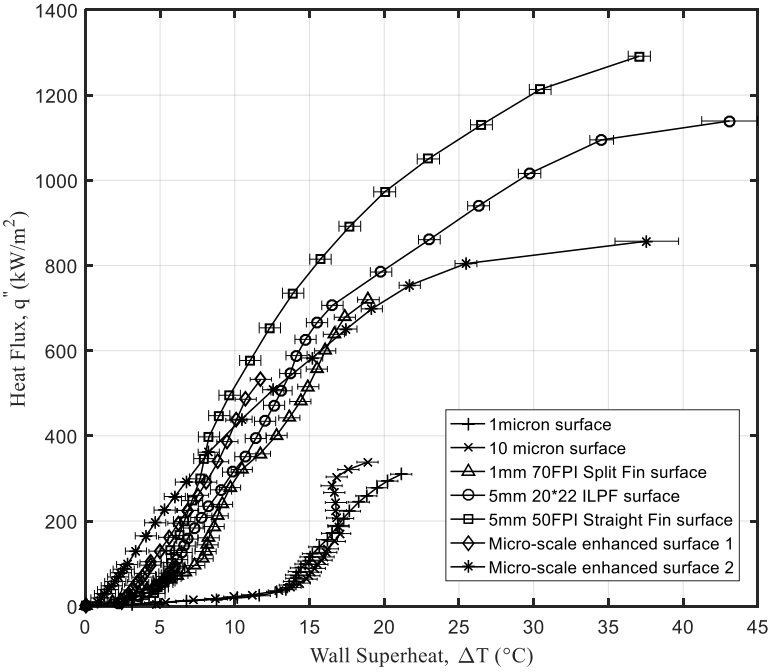

Figure 118: Comparison of pool boiling curves of bare surfaces and enhance surfaces (surface inclination: 45°)

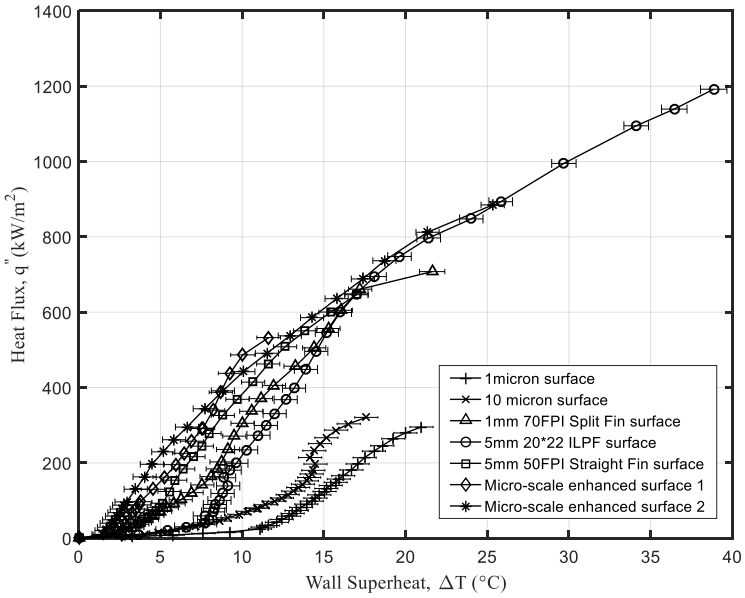

Figure 119: Comparison of pool boiling curves of bare surfaces and enhance surfaces (surface inclination: 90°)

4.3.4 Pool boiling heat transfer enhancement with nanofiber mats

Comparison of pool boiling curves of increasing heat flux between nano-textured surfaces made with fast and slow copper-plated process and bare surface are shown in Figure 120. The upper-rightmost point in each curve represents the critical heat flux point. The nucleate pool boiling curve of the bare surface was studied to characterize the pool boiling curve for this particular fluid-surface combination and was regarded as a reference. It shows that as the heat flux is increased, the wall superheat increases and nucleate boiling starts. It can be seen from Figure 18 that at a given applied heat flux, the wall superheat of pool boiling on slow and fast copper-plated nano-textured surfaces are lower than that of the bare surface, the wall superheat of pool boiling on the slow copper-plated nano-textured surface is the lowest. For instance, at a heat flux of 120 kW/m^2, the wall superheat of pool boiling on slow and fast copper-plated nano-textured surfaces

are 8°C and 10°C respectively, which are much smaller than the wall superheat at the same heat flux condition on the bare surface of 15°C.

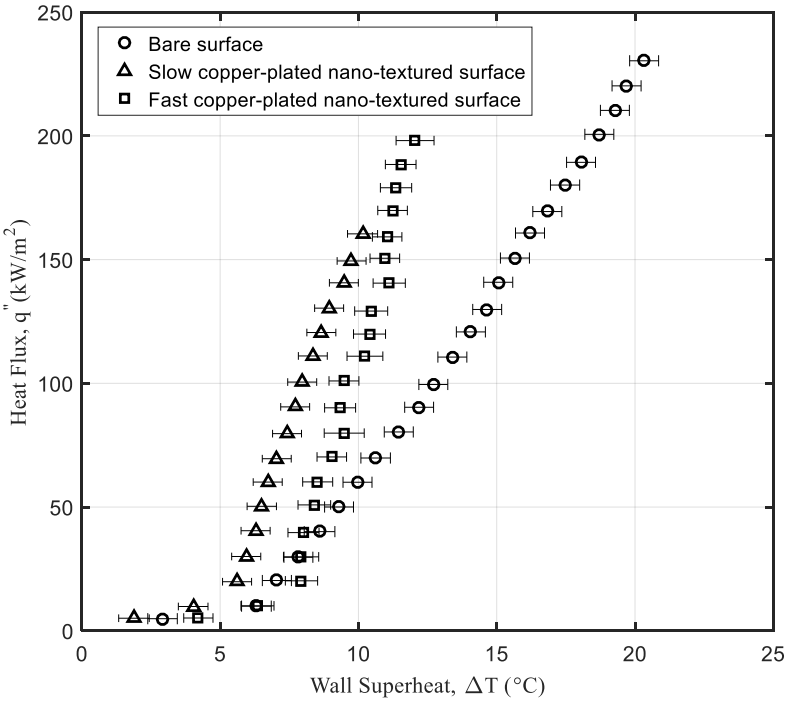

Figure 120: Comparison of pool boiling curves of increasing heat flux between nano-textured surfaces made with fast and slow copper-plated process and bare surface.

It can be seen from Figures 121 and 122 that the largest enhancement to nucleate pool boiling heat transfer coefficient with fast and slow copper-plated nano-textured surfaces are approximately 230% and 260%, respectively. The slow copper-plated nano-textured surface produced a larger nano-fiber surface roughness than that of the fast copper-plated nano-textured surface. The additional roughness may provide additional exposed surface area which would also cause the compression of the curve to the left.

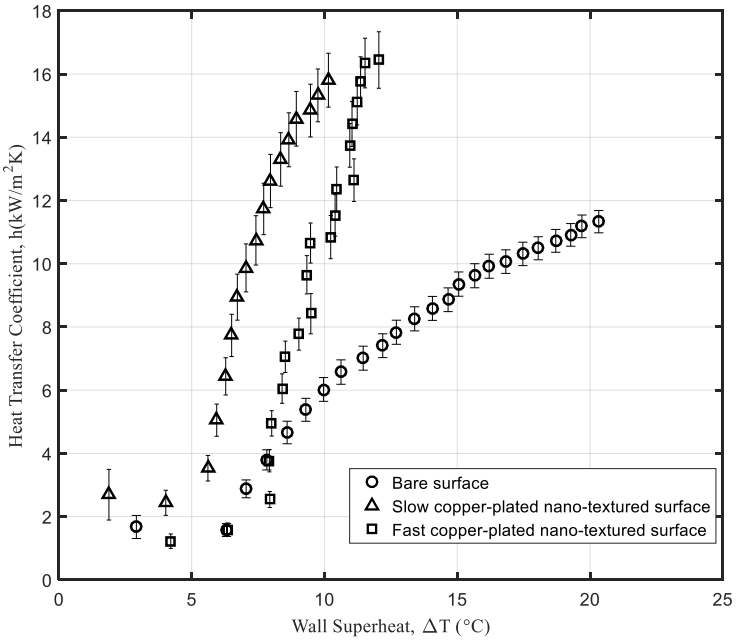

Figure 121: Comparison of Heat transfer coefficient vs. Wall superheat of increasing heat flux between nano-textured surface made with fast and slow copper-plated process and bare surface.

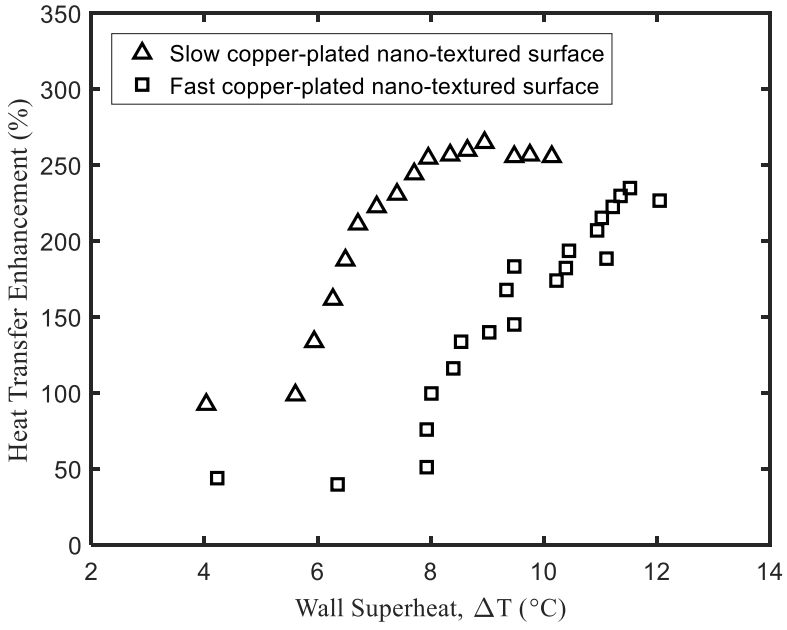

Figure 122: Heat transfer coefficient enhancement of nano-textured surfaces made with fast and slow copper-plated process compared with bare surface.

4.4 Conclusions

Nucleate pool boiling on nano-textured surfaces made of alumina ceramic substrate covered by electrospun nanofiber mats and several specifically machined surfaces was experimentally studied. Significant enhancement in nucleate boiling heat transfer coefficient and critical heat flux was achieved with these modified surfaces. The experimental results indicate that higher density of nucleation sites and larger exposed surface area play important roles in the enhancement of pool boiling heat transfer.

In addition, this study compared nucleate pool boiling heat transfer coefficients obtained with 1μm and 10μm surface roughness and three surface inclination angles. Curve fit for C_{sf} and n based on the current experimental results with 1μm surface roughness matches well with those in Rohsenow's correlation and Cooper's correlation, respectively. The value of CHF/CHF_{max} for 1 micron surface at 0°, 45° and 90° surface orientations were experimentally determined and compared with three correlations. The comparison indicates that the present experimental data lie in between Vishnev's and EI Genk-Bostanci's correlations. Vishnev's correlation gives better estimation for 45 degree surface orientation, whereas for vertical surface, prediction based on El-Genk and Bostanci's correlation seems more accurate. It confirmed that the enhancement of surface roughness could substantially enhance the nucleate pool boiling heat transfer and that the increase of surface inclination angle leads to lower CHF.

CHAPTER 5 EXPERIMENTAL STUDY OF INTERNAL FLOW CONDENSATION USING WATER AS REFRIGERANT UNDER SUB-ATMOSPHERIC PRESSURE

5.1 Introduction

The use of water as a refrigerant has the advantages of zero global warming potential (GWP) and potentially greater efficiency. Literature survey showed that at sub-atmospheric pressure as required by a water driven vapor compression cycle, there is little experimental data available for two-phase heat transfer and pressure drop for in-tube condensation of water as the working fluid. As will be presented below, while several correlations for convective condensation exist, they do not apply specifically to water flow at low mass fluxes within circular mini-channels and therefore the errors can be significant. For these reasons it is desirable to investigate the characteristics for convective condensation in mini-channel experimentally. Specifically, in this study, the in-tube convective condensation heat transfer coefficient and adiabatic pressure drop for water at a below atmospheric saturation pressure as a function of vapor quality in horizontal configuration were measured and presented. Additional limited experiments were also conducted in vertical configuration to confirm the trend observed for the condensation heat transfer coefficient data obtained in horizontal configuration.

5.2 Experiment setup and procedure

5.2.1 Experimental setup

The experiment was designed according to the required operating conditions i.e. circular tube inner diameter, mass flux and saturation temperature, which are shown in Table XIII.

Table XIII: Experimental Parameters

Tube Inner Diameter (mm)	Mass Flux (kg/m^2·s)	Saturation Temperature (°C)
2	5, 10	45
5	1, 10	45

The two-phase flow loop consisted of a pump, various heaters, reservoirs, and temperature, pressure and flow sensors. The schematic and photo of experimental setup are shown in Figure 123 and 124, respectively.

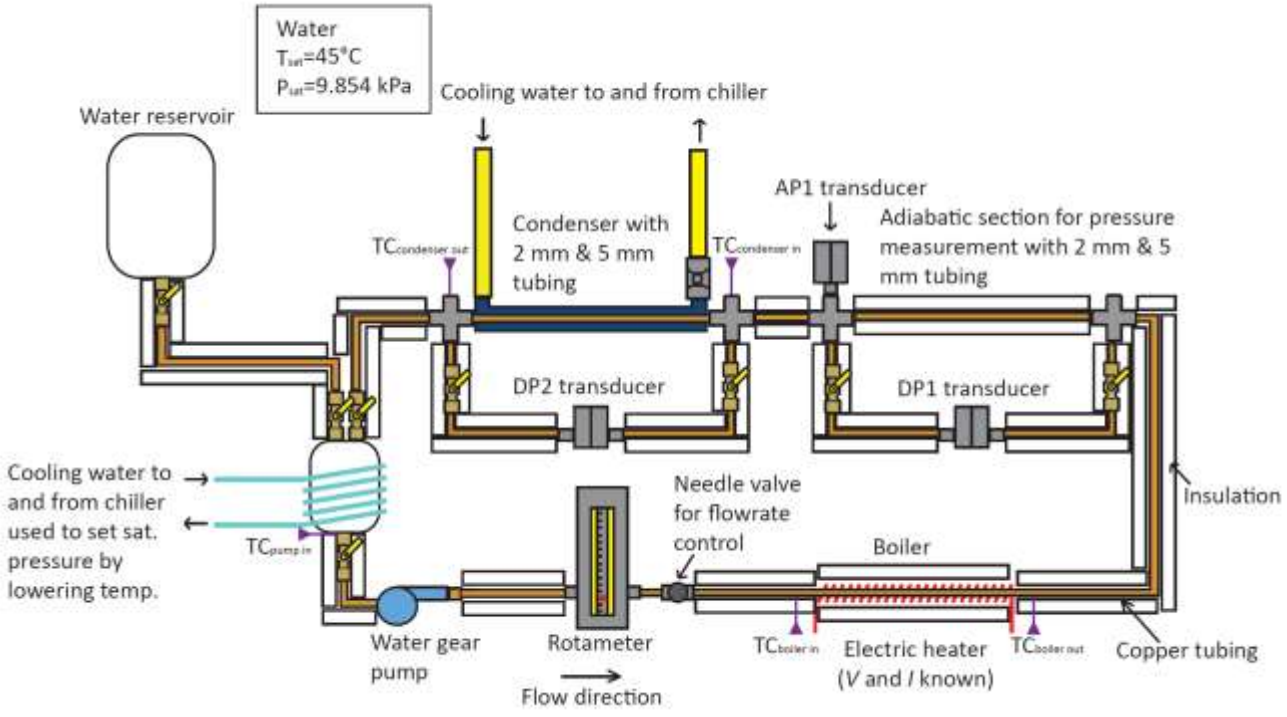

Figure 123: Schematic of experimental setup

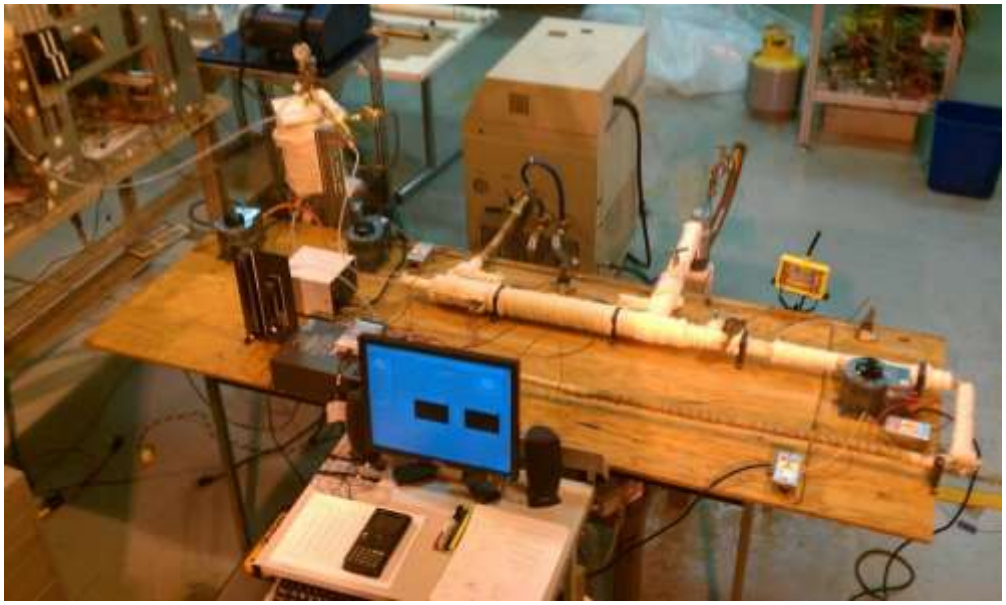

Figure 124: Photograph of experimental setup

A mechanical gear pump was used for pumping the working fluid (distilled water) and the analog dial on the motor controller was used with a needle valve for precise control of flowrate. A rotameter was used downstream of the pump to measure flow rate accurately. The boiler was installed after the rotameter and consisted of a 0.5 inch inner diameter copper tube wrapped around with a high-temperature rope heater. The rope heater provided approximately double the maximum heat that would be required for full phase-change of the water at the given flow rates, to account for heat loss to the environment. The rope heater was covered in several layers of Nomex® thermal insulation fiber to minimize heat loss. T-type probe thermocouples were installed at the inlet and outlet of the boiler for bulk fluid temperature measurements. The rope heater power was controlled by a variac which regulated AC voltage from the electrical power supply. The boiler was followed by the adiabatic section which was heavily insulated to prevent any heat loss to the environment. In addition, a small windowed section was included at the outlet of the adiabatic section to confirm the fluid state as it entered the condenser. The pressure drop across the adiabatic section was measured using a Validyne DP15 differential pressure transducer.

The condenser was a tube-pipe design and consisted of a copper tube of the appropriate inner diameter according to Table 11. The working fluid (distilled water) flowed through the copper tube. The copper tube was installed in a larger steel pipe of 1.5 inches inner diameter. The cooling fluid (tap water) flowed through the annular section between the outer wall of the copper tube and the inner wall of the larger steel pipe. The recirculating chiller (ThermoNESLAB HX150) had a maximum flow rate of 0.646 L/s and minimum temperature setting of 5 °C. The flowrate and inlet and outlet temperatures of the cooling fluid were used to calculate the heat removal rate inside the condenser. On the working fluid side, the bulk temperature at the inlet and outlet of the condenser was measured by probe thermocouples, in the same way as the boiler. In addition to this, an absolute pressure transducer also measured the absolute local pressure at the inlet of the condenser and the thermodynamic condition of the working fluid entering the condenser could be known at any time from these measurements.

The wall temperature measurements in the condenser were made using five fine-gage T-type wire thermocouples which were soldered to the outer wall of the copper tube. Two thermocouples were used per station at the top and bottom of the tube and the average of these were used in heat transfer coefficient calculations. Since the thickness of the tubes was minimal and the thermal conductivity of copper is relatively high, it was assumed that the outer wall temperature approximated the inner wall temperature well. A simple radial, one-dimensional conduction analysis confirmed this assumption. Figure 125 shows a schematic of the wall temperature thermocouples and the locations of stations axially along the tube. The approximate quality at a given station was determined using the distance of the station from the inlet.

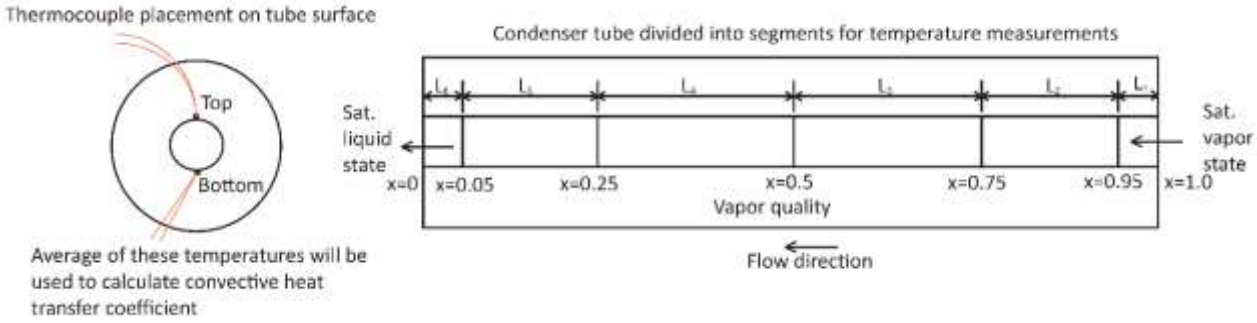

Figure 125: Wall temperature measurement locations in condenser

A reservoir was used to control the overall system pressure by controlling the temperature of the liquid in the reservoir at a given time. This was possible even at the maximum flow rate because the relative volume of the reservoir was much larger than the remainder of the loop. It also ensured that the state of the working fluid could be determined from thermodynamic property tables with a fair amount of accuracy, given the saturation temperature and pressure measurements. All instruments and sensors were connected to a National Instruments Data Acquisition System and a LabVIEW Virtual Instrument was programmed to acquire the data. A sample rate of 10 samples per second was used for all quantities. When the conditions were correct, the data was recorded for 60 seconds. The Maximum systematic error of various measurement devices and experimental uncertainty are given in Table XIV.

Table XIV: Systematic error of all measurement devices and experimental uncertainty for chapter 5

Measurement	Maximum systematic error
Temperature	±0.5°C
Differential Pressure	±15 Pa
Absolute Pressure	±350 Pa
Derived quantity	**Maximum Uncertainty**
Heat transfer coefficient, h	±16 %

5.2.2 Experimental procedure

The loop was first evacuated before any experiments were performed in order to remove air trapped in the tubes. The majority of air dissolved in the distilled water contained in the larger reservoir seen in Figure 123 was also removed by evacuating the top of the working fluid storage reservoir in order to eliminate the influence of non-condensable gas, air in this study, on condensation heat transfer. Distilled water was then charged into the loop and the larger reservoir was isolated from the rest of the setup. It was important to ensure that all the lines were full except the control reservoir as enough expansion volume should be kept to accommodate any sudden increases in system pressure due to, for example, temperature increase. Once the loop was full, single-phase flow was initiated, and measurements of flow rate and pressure drop were taken.

Next, the reservoir saturation condition was set to maintain a system pressure of 9.854 kPa, which corresponded to the required saturation temperature of 45 °C, temperature and pressure were monitored at the inlet of the condenser. The saturation temperature and pressure values deviated slightly from the above stated condition for the various experiments conducted throughout the project. However; these deviations were within 1 °C and thus, their effects on the condensation heat transfer coefficient and adiabatic pressure drop were negligible. Once the

system pressure was achieved and stable, the boiler was started and the applied heat was steadily increased. From the voltage applied and the resistance of the rope heater, the applied electrical power was calculated. This was matched to the heat required for full phase change, found from the flow rate and latent heat of vaporization of the working fluid at the given temperature. This quantity was also matched to the heat removal rate in the condenser, found from the flow rate and bulk temperatures of the cooling fluid, as mentioned above. In reality the electrical power applied was greater than the heat required for full phase change, due to heat loss to the environment. When the saturation temperature and pressure at the inlet of the condenser matched exactly, and when the wall temperatures appeared to follow a trend consistent with condensation heat transfer along the length of the tube, the data were recorded and analyzed.

5.3 Experimental results and discussion

Assuming that there was a constant surface heat flux in the condenser, the heat removal rate, local wall temperature and entrance saturation conditions were used to determine local condensation heat transfer coefficient. Local quality along the length of the tube was also determined from a simple energy balance. Cooling water flow rate in the condenser and heat addition rate in the boiler were adjusted to achieve the desired conditions: water vapor fully condenses at the outlet of the condenser. Measurements were averaged over a specified length of time when steady-state conditions were reached. Note that the pressure along the condenser section decreased, resulting in slight change in the local P_{sat} and T_{sat} values inside the condenser. However; the condensation heat transfer coefficients presented in this report were determined based on the T_{sat} at the condenser entrance, resulting in conservative values.

The heat transfer coefficient and adiabatic pressure drop are plotted as a function of vapor quality. Condensation heat transfer coefficient at a particular station, i, is found using Equation 50.

Here the saturation temperature at the inlet of the condenser is used as the reference bulk fluid temperature. Since the condensation heat transfer coefficient on the vapor side was much higher than the heat transfer coefficient on the water side, the total heat transfer coefficient, *U*, should be close to the heat transfer coefficient on the water sider and should not change much over the condenser length. The water vapor saturation temperature, T_{vapor}, did not change much. The cooling water temperature, $T_{coolingwater}$, did not change much either, as the cooling water flow rate was high. Therefore, the heat flux, equal to U (T_{vapor}-$T_{coolingwater}$), was assumed to be uniform along the condenser.

$$h_i = \frac{q}{A\Delta T} = \frac{\dot{m}_{coolingWater} c_{p\_coolingWater} \left(T_{coolingwaterOut} - T_{coolingwaterIn}\right)}{\pi DL\left(T_{condensern} - T_{wall,i}\right)} \tag{50}$$

The quality was also found in a similar manner, as shown in Equation 51, with the assumption that the fluid entered the condenser as a saturated vapor. This assumption was confirmed by the saturation temperature and pressure measurement at the inlet of the condenser and those values are given in the caption of each plot.

$$x_i = 1 - \frac{q\bar{x}_i}{\dot{m}_{distilledWater} h_{fg\_distilledWater}} = 1 - \frac{\dot{m}_{coolingWater} c_{p\_coolingWater} \Delta T_{coolingWater} \bar{x}_i}{\dot{m}_{distilledWater} h_{fg\_distilledWater}} \tag{51}$$

The adiabatic pressure drop was divided by the adiabatic section length to represent pressure gradient and plotted as a function of vapor quality as well. Figures 126-133 show individual data sets, each of which consists of a convective condensation heat transfer coefficient plot and a pressure gradient for a particular operating condition, giving a total of 8 plots. The experimental data were also compared with aforementioned correlations. Finally, a comparison of all heat transfer coefficients and adiabatic pressure drop was made and the plots are given in Figures 134 and 135.

From the two-phase flow pressure drop measurement in the condenser, it was found that the drop in saturation pressure was not large enough to warrant a change of more than 1°C in the saturation temperature, and this justified the use of only the inlet temperature for all local heat transfer coefficient calculations. In addition to the inlet saturation temperature, another assumption was made regarding the temperature increase of the cooling water. The temperature difference was kept under 1°C in order to maintain a constant heat flux on the surface of the copper tube. In short, the overall heat flux was used to calculate local heat transfer coefficients.

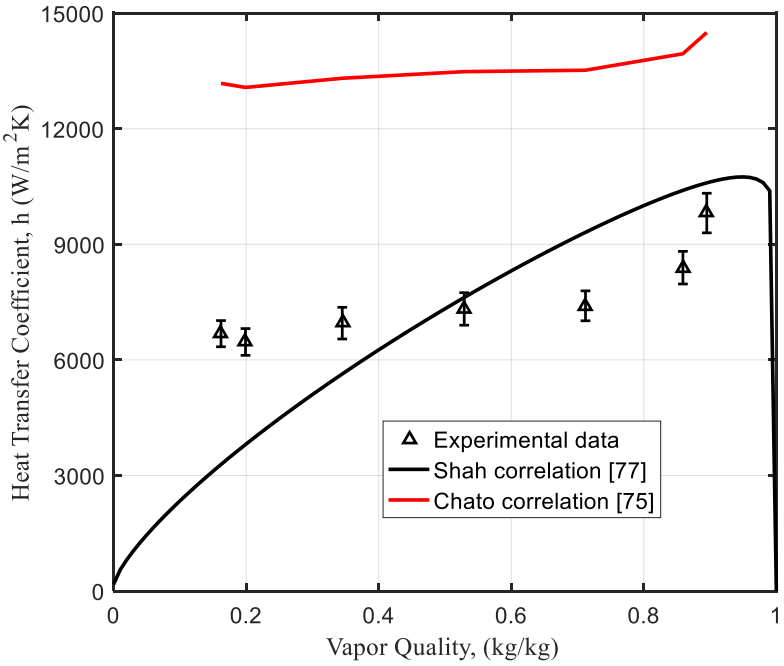

Figure 126: Condensation Heat Transfer Coefficient of Distilled Water vs. Vapor Quality (G=10 kg/m2·s, D=4.8 mm, P_{sat}=11200 kPa, T_{sat}=48.15°C)

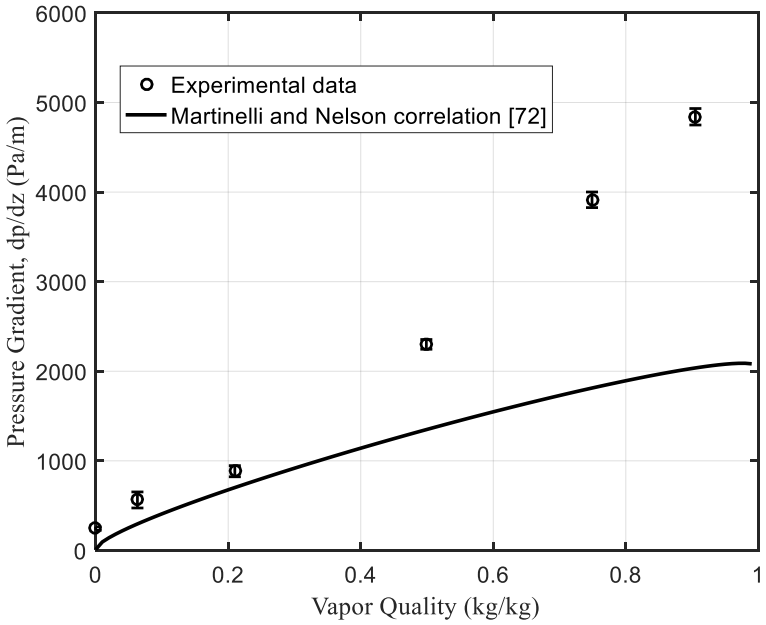

Figure 127: Adiabatic Section Pressure Drop vs. Quality (G=10 kg/m2·s, D=4.8 mm, P_{sat}=11200 kPa, T_{sat}=48.15°C)

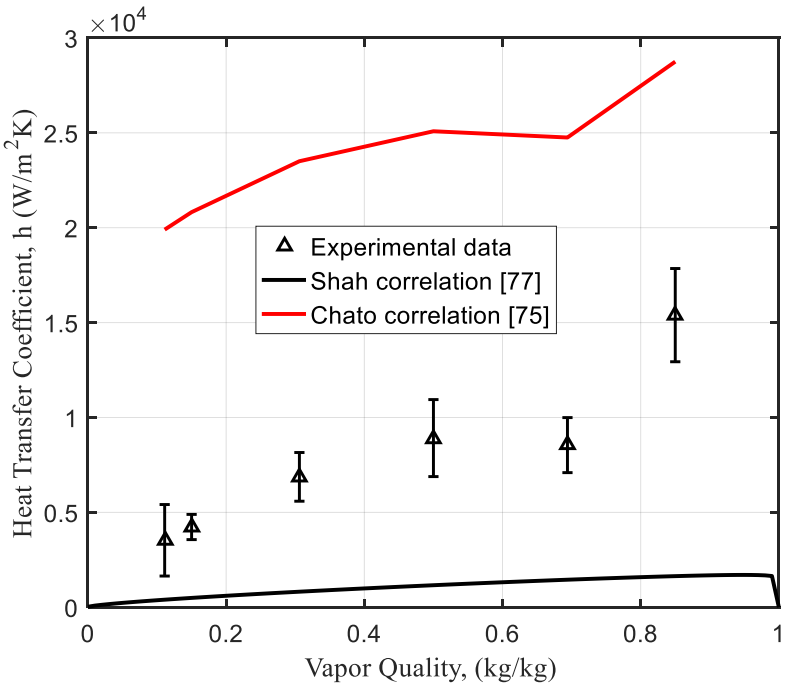

Figure 128: Condensation Heat Transfer Coefficient of Distilled Water vs. Vapor Quality (G=1 kg/m2·s, D=4.8 mm, P_{sat} = 9800 kPa, T_{sat} = 45.52°C)

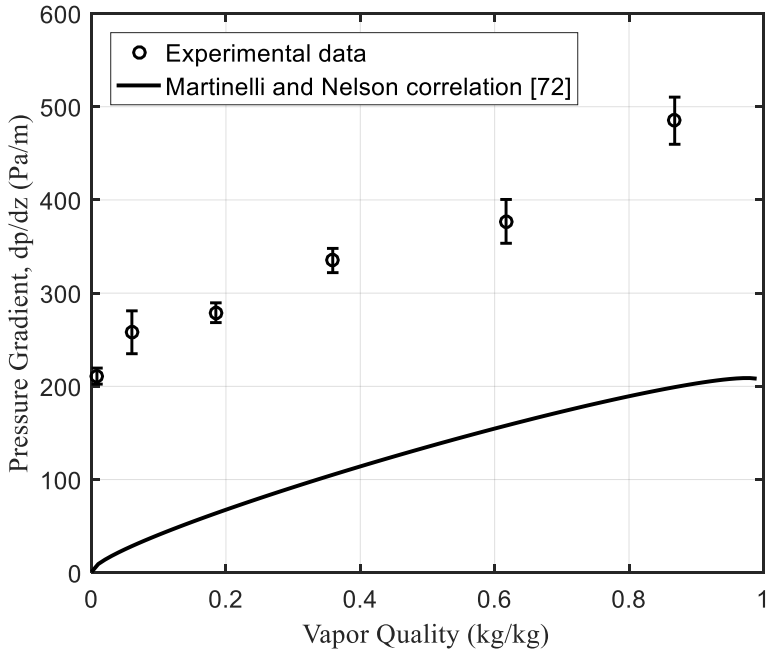

Figure 129: Adiabatic Section Pressure Drop vs. Quality (G=1 kg/m2·s, D=4.8 mm, P_{sat} = 9800 kPa, T_{sat} = 45.52°C)

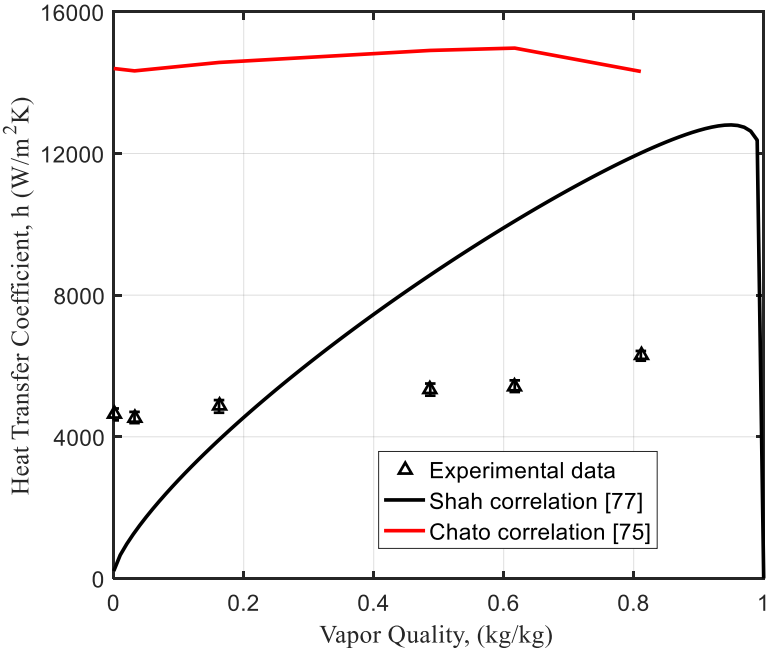

Figure 130: Condensation Heat Transfer Coefficient of Distilled Water vs. Vapor Quality (G = 10 kg/m2·s, D = 2 mm, P_{sat} = 10500 kPa, T_{sat} = 46.7°C)

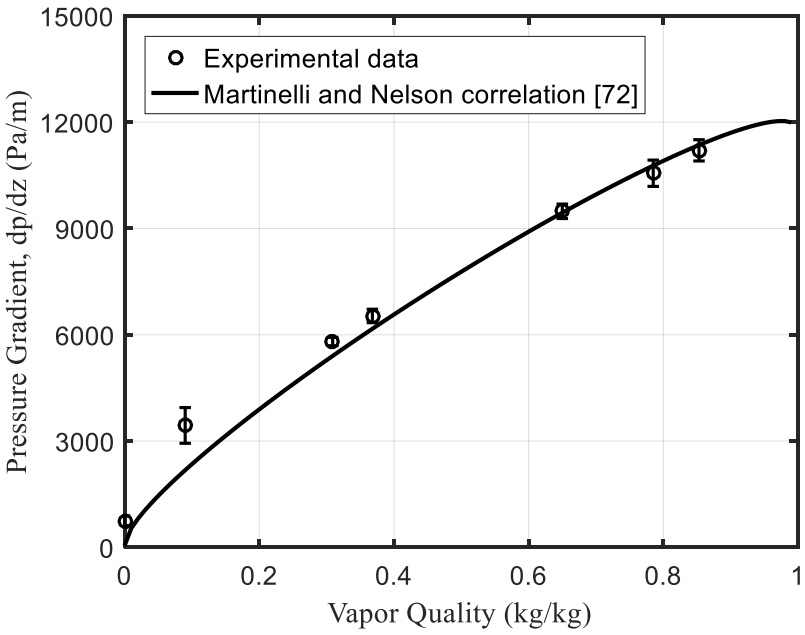

Figure 131: Adiabatic Section Pressure Drop vs. Quality (G=10 kg/m2·s, D=2 mm, P_{sat}=10500 kPa, Tsat=46.7°C)

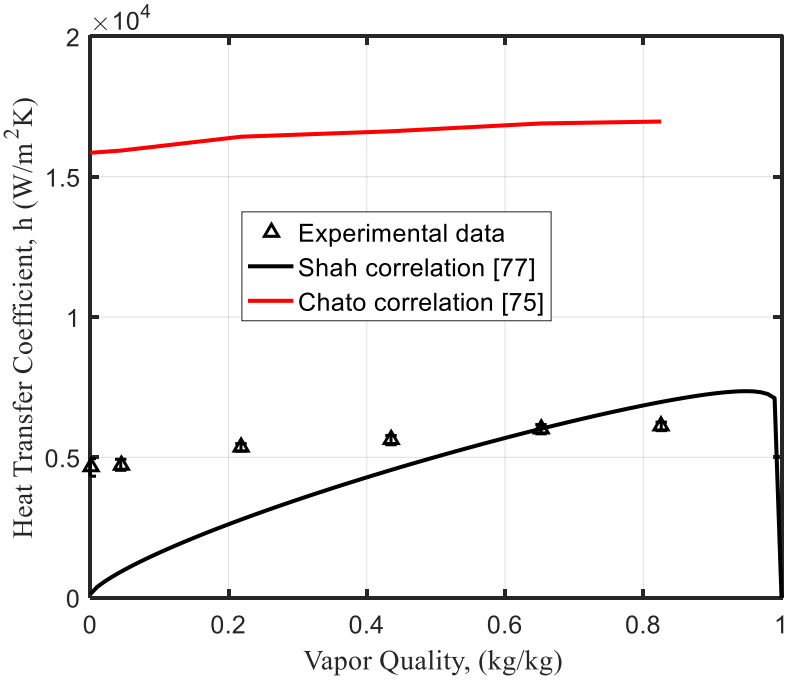

Figure 132: Condensation Heat Transfer Coefficient of Distilled Water vs. Vapor Quality (G=5 kg/m2·s, D=2 mm, P_{sat}=8900 kPa, Tsat=43.5°C)

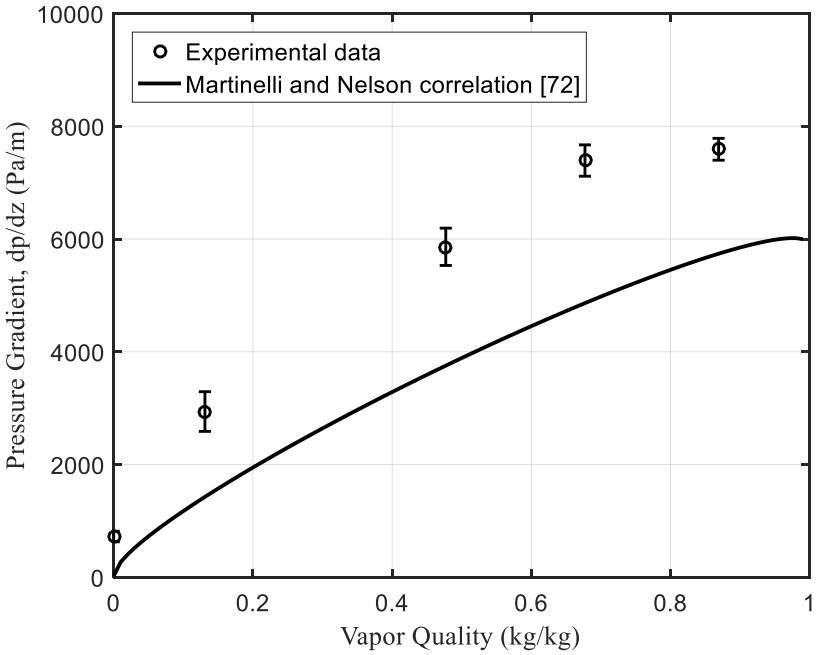

Figure 133: Adiabatic Section Pressure Drop vs. Quality (G=5 kg/m2·s, D=2 mm, P_{sat}=8900 kPa, Tsat=43.5°C)

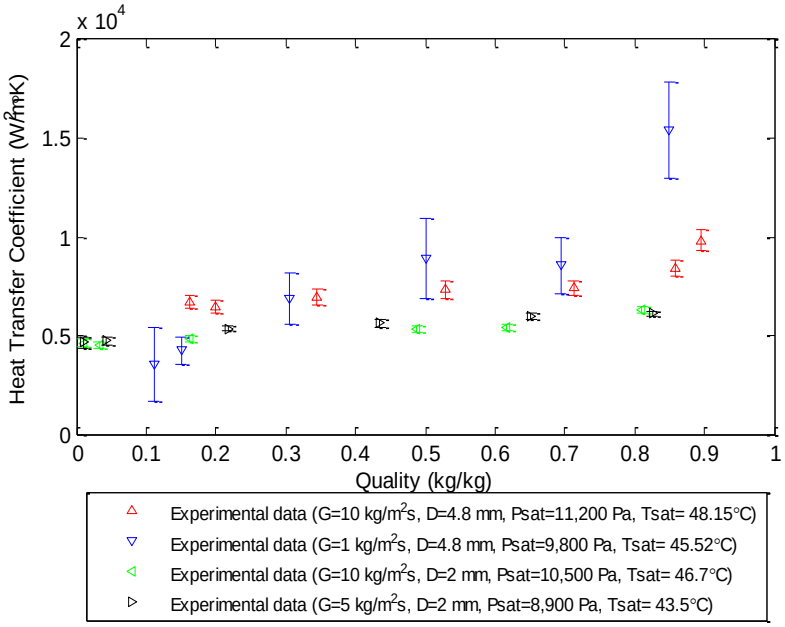

Figure 134: Condensation Heat Transfer Coefficient of Distilled Water vs. Vapor Quality – Final Comparison

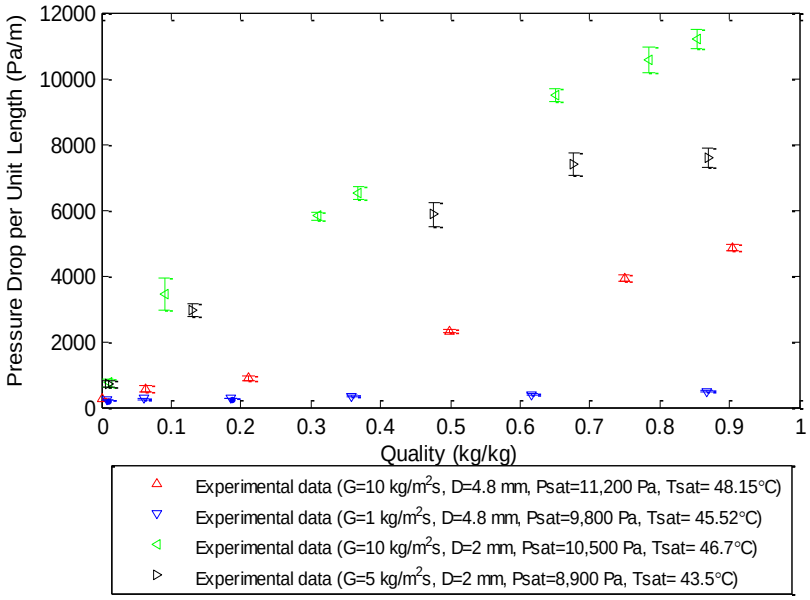

Figure 135: Adiabatic Section Pressure Drop vs. Vapor Quality – Final Comparison

As expected, both convective condensation heat transfer coefficient and adiabatic pressure gradient increased with the vapor quality for all operating conditions. However, the heat transfer coefficients appeared not to increase with increasing mass flux and decreasing tube diameter, which are usually expected for convective condensation in conventional size channel. Instead, they were very similar, indicating that for these mini-channels, the condensation heat transfer coefficient, in general, does not change significantly with the mass flux and tube diameter at a given vapor quality. This is because the vapor Reynolds number, Rev, at the condenser entrance was less than 35,000 (see the values of Rev given below) for all of the operating conditions considered in this study.

D = 4.8 mm, G = 10 kg/m2s (Rev = 4,750)

D = 4.8 mm, G = 1 kg/m2s (Rev = 457)

D = 2.0 mm, G = 10 kg/m2s (Rev = 1,979)

D = 2.0 mm, G = 5 kg/m2s (Rev = 198)

With such low vapor velocities, liquid condensing on the upper portion of the tube wall tends to run down toward the bottom. Additionally, with such low Rev, the shear at the liquid/vapor interface and the tube wall does not significantly affect the transport of heat across the liquid film under the operating conditions considered in this study.

In general, the heat transfer coefficient data does not match with Shah correlation [77] which is based on a purely empirical approach for conventional size channel. However, for aforementioned reasons, they follow similar trends with the correlation developed by Chato [75] for stratified-annular flow condition although they were very different in magnitude. The difference between the experimental data and these two commonly used correlations also confirmed the necessity of experimentally investigating the characteristics for convective condensation of water vapor in mini-channels under low pressure.

The comparison between pressure gradient data and Lockhart-Martinelli-Chisholm correlation [72,73] showed that the general trend of experimental data agreed with the correlation; however, for the two cases of D =4.8 mm, there was a significant difference between them, which is probably due to the secondary flow in the region close to the inlet and outlet of the condenser. For a fixed condenser length, this region is expected to shrink and its effect is expected to become less significant as the tube size decreases, which partially explains a better match between experimental data and correlation for the two cases of D =2 mm. The comparison of all adiabatic pressure gradient data showed that they were very consistent. The largest pressure drop occurred in the smallest tube with the highest mass flux and the lowest pressure drop occurred in the largest tube with lowest mass flux. As expected, losses from frictional pressure drop for single phase flow increase significantly with a reduction in diameter and this was also reflected in the two-phase flow pressure drop.

To confirm the aforementioned observation and determine the effect of gravity on the two-phase flow, additional limited experiments were conducted to measure the condensation heat transfer coefficient in vertical configuration. Only select tests for a single tube were conducted and the results are given in Figures 136 and 137. As shown in these figures, the condensation heat transfer coefficient values do not change significantly with the condenser tube orientation as expected for mini-channels, indicating that gravity force plays a less important role in min-channel two-phase flow as compared to surface tension, inertia force and friction loss.

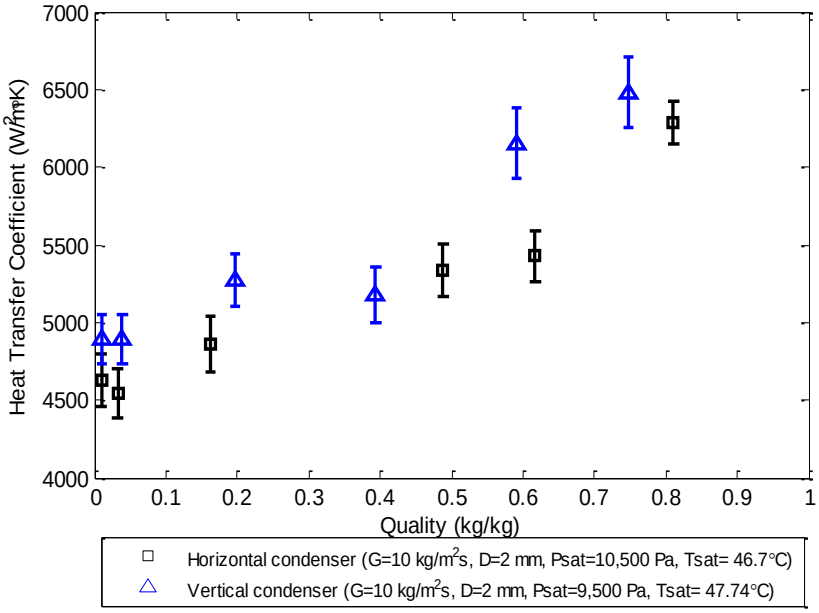

Figure 136: Condensation Heat Transfer Coefficient of Distilled Water vs. Vapor Quality – Comparison between horizontal and vertical condenser orientation

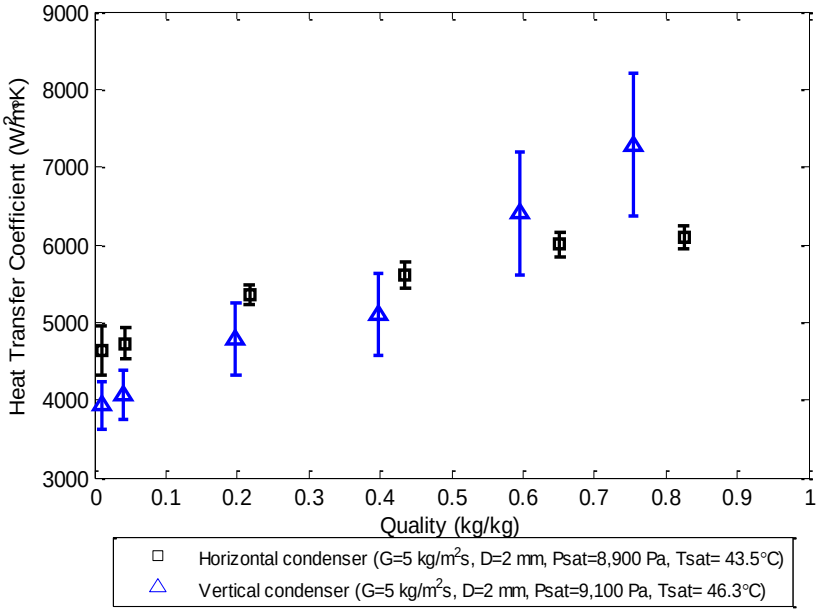

Figure 137: Condensation Heat Transfer Coefficient of Distilled Water vs. Vapor Quality – Comparison between horizontal and vertical condenser orientation

5.4 Conclusions

The in-tube convective condensation heat transfer coefficient and adiabatic pressure drop as a function of vapor quality for water at low saturation pressure and select operating conditions were experimentally measured and presented. The results indicated that the condensation heat transfer coefficient was generally similar in magnitude at a given vapor quality for all operating conditions considered in this study. On the other hand, the adiabatic pressure drop decreases with larger diameter tubes. Both convective condensation heat transfer coefficient and adiabatic pressure drop increase with vapor quality. Comparison of vertical and horizontal orientation of tubes for a fixed mass flux showed a slight increase in the heat transfer coefficient for the vertical tube.

Experimental data of convective flow condensation pressure gradient and heat transfer coefficient were compared with the predictions of Lockhart-Martinelli-Chisholm correlation, and Shah's and Chato's correlations, respectively. In general, they do not apply specifically to water flow at low mass fluxes within circular mini-channels and can only be used as a first approximation. The experimental results achieved in this study can be used for the design of refrigeration cycle using water as the working fluid.

CHAPTER 6 CONCLUSIONS AND RECOMMENDATIONS

6.1 Conclusions

Flow distribution control, and liquid mixing and thermal homogenization in a spherical reservoir via EHD conduction pumping were experimentally studied. In addition, the enhancement of pool boiling and convective flow condensation heat transfer via various techniques such as nanofiber mats and minichannels were experimentally examined. The major contributions of this work are as follows:

Liquid-phase and two-phase flow distribution control via EHD conduction pumping, with possible applications in electronics cooling, were experimentally examined in meso-scale for the first time. The experimental results showed that both liquid-phase and two-phase flow distribution in meso-scale can be effectively controlled via EHD conduction pumping. With the activation of one of the EHD conduction pumps, flow rates could be directed to corresponding branch in a controllable fashion by increasing its applied voltage, resulting in a decrease in the flow rates of other branches. For two-phase study, the maximum total electrical power consumption of the active EHD pump (0.3W) was small compared with the actual total heat transport rate (5.34W) and its flow redistribution capability. The successful recovery of evaporator dryout condition via the activation of the EHD conduction pump in the initially inactive branch was also achieved.

Experimental results also confirmed that the reverse pumping direction configuration was more effective than the same pumping direction configuration. The same direction EHD pumping allowed for more flow on the branch in which EHD pump was installed and reduced the flow on the other branch, while the reverse direction EHD pumping allowed for more flow on the branch with no EHD pumping and reduced the flow on the branch in which EHD pump was installed. The

better performance of reverse EHD conduction pumping was believed to be related to the favorable heterocharge layer development.

The effect of EHD conduction mechanism on thermally homogenizing a fluid with a temperature jump in a spherical reservoir was experimentally studied for the first time. The proposed asymmetric electrode design was especially effective for reservoirs with large diameters given the fact that the resultant electric body forces penetrate into the interior of working fluid. In addition, a numerical analysis of a simplified model of the experimental setup was provided to illustrate fluid mixing and thermal homogenization process. Both experimental and numerical results confirmed that EHD conduction mechanism can be utilized to effectively circulate and mix a thermally non-homogenous liquid inside a reservoir and thus, should be an attractive alternative to current methods of mixing fluids within a storage tank in space application.

Nucleate pool boiling on nano-textured surfaces made of alumina ceramic substrate covered by electrospun nanofiber mats and several specifically machined surfaces was experimentally characterized in terms of heat transfer coefficient (HTC) and critical heat flux (CHF) and compared with bare surface. Significant enhancement in nucleate boiling HTC and CHF were achieved with these modified surfaces. The experimental results indicate that higher density of nucleation sites and larger exposed surface area play important roles in the enhancement of pool boiling heat transfer. It also confirmed that the enhancement of surface roughness could substantially enhance the nucleate pool boiling heat transfer and that the increase of surface inclination angle led to lower CHF.

The in-tube convective condensation heat transfer coefficient and adiabatic pressure drop as a function of vapor quality for distilled water flow in millimeter-scale circular copper tubes at low mass fluxes and sub-atmospheric saturation pressure were experimentally measured and

presented. Their comparison with the predictions of Lockhart-Martinelli-Chisholm correlation, and Shah's and Chato's correlations indicates that, in general, these correlations do not apply specifically to water flow at low mass fluxes within circular mini-channels. The experimental results achieved can be used for the design of a new efficient and cost-effective HVAC system utilizing distilled water as the working fluid.

6.2 Recommendations

Liquid-phase and two-phase flow distribution control via EHD conduction pumping could be further examined in micro-scale in light of the associated enhanced heat transfer and the need of miniature of thermal management system for electronic cooling. In addition to EHD conduction pumping, another EHD pumping mechanism, electrophoretic (DEP) pumping could also be incorporated into such thermal management system, with which more effective and efficient flow distribution control can be expected.

With the experimental confirmation of the reverse pumping direction configuration being more effective than directionally the same pumping configuration, the corresponding numerical study should be conducted. A better fundamental understanding of the effect of flow direction and velocity on EHD conduction phenomenon could be achieved with the numerical analysis on heterocharge layer development.

The effect of EHD conduction mechanism on liquid mixing and thermal homogenization can also be examined with various reservoir geometries in addition to a spherical one used in this study. Numerical analysis of more involved models should carried out to illustrate fluid mixing and thermal homogenization process. The EHD electrode design can be further refined based on such numerical analysis in order to improve the EHD conduction pumping efficiency.

The fundamental understanding of the condenser, used in the vapor compression cycle of refrigeration systems under sub-atmospheric pressure using water as working fluid, is provided in this study. Further study on characterizing the evaporator for such systems are encouraged for the fundamental understating of the related internal flow boiling process.

CHAPTER 7 IMPACT

There are many industrial applications of flow distribution systems, effective controlling of such systems is vital to the enhancement of system efficiency and safety level. The shell and tube heat exchanger, illustrated in Figure 138, is an example of flow distribution used in macro-scale application. Shell and tube heat exchangers are used in a variety of consumer-directed industries. A common problem among shell and tube heat exchangers is maldistribution, an uneven flow distribution among the various tubes comprising the tube side of the heat exchanger. Inconsistent temperatures due to maldistribution can lead to thermal expansion causing the tubes to be removed from their place in the sheet, these tubes may become warped and damaged during this process. Heat-transfer liquid may leak into the solution being processed and results in an impure product not suitable for use or sale. Another problem associated with maldistribution is that heat is not transferred as well when maldistribution occurs and the efficiency of heat exchangers would decrease.

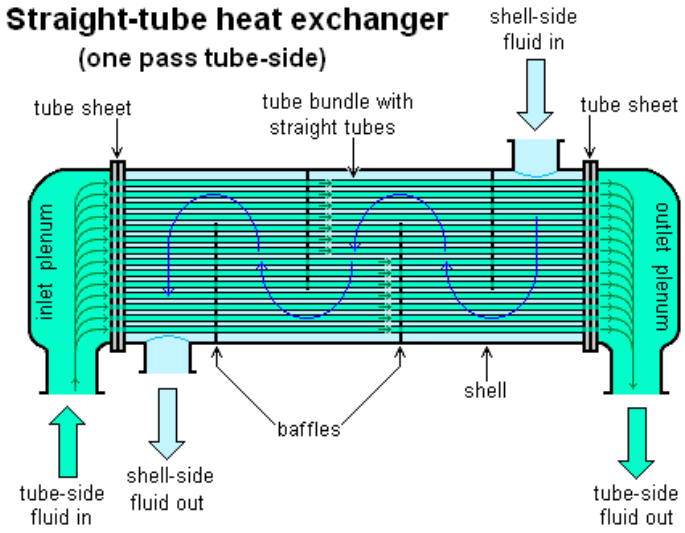

Figure 138: A schematic of shell and tube heat exchanger [121]

In addition to some passive solutions such as installing expansion joint either on the shell side or the tube side of the heat exchanger, flow distribution control via EHD conduction pumping can be used as an active way to prevent maldistribution from happening. The flow rate in each tube in the heat exchange can be effectively adjusted with the activation of the EHD pump in the corresponding branch. The maldistribution condition can be corrected in a timely fashion and therefore, the cost and time it takes to repair or replace the damaged parts due to maldistribution can be slashed.

Flow distribution control via EHD conduction pumping can also be used in micro-scale, for example, in the thermal management system of high heat flux micro-electronics. Micro-scale EHD conduction pumps in such system act as smart control valves controlling the flow rate in each branch. The experimental study in chapter 4 demonstrates that EHD conduction pumping is a very effective low power method capable of controlling flow on demand by simply adjusting its applied voltage. Flow distribution systems with EHD conduction pumping could be utilized to effectively redistribute the flow to accommodate areas with higher heat transfer needs. Thus, it provides a solution to junction level heat removal for local hot spots during the operation of these devices. The experimental results, for reverse pumping direction configuration in chapter 4, can also be used for the optimal design of such systems to increase their efficiency.

Rocket fuel, spacecraft heating and cooling systems, and sensitive scientific instruments on board space station rely on cryogenic fluids. The pressure rise in cryogenic tanks due to the heat from the environment pose risk to these spacecraft. There are a few different techniques to alleviate the increase in pressure. One of them, for example, is based on the venting of fluid out of the tank [122]. However, costly cryogenic fluid is lost during this process and therefore shortens the life of the cooling system or the length of a spacecraft mission. Liquid mixing and

thermal homogenization via EHD Conduction pumping, studied in Chapter 3, provides a vent less solution to this issue. By keeping the cryogenic fluid recirculate in the tank, temperatures at different locations in the tank can be homogenized and the tank pressure is maintain in a certain range. It would allow for more fuel and cryogenic fluid to be available for rockets and thus long distance missions.

With the explosive growth of the internet, cloud computing and high-performance computing, the energy used to cool the computing hardware increased dramatically. U.S. EPA reported that U.S. data centers consume enormous amounts of electricity, some 2% of total energy consumption [123]. Since the development of the first electronic computers in the 1940s, the development of faster and denser circuit technologies and packages has been accompanied by increasing heat fluxes at the chip levels. Comparing with fan cooling, direct immersion liquid cooling can be used to significantly improve the cooling of computing hardware and reduce energy consumption. As illustrated in Figure 139, for the immersion cooling of microelectronic devices, heat generated by the electronic components is directly transferred to the non-conductive liquid based on pool boiling mechanism. The pool boiling experimental study in Chapter 4 provides fundamental understanding for immersion cooling technique. Nano-fiber surfaces and micro-scale enhanced surfaces can be used to augment the heat transfer coefficient for such technique. As a result, microelectronics can be further miniaturized with optimal performance by maintaining temperatures below the thermal limit and the demanding cooling requirement for high performance computing devices can be met.

Figure 139: A photo of direct liquid immersion cooling [124]

Refrigerants R-123 and R-134a are the commonly used working fluids in the vapor compression cycle of HVAC&R systems. However, they have high global warming potential (GWP) and are being phasing out. On the other hand, pure water is proposed to be used as the refrigerant for HVAC&R systems as it has zero GWP and poses no threat to the environment. The study in Chapter 5 is an important step toward this effort. It explores the in-tube convective condensation of pure water in mini-channel under sub-atmospheric pressure and provides valuable information for the design of condenser section in a vapor compression cycle of HVAC&R systems using water as the refrigerant.

APPENDIX A UNCERTAINTY ANALYSIS

A.1 General uncertainty analysis

This section provides a summary of standards and procedures used for the uncertainty analysis of all experimental data presented in this dissertation. It should be pointed out that the uncertainty attributed to a measurement is an estimate for the possible residual error in that measurement after all proposed corrections have been made for the original error. Thus, the uncertainty analysis in this section does not account for factors such as human error in incorrectly reading or connecting a device, for example.

An error source is usually categorized as fixed or random depending on whether the error it introduces is steady or changes during the time of on complete experiment. The errors themselves are called bias or precision errors, and the precision error is presumed to behave randomly, with a zero mean. Both the bias and precision are presumed to represent stationary statistical properties of a Gaussian distributed data set [125].

A.1.1 Systematic uncertainty

Systematic uncertainty represents the bias error of a measurement whereby the true mean μ_X of the variable X is not exactly equal to the true value, X_{true}, of the quantity being measured. A number of elemental error sources may affect the systematic uncertainty of a measurement: measurement system errors, system-sensor interactions, system disturbances, and conceptual errors. The uncertainty related to these errors contributes to the fixed error component of the overall uncertainty in the final result.

Among these errors, measurement system errors are inherent in the measurement devices, and they are caused by many factors: for example, calibration, curve-fitting of calibration data and errors in the data acquisition system. The analytical approach to estimating measuring system

errors requires an estimate of the fixed and random components of error from each component of the system, usually based on the manufacturer's specifications. The manufacturer's specification description of an error can be converted into an estimate of the equivalent standard deviation, which would also describe the data. For example, if a manufacturer states that a component is accurate within 0.1% of full scale, this could be interpreted to mean that the odds are 20 to 1 against the error being larger than 0.1 % of full scale. This interpretation is equivalent to claiming that for that error source was 0.05% of full scale [125].

A.1.2 Random uncertainty

Random uncertainty due to random errors in a measurement is contributed by the present experiment, partly from the instrumentation and partly by the process instability. Random uncertainty is characterized by the mean and standard deviation. For a given measurement, a fixed number of measurements, n, of data points, x_i, are acquired. The arithmetic mean, $\bar{x}$, and standard deviation, s_x, of these are found in order to quantify the scatter of the data. The arithmetic mean is the summation of all measured values divided by the number of values.

$$\bar{x} = \frac{1}{n}\sum_{i=1}^{n} x_i \tag{52}$$

The standard deviation is found using

$$s_x = \sqrt{\frac{1}{n-1}\sum_{i=1}^{n}(x_i - \bar{x})^2} \tag{53}$$

where n-1 is used in the denominator.

A.1.3 Propagation of uncertainty

In many experiments, the final result is determined by inputting measured variables into a well-known equation that governs the physical phenomena. Kline and McClintock [126], and Moffat [125] showed that the uncertainty in a computed result could be estimated with good accuracy using a root-sum-square combination of the effects of each of the individual inputs and that the RSS operation express the uncertainty in the calculated result at the same odds as were used in estimating the uncertainties in the measurement.

Consider a calculated result, R, which is a function of measured variables, X_1, X_2, X_3… and so on, we have

$$R = R(X_1, X_2, \cdots, X_N) \tag{54}$$

The contribution made by the uncertainty in one variable, δX_i, towards the overall uncertainty of the result, δR, can be found using the root-sum-square (RSS) method

$$\delta R = \left\{ \sum_{i=1}^{N} \left(\frac{\partial R}{\partial X_i} \delta X_i \right)^2 \right\}^{\frac{1}{2}} \tag{55}$$

The partial derivatives of R with respect to X_i are known as the sensitivity coefficients. This is the basic equation of uncertainty analysis [125].

A.1.4 Examples of uncertainty analysis

Calculation of propagation of uncertainty can be illustrated by an example. In Chapter 4, Equation 42 is used to determine pool boiling heat transfer coefficient from experimentally measured values and it is repeated here for convenience

$$h = \frac{q''}{\Delta T} \tag{1}$$

In order to perform the uncertainty analysis, we can apply equation 55 as follows to determine the overall uncertainty in the heat transfer coefficient, δh

$$\delta h = \sqrt{\left(\frac{\partial h}{\partial q"}\delta q"\right)^2 + \left(\frac{\partial h}{\partial \Delta T}\delta \Delta T\right)^2} \tag{2}$$

The partial derivatives are found by taking the partial derivatives of equation 57

$$\frac{\partial h}{\partial q"} = \frac{1}{\Delta T} \;\; and \;\; \frac{\partial h}{\partial \Delta T} = -\frac{q"}{(\Delta T)^2} \tag{3}$$

Substituting into equation 58 gives

$$\delta h = \sqrt{\left(\frac{1}{\Delta T}\delta q"\right)^2 + \left(-\frac{q"}{(\Delta T)^2}\delta \Delta T\right)^2} \tag{4}$$

Before proceeding, the contributions made by the uncertainty in each variable must be known. Therefore, a similar analysis must first be performed for each individual variable, i.e. the heat flux and temperature difference. However, the individual contributors to the heat transfer coefficient are themselves determined by separate equations which relate measured quantities. The heat flux is determined from measured heater voltage, resistance, and surface area.

$$q" = \frac{U^2}{RS} \tag{60}$$

Application of equation 60 leads to

$$\delta q" = \sqrt{\left(\frac{2U}{RS}\delta U\right)^2 + \left(-\frac{U^2}{(R)^2 S}\delta R\right)^2 + \left(-\frac{U^2}{R(S)^2}\delta S\right)^2} \tag{61}$$

The temperature difference is a straightforward subtraction of one measured temperature from another.

$$\Delta T = T_1 - T_2 \tag{62}$$

Application of equation 62 results in

$$\delta\Delta T = \sqrt{(\delta T_1)^2 + (-\delta T_2)^2} \tag{63}$$

A.2 Temperature

Various T-type thermocouples were used for temperature measurement since they have a wide temperature range (-200 to 350°C) and a higher accuracy than the other types of thermocouples. Specifically, fine-gage (36 AWG) wire thermocouples were used for surface temperature measurement and stainless steel probe thermocouples were used for bulk fluid temperature measurement.

The National Institute of Standards and Technology (NIST) provides standardized relations between the voltage output of a thermocouple and the corresponding temperature, based on a reference junction (cold junction) that is at a temperature of 0 °C [127]. The relationship between thermoelectric voltage, *V*, and temperature *T* is given by

$$V = \sum_{i=0}^{n} c_i (T)^i \tag{64}$$

where *V* is in mV, *T* is in °C, and c_i is the polynomial coefficients. The inverse relationship is given by:

$$T = \sum_{i=0}^{n} d_i (V)^i \tag{65}$$

Where d_i is inverse polynomial coefficients. Both coefficients for each thermocouple type for a given temperature range are provided in NIST ITS-90 Thermocouple Database.

In all experiments, thermocouple readings were taken by National Instruments NI 9213 data acquisition system (DAQ). The system measures the voltage at the terminals with an accuracy

of 0.01% of the reading at 25 °C, with this resolution, the accuracy of measurement for T-type thermocouples corresponded to of ±0.02 °C for T-type thermocouples. The data acquisition system had built-in cold junction compensation, eliminating the need for maintaining the reference at a known temperature with a fixed-temperature ice bath, for example.

In some experiments, Resistance Temperature Detectors (RTDs) were used. Specifically, surface-mount RTDs were used for surface temperature measurement and stainless steel probe RTDs were used for bulk fluid temperature measurement. The surface-mount RTDs were Omega SA1-RTD 100 Ω with a class "A" accuracy of ± (0.15 + 0.002 |T|)°C. The probe PRTs were Omega P-M-A-1/8-6-0-P-3 100 Ω with a class "A" accuracy of ± 0.15% at 0°C. Resistance was measured using the 4-wire method in order to account for the additional resistance of connecting wires.

The National Instruments NI 9219 data acquisition system was used for these measurements, with a 24-bit resolution, 50/60 Hz noise rejection and support for 3- and 4-wire RTDs with built-in excitation and automatic detection.

The Callendar-Van Dusen equation was used to determine the relationship between resistance, *R*, and temperature, *T*, for these standard 100 Ω platinum RTDs, as shown below:

$$R(T) = R_0[1 + AT + BT^2 + CT^3(T - 100)] \quad (-200°C < T < 0°C)$$

$$R(T) = R_0[1 + AT + BT^2] \quad (0°C \leq T \leq 850°C)$$

$$A = 3.9083 \times 10^{-3}°C^{-1} \tag{66}$$

$$B = -5.775 \times 10^{-7}°C^{-1}$$

$$C = -4.183 \times 10^{-12}°C^{-4}$$

where *R* was in *Ω*, *T* was in °C and R_0 was the resistance at 0°C.

A.3 Pressure

Differential pressure was measured using Validyne DP-15 variable reluctance pressure transducers. A carrier-demodulator was used to convert the high-frequency carrier signal from the transducer into an analog voltage which was input into the data acquisition system. The accuracy of the transducers was ±10 Pa. Transducers were calibrated in the lab with a manometer as the reference and the range was 0-3.5 in of water or 0-882 Pa. The accuracy of the manometer was determined by the smallest graduation on the scale, which was ±0.01 in, or ±2.5 Pa in hydrostatic pressure of the water column. The absolute pressure or system pressure was measured using a Validyne AP-10 pressure transducer, in the range of 0-140 kPa. The accuracy of this transducer was ±350 Pa.

Voltage signals from the pressure transducers were measured using the National Instruments USB 6211 16-Bit, 250 kS/s M Series multifunction data acquisition system. It had 16 analog inputs (16-bit, 250 kS/s) and 2 analog outputs (16-bit, 250 kS/s) with 4 digital inputs, 4 digital outputs and 2 32-bit counters. The maximum voltage range was -10 V to 10 V with an accuracy of 2.69 mV. The minimum voltage range was -200 mV to 200 mV with an accuracy of 0.088 mV.

A.4 Flow rate

Flow rate was measured using a Sensirion HLQ-60 flow sensor. The flow meter was chosen based on the flow rate range, compatibility of wetted parts with the working fluid and cost. The calibration curve of analog output voltage vs. flow rate, provided by the manufacturer, is for Isopropyl Alcohol:

$$Q = c_1 \left[\exp\left(\frac{V-5}{c_2}\right) - 1\right] \tag{67}$$

Where c_1 = 0.333mL/min and c_2 = 0.729V. Use with other fluids requires calibration using that fluid (in this study, refrigerant HCFC-123 and 3M™ Novec™ 7600).

To calibrate the flow sensor, refrigerant HCFC-123 and 3M™ Novec™ 7600 was drained from a reservoir tank, through the meter, through a throttling valve, and into a collection tank. The collection tank was placed on a scale which had an accuracy 2 g. A stopwatch with an accuracy of 0.01s was used to measure the time. The measured mass flow rate was then converted to a volumetric flow rate using fluid density at ambient conditions.

The flow rate range was 0-52 ml/min. The flow detection response time was < 50 ms and accuracy was ±10% of the measured value. Repeatability was 0.2 sec and the integration time was 1.5% of the measured value or 0.2% of the full scale range. Voltage signals from the flow meters were measured using the National Instruments USB 6211 data acquisition system described above.

A.5 Voltage and current

The heater and evaporator power supplies for all experiments was an Acopian Y0120LXB600, which had a voltage range of 0-120 VDC and current range of 0-6 A. The voltage load regulation was ±0.05% of the maximum or 5 mV, whichever is greater. For remote programming, a 0-10 V signal was used which was linearly proportional to output voltage. The input voltage resolution accuracy was 0.5% of maximum rated output voltage. In the same way, the accuracy of the input current was 3% of maximum rated output current. Voltage signals from the power supplies were measured using the National Instruments USB 6211 data acquisition system described above. In addition, analog output voltage signals for control of power supplies were also applied using the same DAQ board.

A.6 EHD voltage and current

The power supply for EHD pumps in experiments of Chapter 2 was a Trek 677B which had a voltage range of 0-1.5 kV DC. The input voltage signal was amplified at a gain of 200 V/V. The current range was 0-5 mA. The output voltage had a resolution of 1V. The voltage monitor had a DC accuracy better than 0.1 % of full scale, with offset voltage < 5 mV and output noise < 10 mV rms. The current monitor had a scale factor of 1 V/mA and DC accuracy better than 0.1 % of full scale. National Instruments USB 6211 data acquisition system, described above, was used to measure the voltage signals from the power supplies and send out analog output voltage signals to control power supplies.

The power supply for the EHD pumps in experiments of Chapter 3 was a Glassman Series EH HV supply which had a voltage range of 0-30 kV DC and a current range of 0-3 mA. The power supply had built in voltage and current monitors and analog output voltage control. The units could be configured in either fixed-voltage or fixed-current modes. National Instruments USB 6211 data acquisition system, described above, was used to measure the voltage signals from the power supplies and send out analog output voltage signals to control power supplies.

REFERENCES

[1] Pickard W., Progress in dielectrics. Vol 6 Heywood, London:1-39, 1965.

[2] Stuetzer O. M., "Ion drag pressure generation," Journal of Applied Physics 30 (7):984-994, 1959.

[3] Pickard, W. F., "Ion drag pumping. I. Theory," Journal of Applied Physics 34 (2):246-250, 1963.

[4] Pickard W.F., "Ion drag pumping. II. Experiment," Journal of Applied Physics 34 (2):251-258, 1963.

[5] Melcher J. R., "Electrohydrodynamic and magnetohydrodynamic surface waves and instabilities," Physics of Fluids (1958-1988) 4 (11):1348-1354, 1961.

[6] Brand, K., and Seyed-Yagoobi, J., "Effect of electrode configuration on electrohydrodynamic induction pumping of a stratified liquid/vapor medium," IEEE Transactions on Industry Applications 38 (2):389-400, 2002.

[7] Darabi, J., Rada, M., Ohadi, M., and Lawler, J., "Design, fabrication, and testing of an electrohydrodynamic ion-drag micropump," Journal of Microelectromechanical Systems 11 (6):684-690. doi:10.1109/JMEMS.2002.805046, 2002

[8] Patel, V.K., Robinson, F., Seyed-Yagoobi, J., and Didion, J., "Terrestrial and Microgravity Experimental Study of Microscale Heat-Transport Device Driven by Electrohydrodynamic Conduction Pumping," IEEE Transactions on Industry Applications 49 (6):2397-2401, 2013.

[9] Talmor, M. and Seyed-Yagoobi, J., "Electrohydrodynamically Augmented Internal Forced Convection", a Chapter in Handbook of Thermal Science and Engineering, Edited by Francis A. Kulacki, Springer Publishing Co., New York, New York, in press.

[10] Melcher, J. R., Continuum electromechanics. MIT Press, Cambridge, Mass, 1981.

[11] Crowley, J. M., Fundamentals of applied electrostatics. John Wiley & Sons, 1986.

[12] Seyed-Yagoobi, J., "Electrohydrodynamic pumping of dielectric liquids," Journal of Electrostatics 63 (6):861-869, 2005.

[13] Al Dini, S. A. S., "Electrohydrodynamic induction and conduction pumping of dielectric liquid film: theoretical and numerical studies," Texas A&M University, 2007

[14] Crowley, J. M., Wright, G. S., and Chato, J.C., "Selecting a working fluid to increase the efficiency and flow rate of an EHD pump," IEEE Transactions on Industry Applications 26 (1):42-49, 1990.

[15] Chattock, A,, Walker, W.E., and Dixon, E., "On the specific velocities of ions in the discharge from points," The London, Edinburgh, and Dublin Philosophical Magazine and Journal of Science 1 (1):79-98, 1901.

[16] Seyed-Yagoobi, J., Krein, P. T., Crowley, J. M., and Chato, J. C., "Effects of long-term low-level charge injection on insulating oil," In: Conference on Electrical Insulation & Dielectric Phenomenon - Annual Report 1984, 21-25 Oct. 1984 1984. pp 307-311. doi:10.1109/EIDP.1984.7684004

[17] Melcher, J. R., "Traveling-Wave Induced Electroconvection," Phys Fluids Physics of Fluids 9 (8):1548, 1966.

[18] Melcher, J., and Taylor G., "Electrohydrodynamics: a review of the role of interfacial shear stresses," Annual Review of Fluid Mechanics 1 (1):111-146, 1969

[19] Onsager, L., "Deviations from Ohm's law in weak electrolytes," The Journal of Chemical Physics 2 (9):599-615, 1934

[20] Pontiga, F., and Castellanos, A. “The effect of field-enhanced injection and dissociation on the conduction of highly-insulating liquids,” IEEE transactions on dielectrics and electrical insulation 3 (6):792-799, 1996.

[21] Atten, P., and Seyed-Yagoobi, J., “Electrohydrodynamically induced dielectric liquid flow through pure conduction in point/plane geometry,” IEEE Transactions on Dielectrics and Electrical Insulation 10 (1):27-36, 2003

[22] Yazdani, M., and Seyed-Yagoobi, J., “Electrically induced dielectric liquid film flow based on electric conduction phenomenon,” IEEE Transactions on Dielectrics and Electrical Insulation 16 (3):768-777, 2009.

[23] Yazdani, M., Yagoobi, J. S., “The effect of uni/bipolar charge injection on EHD conduction pumping,” Journal of Electrostatics 75:43-48, 2015.

[24] Kano, I., and Nishina, T., “Effect of electrode arrangements on EHD conduction pumping,” IEEE Transactions on Industry Applications 49 (2):679-684, 2013.

[25] Yang, L., Minchev, K. S., Talmor, M., Jiang, C., Shaw, B. C., and Seyed-Yagoobi, J., “Flow distribution control in meso scale via electrohydrodynamic conduction pumping,” In: Industry Applications Society Annual Meeting, 2015 IEEE, 2015. IEEE, pp 1-8.

[26] Pearson, M., and Seyed-Yagoobi, J., “Advances in electrohydrodynamic conduction pumping,” IEEE Transactions on Dielectrics and Electrical Insulation 2 (16):424-434, 2009

[27] Mahmoudi, S., Adamiak, K., and Castle, G.P., “Prediction of the static pressure generation for an electrohydrodynamic conduction pump,” In: 2011 IEEE International Conference on Dielectric Liquids, 2011. IEEE, pp 1-7

[28] Feng, Y., and Seyed-Yagoobi, J., "Understanding of electrohydrodynamic conduction pumping phenomenon," Physics of Fluids (1994-present) 16 (7):2432-2441, 2004

[29] Ramos, A., "Electrokinetics and electrohydrodynamics in microsystems, vol 530. Springer Science & Business Media, 2011.

[30] Stern, O., "The theory of the electrolytic double-layer," Z Elektrochem 30 (508):1014-1020, 1924.

[31] Dutta, P., and Beskok, A., "Analytical solution of combined electroosmotic/pressure driven flows in two-dimensional straight channels: finite Debye layer effects. Analytical chemistry 73 (9):1979-1986, 2001.

[32] Gong, L., and Wu, J. K., "Resistance effect of electric double layer on liquid flow in microchannel," Applied Mathematics and Mechanics 27:1391-1398, 2006.

[33] Tardu, S., "Analysis of the electric double layer effect on microchannel flow stability," Microscale Thermophysical Engineering 8 (4):383-401, 2004.

[34] Cao, J., Cheng, P., and Hong, F., "Applications of electrohydrodynamics and Joule heating effects in microfluidic chips: A review," Science in China Series E: Technological Sciences 52 (12):3477-3490, 2009.

[35] Castellanos, A., Ramos, A., Gonzalez, A., Green, N. G., and Morgan, H., "Electrohydrodynamics and dielectrophoresis in microsystems: scaling laws," Journal of Physics D: Applied Physics 36 (20):2584, 2003

[36] Zhakin, A., "Conduction Phenomenon in Dielectric Liquids, EHD Models, Linear and Nonlinear Effects on the Charged Interface, EHD Pumping of Dielectric Liquids," COURSES AND LECTURES-INTERNATIONAL CENTRE FOR MECHANICAL SCIENCES 1 (380):83-162, 1998.

[37] Washabauch, A., Zahn, M., and Melcher, J., “Electrohydrodynamic traveling-wave pumping of homogeneous semi-insulating liquids,” IEEE transactions on electrical insulation 24 (5):807-834, 1989.

[38] Atten, P., and Seyed-Yagoobi, J., “Electrohydrodynamically induced dielectric liquid flow through pure conduction in point/plane geometry-theory,” In: Proceedings of the 1999 IEEE 13th International Conference on Dielectric Liquids (ICDL '99), 1999. IEEE, pp 231-234

[39] Jeong, S-I., and Seyed-Yagoobi, J., “Experimental study of electrohydrodynamic pumping through conduction phenomenon,” Journal of Electrostatics 56 (2):123-133, 2002.

[40] Jeong, S-I., and Seyed-Yagoobi, J., “Innovative electrode designs for electrohydrodynamic conduction pumping.” IEEE Transactions on Industry Applications 40 (3):900-904, 2004.

[41] Ashjaee, M., and Mahmoudi, S. “Experimental study of electrohydrodynamic pumping through conduction phenomenon using various fluids,” In: CEIDP'05. 2005 Annual Report Conference on Electrical Insulation and Dielectric Phenomenon, 2005., 2005. IEEE, pp 495-498

[42] Carey, V. P., “Liquid-Vapor Phase-Change Phenomenon, “Taylor & Francis Group, LLC, New York, NY, 2008.

[43] Nukiyama, S., “The maximum and minimum values of heat Q transmitted from metal to boiling water under atmospheric pressure,” J. Jap. Soc. Mech. Eng., vol. 37, pp. 367-374, 1934 (also, translated in Int. J. Heat and Mass Transf., Vol.9, pp. 1419-1433,1966).

[44] Kutateladze, S. S., “On the transition to film boiling under natural convection, Kotloturbostroenie,” no. 3, p. 10, 1948

[45] Zuber, N., “Hydrodynamic aspects of boiling heat transfer,” AEC Report AECU-4439, June 1959.

[46] Rohsenow, “A method of correlating heat transfer data for surface boiling of liquids”, ASME 74 (1952) 969–975,1952

[47] Yilmaz, S., Hwalek, J. J., and Westwater, J. W., “Pool boiling heat transfer performance for commercially enhanced tube surfaces,” ASME paper no. 80-HT-41, presented at the 19th National Heat Transfer Conference July, 1980

[48] Ribatski, G., and Saiz Jabardo, J. M., “Experimental study of nucleate boiling of halocarbon refrigerants on cylindrical surfaces”, Internatinal Journal of Heat and Mass Transfer 46 (2004) 4439-4451

[49] Saiz Jabardo, J. M., Fockink da Silva, E., Ribatshi, G., and de Barros, S. F., “Evaluation of the Rohsenow Correlation through Experimental Pool Boiling of Halocarbon Refrigerants on Cylindrical Surfaces”, ABCM, Vol.XXVI, April-June 2004.

[50] Saiz Jabardo, J. M., “An Overview of Surface Roughness Effects on Nucleate Boiling Heat Transfer,” The Open Transport Phenomenon Journal, 2010, 2, 24-34.

[51] Jones, B. J., Mchale, J. P., and Garimella, S. V., “The Influence of Surface Roughness on Nucleate Pool Boiling Heat Transfer,” Journal of Heat Transfer, 2009, Vol. 131/11009-1

[52] Hosseini, R., Gholaminejad, A., and Nabil, M., “Concerning the Effect of Surface Material on Nucleate Boiling Heat Transfer of R-113,” Journal of Electronics Cooling and Thermal Control, 2011, 1, 22-27

[53] Kim, Y. C., "Effect of surface roughness on pool boiling heat transfer in subcooled water-CuO nanofluid," Journal of Mechanical Science and Technology 28 (8) (2014) 3371-3376

[54] Nishikawa, Fujita, Uchida, Ohta, "Effect of surface configuration on nucleate boiling heat transfer," Internat. J. Heat Mass Transfer 27 (1983) 1559–1571.

[55] Moissis, R., and Berenson, P.J., "On the hydrodynamic transitions in nucleate boiling, ASME J. Heat Transfer," vol 85, pp. 221-229, 1963.

[56] Chang, You, "Heater orientation effects on pool boiling of microporous-enhanced surfaces in satured FC-72," J. Heat Transfer 118 (1996) 937–943.

[57] El-Genk, M. S., and Bostanci, "Saturation boiling of HFE-7100 from a copper surface, simulating a microelectronic chip," Internat. J. Heat Mass Transfer 46 (2002) 1841–1854.

[58] El-Genk, M. S., "Combined Effects of Subcooling and Surface Orientation on Pool Boiling of HFE-7100 from a Simulated Electronic Chip," Experimental Heat Transfer, 16:281-301, 2003

[59] Priarone, A., "Effect of surface orientation on nucleate boiling and critical heat flux of dielectric fluids," Internation Journal of Thermal Sciences 44 (2005) 822-831

[60] Howard, A.H. and Mudawar, I., "Orientation effects on pool boiling critical heat flux (CHF) and modeling of CHF for near-vertical surfaces," International Journal of Heat and Mass Transfer 42 (1999) 1665-1688.

[61] Vishnev, "Effect of orienting the hot surface with respect to gravitational field on the critical nucleate boiling of a liquid'" J. Engrg. Phys. 24 (1974) 43–48

[62] Lee, C. Y., Bhuiya, M. M. H., and Kim, K. J., "Pool boiling heat transfer with nano-porous surface," International Journal of Heat and Mass Transfer, 53, pp. 4274–4279, 2010.

[63] Forrest, E., Williamson, F., Buongiorno, J., Hu, L.W., Rubner, M., and Cohen, R., "Augmentation of nucleate boiling heat transfer and critical heat flux using nanoparticle thin-film coatings," International Journal of Heat and Mass Transfer, 53, pp. 58–67, 2010.

[64] Vemuri, S., and Kim, K. J., "Pool boiling of saturated FC-72 on nano-porous surface," International Communications in Heat and Mass Transfer, 32, pp. 27–31, 2005.

[65] Hendricks, T. J., Krishnan, S., Choi, C., Chang, C. H., and Paul, B., "Enhancement of pool-boiling heat transfer using nanostructured surfaces on aluminum and copper," International Journal of Heat and Mass Transfer, 53, pp. 3357–3365, 2010.

[66] Ahn, H., Sinha, N., Zhang, M., Banerjee, D., Fang, S., and Baughman, R., "Pool Boiling Experiments on Multiwalled Carbon Nanotube (MWCNT) Forests," Journal of Heat Transfer, 2006

[67] Ujereh, S., Fisher, T., and Mudawar, I., "Effects of carbon nanotube arrays on nucleate pool boiling," International Journal of Heat and Mass Transfer, 50, pp. 4023–4038, 2007.

[68] Chen, R., Lu, M., Srinivasan, V., Wang, Z., Cho, H., and Majumdar, H., "Nanowires for Enhanced Boiling Heat Transfer," NANO LETTERS, 9, pp. 2548-553, 2009.

[69] Wu, W., Bostanci, H., Chow, L. C., Hong, Y., Su, M., and Kizito, J. P., “Nucleate pool boiling heat transfer enhancement for water and FC-72 on titanium oxide and silicon oxide surfaces,” International Journal of Heat and Mass Transfer, 53, pp. 1773–1777, 2010.

[70] Launay, S., Fedorov A. G., Joshi, Y., Cao, A., Ajayan, P. M., 2006, "Hybrid micro-nano structured thermal interfaces for pool boiling heat transfer enhancement," Microelectronics Journal, 37, pp. 1158–1164.

[71] Im, Y., Joshi, Y., Dietz, C., and Lee, S. S., "Enhanced Boiling of a Dielectric Liquid on Copper Nanowire Surfaces," International Journal of Micro-Nano Scale Transport, 2010.

[72] Martinelli, R. C., and Nelson, D. B., "Prediction of pressure drop during force-circulation boiling of water," Trans. ASME, vol.70, pp. 695-702, 1948.

[73] Chisholm, D., and Laird, A. D. K., "Two-phase flow in rough tubes," Trans. ASME, vol. 80, pp. 276-286, 1958.

[74] Wallis, G. B., "One-Dimensional Two-Phase Flow," John Wiley, New York, NY, 1965.

[75] Chato, J., "Laminar condensation inside horizontal and inclined tubes ASHRAE Journal," pp. 52-60, 1962.

[76] Travis, D. P., Rohsenow, W. M., and Baron, A. B., "Forced convection condensation in tubes: A heat transfer correlation for condenser design," ASHRAE Transactions, vol. 79, Part 1, pp. 157-165, 1972.

[77] Shah, M. M., "A general correlation for heat transfer during film condensation inside pipes," Int. J. Heat and Mass Transfer, vol. 22, pp. 547-556, 1979.

[78] Bryan, J. E., and Seyed-Yagoobi, J., "Heat transport enhancement of monogroove heat pipe with electrohydrodynamic pumping," Journal of Thermophysics and Heat Transfer 11 (3):454-460, 1997.

[79] Jeong, S-I., and Didion, J., "Performance characteristics of electrohydrodynamic conduction pump in two-phase loops," Journal of Thermophysics and Heat Transfer 22 (1):90-97, 2008.

[80] Jeong, S-I., and Didion, J., “Thermal control utilizing an electrohydrodynamic conduction pump in a two-phase loop with high heat flux source," Journal of Heat Transfer 129 (11):1576-1583, 2007

[81] Pearson, M. R., and Seyed-Yagoobi, J., “Experimental Study of EHD Conduction Pumping at the Meso- and Micro-Scale,” IEEE J. Electrost., 69(6), pp. 479–485, 2011.

[82] Kano, I., and Nishina, T., “Electrode arrangement for micro-scale electrohydrodynamic pumping,” Journal of Fluid Science and Technology 5 (2):123-134, 2010.

[83] Mahmoudi, S. R., Adamiak, K., Castle, G. P., and Ashjaee, M., “Study of electrohydrodynamic micropumping through conduction phenomenon,” IEEE Transactions on Industry Applications 47 (5):2224-2234, 2011.

[84] Pearson, M. R., and Seyed-Yagoobi, J., “Electrohydrodynamic Conduction Driven Single- and Two-Phase Flow in Microchannels With Heat Transfer,” ASME J. Heat Transfer, 135 (10), p. 101701, 2013.

[85] Patel, V. K., Robinson, F., Seyed-Yagoobi, J., and Didion, J., “Terrestrial and Microgravity Experimental Study of Microscale Heat- Transport Device Driven by Electrohydrodynamic Conduction Pumping,” IEEE Trans. Ind. Appl., 49 (6), pp. 2397-2401, 2013.

[86] Patel, V. K., and Seyed-Yagoobi, J., “Long-Term Performance Evaluation of Microscale Two- Phase Heat Transport Device Driven by EHD Conduction,” ASME J. Heat Transfer, 50 (5), pp. 3011-3016, 2014.

[87] Patel, V. K., Robinson, F., Seyed-Yagoobi, J., and Didion, J., “Terrestrial and Microgravity Experimental Study of Microscale Heat- Transport Device Driven by

Electrohydrodynamic Conduction Pumping," IEEE Trans. Ind. Appl., 49 (6), pp. 2397-2401, 2013.

[88] Siddiqui, M. A. W., and Seyed-Yagoobi, J., "Experimental Study of Liquid Film Pumping Based on Conduction Phenomenon," IEEE Trans. Indus. Appl., in press, 2009.

[89] Nourdanesh, N., and Esmaeilzadeh, E., "Experimental study of heat transfer enhancement in electrohydrodynamic conduction pumping of liquid film using flush electrodes," Applied Thermal Engineering 50 (1):327-333, 2013.

[90] Yazdani, M., and Seyed-Yagoobi, J., "Electrically Induced Dielectric Liquid Fil Flow Based on Electric Conduction Phenomenon," IEEE Trans. Dielectr. Electr. Insul., 16(3), pp. 768–777, 2009.

[91] Yazdani, M., and Seyed-Yagoobi, J., "Numerical Investigation of Electrohydrodynamic-Conduction Pumping of Liquid Film in the Presence of Evaporation," ASME J. Heat Transfer, 131(1), p. 011602, 2008.

[92] Pearson, M. R., and Seyed-Yagoobi, J., "Experimental Study of Linear and Radial Two-Phase Heat Transport Devices Driven by Electrohydrodynamic Conduction Pumping," ASME J. Heat Transfer, 137(2), p. 022901, 2015.

[93] Patel, V. K., Seyed-Yagoobi, J., Sinha-Ray, S., Sinha-Ray, S., and Yarin, A., "Electrohydrodynamic Conduction Pumping Driven Liquid Film Flow Boiling on Bare and Nanofiber-Enhanced Surfaces," ASME J. Heat Transfer 138(4), p. 041501, 2016.

[94] Patel, V. K., Seyed-Yagoobi, J., Robinson, F., and Didion, J. R., "Effect of Gravity on Electrohydrodynamic Conduction Driven Liquid Film Flow Boiling," AIAA J. Thermophys. Heat Transfer, 30(2), pp. 429–437, 2016.

[95] Hanaoka, R., Takahashi, I., Takata, S., Fukami, T., and Kanamaru Y., “Properties of EHD pump with combination of rod-to-rod and meshy parallel plates electrode assemblies,” IEEE Transactions on Dielectrics and Electrical Insulation 16 (2):440-447, 2009

[96] Hanaoka, R., Takata, S., Murakumo, M., and Anzai, H., “Properties of liquid jet induced by electrohydrodynamic pumping in dielectric liquids,” Electrical Engineering in Japan 138 (4):1-9, 2002.

[97] Feng, Y., and Seyed-Yagoobi, J., “Understanding of electrohydrodynamic conduction pumping phenomenon,” Physics of Fluids (1994-present) 16 (7):2432-2441, 2004.

[98] Feng, Y., and Seyed-Yagoobi, J., “Control of adiabatic two-phase dielectric fluid flow distribution with EHD conduction pumping,” Journal of electrostatics 64 (7):621-627, 2006

[99] Sinnamon, S., "Coolant Distribution Control in Satellite Structural Panel using Electrohydrodynamic Conduction Pumping," Master thesis, 2009.

[100] Seyed-Yagoobi, J., “Electrohydrodynamic pumping of dielectric liquids,” J. Electrostatics, vol. 63, pp. 861-869, 2005.

[101] 3M, 2009, 3M™ Novec™ 7600 Engineered Fluid Product Information.

[102] DuPont, 2005, DuPont HCFC-123 Properties, Uses, Storage and Handling, DuPont Fluorochemicals, Wilmington, DE.

[103] DuPont, 2005, Thermodynamic Properties of HCFC-123 Refrigerant, DuPont Fluorochemicals, Wilmington, DE.

[104] Bryan, J. E., "Fundamental Study of Electrohydrodynamically Enhanced Convective and Nucleate Boiling Heat Transfer," Ph.D. Thesis, Texas A&M University, College Station, TX, 1998.

[105] Castellanos, A., "Conduction models in dielectric liquids," in Electrohydrodynamics. Vienna, Austria: Springer, pp. 103–120, 1998.

[106] Kennedy, J. E., Roach Jr, G. M., Dowling, M. F., Abdel-Khalik, S. I., Ghiaasiaan, S. M., Jeter, S. M., and Quereshi, Z. H., "The onset of flow instability in uniformly heated horizontal microchannels", ASME J. Heat Transfer 122 118–125, 2012.

[107] Shu, H. S., and Lai, F. C., "Effect of electrical field on buoyancy-induced flows in an enclosure," IEEE IAS Annu. Meeting, pp. 1465–1472, 1995.

[108] Yang, H., and Lai, F. C., "Effects of Joule Heating on EHD-enhanced Natural Convection in an Enclosure" IEEE IAS Annu. Meeting, pp. 1851–1858, 1997.

[109] Jeong, S. I., Seyed-Yagoobi, J.,and Atten, P., "Fluid circulation in an enclosure generated by electrohydrodynamic conduction phenomenon," IEEE Trans. Ind. Appl., vol. 11, no. 5, pp. 899–910, Oct. 2004.

[110] Yazdani, M., and Seyed-Yagoobi, J., "Fluid Circulation within a Spherical Reservoir with EHD Conduction Pumping," IEEE Trans. Ind. Appl. 45.

[111] Yazdani, M., and Seyed-Yagoobi, J., "Thermal Homogenization in Spherical Reservoir by Electrohydrodynamic Conduction Phenomenon," Journal of Heat Transfer. SEPTEMBER Vol. 131/ 094502-1, 2009.

[112] Bryan, J. E., and Seyed-Yagoobi, J., "Development of a Unique Facility to Measure Electrical Properties of Dielectric Liquid Over a Large Range of Temperature and

Pressure," ICDL 12th International Conference on Conduction and Breakdown in Dielectric Liquids, pp. 488-491, 1996.

[113] Noureddini, H., Teoh, B.C., and Clements, L. D., "Densities of Vegetable Oils and Fatty Acids," JAOCS, Vol. 69, no. 12, December. 1992.

[114] Fasina, O. O., and Colley, Z., "Viscosity and Specific Heat of Vegetable Oils as a Function of Temperature: 35°C to 180 °C," International Journal of Food Properties, 11: 738-746, 2008.

[115] Turgut, A., Tavman, I., and Tavman, S., "Measurement of Thermal Conductivity of Edible Oils using Transient Hot Wire Method," International Journal of Food Properties, 12: 741-747, 2009.

[116] Reneker, D. H., Yarin, A. L., Fong, H., and Koombhongse, S., J. Appl. Phys, 87, pp. 4531, 2000.

[117] Yarin, A. L., Koombhongse, S., and Reneker, D. H., 2011, J. Appl. Phys, 89, pp.3018.

[118] Theron, A., Zussman, E., and Yarin, A. L., 2011, Nanotechnolgy, 12, pp.384-390.

[119] S Sinha-Ray, Y Zhang and A L Yarin., 2011, Langmuir, 27, pp. 215-226.

[120] Hsu, Y. Y., "On the size range of active nucleation cavities on a heating surface," J. Heat Transfer, vol.84, pp. 207-213, 1962.

[121] Shell and tube heat exchanger <https://en.wikipedia.org/wiki/Shell_and_tube_heat_exchanger>

[122] NASA. (2016). Zero Boil-Off Tank (ZBOT). https://www.nasa.gov/mission_pages/station/research/experiments/1270.html#results

[123] 3M Immersion cooling for data centers < http://www.3m.com/3M/en_US/novec-us/applications/immersion-cooling/>

[124] https://www.overclockers.ru/hardnews/84737/na-computex-gigabyte-pokazala-polnostju-pogruzhennyj-v-zhidkost-server.html

[125] S. J. Kline, and F. McClintock, “Describing Uncertainties in Single-sample Experiments,” Mechanical Engineering, vol. 75, no. 1, pp. 3-8, 1953.

[126] R. J. Moffat, “Describing the Uncertainties in Experimental Results,” Experimental Thermal and Fluid Science, vol. 1, no. 1, pp. 3-17, 1988.

[127] National Institute of Standards and Technology. ITS-90 Thermocouple Database. July 2000. Web. 06 October2010. <http://srdata.nist.gov/its90/main/its90_main_page.html>.